

**LUMINESCENCE INVESTIGATION OF ZINC OXIDE NANOPARTICLES
DOPED WITH RARE EARTH IONS**

by

GUY LEBA KABONGO

submitted in accordance with the requirements
for the degree of

MASTER OF SCIENCE

In the subject

PHYSICS

at the

UNIVERSITY OF SOUTH AFRICA

SUPERVISOR : PROF. M S DHLAMINI

CO-SUPERVISOR : DR. B M MOTHUDI

NOVEMBER 2013

Declaration

(Student number: 5050-131-3)

I declare that “LUMINESCENCE INVESTIGATION OF ZINC OXIDE NANOPARTICLES DOPED WITH RARE EARTH IONS” is my own work and that all sources that I have used or quoted have been indicated and acknowledged by means of complete references.

SIGNATURE
(G. LEBA KABONGO)

____22nd November 2013____

DATE

Thesis dedicated to the memory of the late
Dr. Kabongo Raphael (1930-2013) and
Papa Kabongo Ndundu Willem (1944-2013)

“Science without conscience is but the ruin of the soul”

François Rabelais (1494-1553)

“Meeji a kalasa kaena mwa kupita meyi ne mikandu ya ba nkambwa nansha!”

Acknowledgements

- First and foremost, I would like to thank God, for giving me courage and strength during these years.
- I am deeply grateful to both my promoters, *Prof. M.S. Dhlamini*, *Prof. B.M. Mothudi* and *Dr. G.H. Mhlongo* for their research guidance, encouragements, and support which made this work meaningful and a success.
- I would also like to express my sincere appreciation to *Prof. K.T. Hillie* for his professional support and suggestions. *Prof. H.C. Swart* is also acknowledged for his support, suggestions and encouragements. *Dr. R.E. Kroon* and *Dr. D.E. Motaung* are acknowledged for He-Cd Laser and Raman spectroscopy measurements, respectively.
- Many thanks to the NCNSM - Centre staff at *CSIR* for their inspiration and continued support. I am grateful to *Dr. B.W. Mwakikunga* for his encouragements and *Dr. James*. The support of *Thomas, Ntombi, Tutuzwa, Charity, Sharon, Edwin* is highly appreciated.
- I especially thank my fellow researchers and staff of the department of Physics for their assistance and support they gave me at *UNISA*, especially *Collen*.
- My special thanks to *Dr. Diulu Kabongo* for his huge support during this long journey. I would also like to thank *Dr. Willy Kabongo* for his encouragements, and also to *Dr. Prudence Kayoka Kabongo* for her advices, *Dr. Leba Kabongo*, *Dr. Evelyne Kabongo*, *Myriam*, *Eric*, *Ange*, *Gracia*, *Guylain*, *Winny*, *Delphin*, for their understanding, encouragement and support during these years.
- Great thanks to both *National Research Foundation (NRF)* and the *Council for Scientific and Industrial Research (CSIR)* of South Africa as well as *UNISA* for funding this project. The support of the *Ministère de l'Enseignement Supérieur et Universitaire (R.D. Congo)* is also appreciated.
- Many thanks to *Benith (helpmate)* for her understanding.
- Last but not the least, my truthful indebtedness to my parents for their fundamental moral support.

Summary

Un-doped, Tb^{3+} as well as Yb^{3+} doped ZnO nanocrystals with different concentrations of RE^{3+} (Tb^{3+} , Yb^{3+}) ions were successfully synthesized via sol-gel method to produce rare earth activated zinc oxide nanophosphors. The phosphor powders were produced by drying the precursor gels at 200°C in ambient air.

Based on the X-ray diffraction results, it was found that the pure and RE^{3+} doped ZnO nanophosphors were highly polycrystalline in nature regardless of the incorporation of Tb^{3+} or Yb^{3+} ions. Moreover, the diffraction patterns were all indexed to the ZnO Hexagonal wurtzite structure and belong to $P6_3mc$ symmetry group. The Raman spectroscopy confirmed the wurtzitic structure of the prepared samples.

Elemental mapping conducted on the as prepared samples using Scanning electron microscope (SEM) equipped with energy dispersive X-ray spectrometer (EDX) revealed homogeneous distribution of Zn, O, and RE^{3+} ions. The high resolution transmission electron microscope (HR-TEM) analyses indicated that the un-doped and RE^{3+} doped samples were composed of hexagonal homogeneously dispersed particles of high crystallinity with an average size ranging from 4 to 7 nm in diameter, which was in agreement with X-ray diffraction (XRD) analyses.

ZnO: Tb^{3+} PL study showed that among different Tb^{3+} concentrations, 0.5 mol% Tb^{3+} doped ZnO nanoparticles showed clear emission from the dopant originating from the $4f-4f$ intra-ionic transitions of Tb^{3+} while the broad defects emission was dominating in the 0.15 and 1 mol% Tb^{3+} doped ZnO. Optical band-gap was extrapolated from the Ultraviolet Visible spectroscopy (UV-

Vis) absorption spectra using TAUC's method and the widening of the optical band-gap for the doped samples as compared to the un-doped sample was observed. The PL study of ZnO:Yb³⁺ samples was studied using a 325 nm He-Cd laser line. It was observed that the ZnO exciton peak was enhanced as Yb³⁺ ions were incorporated in ZnO matrix. Furthermore, UV-VIS absorption spectroscopic study revealed the widening of the band-gap in Tb³⁺ doped ZnO and a narrowing in the case of Yb³⁺ doped ZnO system.

X-ray photoelectron spectroscopy demonstrated that the dopant was present in the doped samples and the result was found to be consistent with PL data from which an energy transfer was evidenced. Energy transfer mechanism was evidenced between RE³⁺ and ZnO nanocrystals and was discussed in detail.

Key terms

Sol-gel, ZnO nanoparticles, photoluminescence, energy transfer, rare earth, terbium, ytterbium

Acronyms

EDX	- Energy dispersive X-ray spectroscopy
EtOH	- Ethanol
FE-SEM	- Field emission scanning electron microscope
HR-TEM	- High resolution transmission electron microscope
PL	- Photoluminescence
QD	- Quantum Dot
TGA	- Thermogravimetric analysis
UV-Vis	- Ultraviolet visible spectroscopy
XPS	- X-ray photoelectron spectroscopy
XRD	- X-ray diffraction

Table of contents

Declaration.....	i
Dedication	ii
Epigraph.....	iii
Acknowledgements.....	iv
Summary.....	v
Key terms.....	vi
Acronyms.....	vi
Table of content.....	vii

Chapter 1. Introduction

1.1. Background.....	1
1.2. Problem statement.....	5
1.3. Study objectives.....	6
1.4. Thesis layout.....	7
1.5. References.....	8

Chapter 2. Basic Literature

2.1. Introduction.....	11
2.2. Photoluminescence.....	11
2.2.1. Intrinsic luminescence.....	13
2.2.2. Extrinsic luminescence.....	13
2.3. Trivalent rare earth ions.....	14
2.4. Zinc oxide host material.....	19
2.4.1. Background.....	19
2.4.2. Crystals structure.....	20
2.4.3. Defects in ZnO.....	23
2.4.4. ZnO Quantum dots.....	25
2.4.4.1 Effective mass approximation for quantum dots.....	26
2.4.4.2 Surface effect.....	27
2.5. Energy transfer in phosphors.....	28
2.5.1. Background.....	28
2.5.2. Mechanism of energy transfer.....	30
2.6. Photoluminescence related properties.....	33
2.6.1. Concentration quenching.....	33
2.6.2. Killer centers.....	34
2.6.3. Absorption coefficient.....	35
2.6.4. Quantum yield.....	36
2.6.5. Franck-Condon principle.....	37
2.7. Applications.....	38
2.8. References.....	40

Chapter 3. Synthesis and Research Techniques

3.1. Introduction.....	46
3.2. Sol-gel process.....	46
3.3. Preparation of ZnO and ZnO:RE ³⁺ (RE=Tb,Yb) nanophosphor.....	52
3.4. Characterization techniques.....	55
3.4.1. Optical characterization.....	55
3.4.2. Structural characterization.....	59
3.4.3. Surface characterization.....	61
3.5. References.....	70

Chapter 4. Properties of Terbium ions in ZnO Nanocrystals

4.1. Introduction.....	74
4.2. Experimental.....	75
4.2.1. Un-doped and Tb ³⁺ -doped ZnO nanocrystals preparation.....	75
4.2.2. Characterization.....	76
4.3. Results and discussion.....	77
4.3.1. Surface morphology.....	77
4.3.2. Structural properties.....	80
4.3.3. Optical properties.....	85
4.4. Conclusion.....	92
4.5. References.....	93

Chapter 5. Properties of Ytterbium ions in ZnO Nanocrystals

5.1. Introduction.....	97
5.2. Experimental detail.....	98
5.3. Results and discussion.....	98
5.3.1. Structural and surface properties.....	98
5.3.2. Optical properties.....	105
5.4. Conclusion.....	109
5.5. References.....	110

Chapter 6. Conclusion and Future Works

6.1. Conclusion.....	112
6.2. Future works.....	113
Appendix.....	114
A.0. Thermogravimetric analysis results.....	114
A.1. Publications.....	115
A.2. Conferences.....	116
A.3. Awards.....	116
Résumé.....	119

Chapter 1. Introduction

1.1 Background

As a drive to design, synthesize and fabricate efficient luminescent materials worldwide, scientists have found tremendous interests in this research field. They have been attracted particularly to control shape and size, investigate the physical, optical and luminescent properties of a new generation of light emitting materials known as “*phosphors*” at nanoscale [1,2]. Phosphors can absorb energy from the incident radiation and emit photons after successions of energy transfer processes. To satisfy the demands for a number of applications, phosphors are generally in the powder form with detailed requirements on particle size and morphology [3]. Rare earth based phosphors have found extensive applications in a variety of fields in recent years such as cathode-ray tube (CRT) screens and liquid-crystal display (LCD) which are the most commercialized display devices. Besides, solar cells appears to be a novel world class field for application of rare earth based phosphors, in this regard a very recent world record breaking solar cell with 44.7% efficiency have been announced jointly by the Fraunhofer Institute for Solar Energy Systems ISE and the Helmholtz Center Berlin. However, in a theoretical study, Trupke [4] and colleagues have predicted a maximum efficiency of approximately 63% for concentrated sunlight and 48% for nonconcentrated sunlight.

In 1959, Richard Feynmann in one of his famous Caltech talk entitled “There’s Plenty of Room at the Bottom”, stated that: *“I would like to describe a field, in which little have been done, but in which enormous amount can be done in principle. The field is not quite the same as others in that it will not tell us much of fundamental physics (in the sense of, “What are the strange particles?”), but it is more like solid-state physics in the sense that it might tell us much of great interest about the strange phenomena that occur in complex situations. Furthermore, a point that is most important is that it would have an enormous number of technical applications. What I want to talk about is the problem of manipulating and controlling things on a small scale. . . . What I have demonstrated is that there is room—that you can decrease the size of things in a practical way. I now want to show that there is plenty of room. I will not now discuss how we are going to do it, but only what is possible in principle...We are not doing it simply because we haven’t yet gotten around to it”*. This brilliant lecture gave a tone to a dynamic interest of the nanoscopic world and revolutionized the scientific community view of nanosciences [5-7].

There is a bridge to be crossed between nanosciences and nanotechnology. Nanotechnology is known to be the understanding and control of matter at dimensions between approximately 1 and 100 nanometers, where unique phenomena enable novel applications of nanoparticles [2,8]. On the other hand, Nanoscience is defined as the science underlying nanotechnology [2].

Among other nanostructures such as nanorods, polymers, carbon nanotubes (Graphene), quantum wire, quantum well, etc, this study, focuses on a particular class of nanostructure called “quantum dots”, which are also known in the field as “artificial atoms” and consist of approximately 100 to 10 000 atoms [9,10]. Quantum dot are known to exhibit discrete energy levels due to the quantum confinement effect which result in an increase of the energy gap of a semiconductor

nanocrystals with decreasing their size. Detailed discussion on quantum dots will follow in the next chapter. We are interested mainly in investigating their luminescence properties.

Luminescence, defined as the electromagnetic radiation from phosphors with suitable excitation, was first named in 1888 by the German physicist Eilhard Wiedemann. He characterized light emission originating from processes other than the increase of temperature [11]. Further discussion on luminescence mechanism and categories is presented in the next chapter. The so-called ‘cold light’ is in clear difference to incandescence, which is light released by a substance as a consequence of heating. Luminescence can be classified depending on the excitation source, see **Table 1.1**. In the current study the focus will be on the first form of luminescence on the table, photoluminescence, since it is the most common used in solar cells [12].

Table 1.1 The different types of luminescence.

Name	Excitation source
Photoluminescence	Light
Cathodoluminescence	Electrons
Radioluminescence	X-rays, α -, β -, or γ -rays
Thermoluminescence	Heating
Electroluminescence	Electric field or current
Triboluminescence	Mechanical energy
Sonoluminescence	Sound waves in liquids
Chemiluminescence and bioluminescence	Chemical reactions

While theories of solids were still in an infant stage of development, the field of luminescence used to be treated “*more as an art than science*”. Furthermore, during the early days of studies of luminescence, the main efforts were intended at making valuable and efficient luminescent materials. The forerunners, Lenard and his school have undertaken methodical and comprehensive investigations in the foundation properties of materials like alkaline earth sulphide phosphors [13]. Studies in luminescence in that period were motivated by application possibilities: even then, such studies by the way generated results of fundamental importance, and facilitated our predecessors in subsequent interpretative work in some simple cases at least. Additionally, the work of Hilsch, Pohl and their collaborators during the period of 1925 to 1932 on the optical and electronic properties of alkali halide crystals and colour centres can be looked as an important breakthrough in the contemporary progress for understanding the properties of luminescent crystals [13].

The foremost materials of interest in the current study are rare earth (RE) based phosphors. Rare earth ions are ideal candidates for spectral conversion, due to their high luminescence efficiencies and rich energy level structure that allows for great flexibility in the upconversion and downconversion of photons in a wide spectral region (NIR-VIS-UV) [14]. Moreover, Zinc oxide as a wide direct bandgap (3.37 eV) semiconductor with a large exciton binding energy at room temperature (60 meV) is known to be one of the ideal host candidates for rare earth ions [15]. Researchers faced some challenges such as the low solubility of the dopant in the matrix resulting in a material exhibiting two phases due to the low temperature processing, in addition other important factors are reported by Gali et al. and Erwin et al. [16,17].

It should be pointed out that, the fascination for lanthanide (Ln) optical study dates back to the 1880s when renowned scientists such as Sir William Crookes, LeCoq de Boisbaudran, Eugène

Demarçay or, later, Georges Urbain were using luminescence as an analytical tool to test the purity of their crystallizations and to identify potential new elements [18].

Among all lanthanides (Ln) which are luminescent except La^{3+} and Lu^{3+} , this dissertation focuses on Terbium (Tb^{3+}) for which the *f-f* emission lines cover the entire spectrum in the visible region. Furthermore, we have also found interests on Ytterbium (Yb^{3+}) which is luminescent in the near-infrared (NIR) region of the electromagnetic spectrum [18]. We have to note that depending on the excitation wavelength some of these ions are fluorescent, others phosphorescent and some are both [18].

To the best of our knowledge, only few groups of researchers have reported their successful synthesis of luminescence materials based on ZnO nanocrystals doped with lanthanides, in particular Terbium and Ytterbium [19-22].

1.2 Problem Statement

The development of a novel generation of high resolution and high efficiency luminescent devices has initiated a necessity for phosphors with tuneable optical properties. Previously, it has been reported that high definition display devices require submicron particle sizes to optimize screen resolution and luminescence efficiency [23]. Semiconductor nanocrystals can be synthesized with sizes ranging from 2 to 10 nm and thus achieve the size requirement for quantum confinement process. This new generation of light emitting materials, nano-sized phosphors, has shown fascinating properties such as high quantum efficiency for photoluminescence, ultra-fast recombination time and increased energy band-gap for luminescence due to the low dimension of the particles [24-27]. A prodigious deal of work started during the past decade has set a special importance on the nanocomposites consisting of

semiconductor nanocrystals. ZnO nanoparticles are often embedded in dielectric matrices such as glasses and polymers and are of great importance as phosphor materials for solar cells device fabrication. However, doping of the ZnO semiconductor nanocrystals below 10 nm still remains a challenge among the scientific community. This study is focusing on developing RE^{3+} ($\text{Tb}^{3+}, \text{Yb}^{3+}$) doped ZnO nanoparticles in the particle size range below 10 nm in order to improve the performance of the solar cells buffer layer.

Due to its wide direct band gap (3.37 eV), large exciton binding energy (60 meV) and high optical gain (320 cm^{-1}), ZnO seems to be a promising contender, and the development of this phosphor could make a massive impact technologically worldwide. Photoluminescence (PL) studies will be carried out on the luminescent properties of the semiconductor nanocrystals powder phosphors. The absorption and emission properties of these phosphors are of primary importance.

This study propose a procedure for doping ZnO semiconductor nanocrystals (<10 nm) using sol-gel method. Sol-gel is used for its low energy consumption, good control of particle size, uniform morphology of the particles in the final product as well as its very low cost.

1.3 Study Objectives

- To synthesise pure and rare earth doped ZnO nanocrystals, using the sol-gel method.
- To study the structural and photoluminescence properties of the undoped and rare earth doped ZnO
- To investigate energy transfer from ZnO nanophosphors to RE^{3+} , etc.

1.4 Thesis Layout

- **Chapter 2** deals with the literature review.
- **Chapter 3** provides a summary of the theory of the research techniques used in this study. This includes a brief description on how each of these techniques works as well as the theory of the method of synthesis of ZnO and RE³⁺ doped ZnO nanophosphors.

In the next chapters research carried out in the National Centre for Nano-Structured Materials (NCNSM) of the Council for Scientific and Industrial Research (CSIR) is reported and discussed:

- **Chapter 4** discusses the study of ZnO:Tb³⁺ nanocrystals. The morphology, structural properties and elemental composition of the as-prepared samples are presented and discussed. Furthermore, the luminescent properties and mechanism of energy transfer are discussed in details.
- **Chapter 5** presents results on the investigation of ZnO:Yb³⁺ nanophosphors. The structural and optical properties presented are discussed as well as the surface chemical composition results.
- **Chapter 6** is about summary of the results, conclusion and suggestions for possible future studies.

1.5 References

- [1] Ozawa L, *Cathodoluminescence and Photoluminescence: theories and practical applications*, CRC Press, Boca Raton, FL, (2007)
- [2] Ramsden J, *Essentials of nanotechnology*, Jeremy Ramsden & Ventus Publishing, (2009). ISBN 978-87-7681-418-2
- [3] Blasse G, *Chem of Mat* **1**(3) (1989) 294
- [4] Trupke T, Green MA and Würfel P, *J Appl Phys* **92** (2002) 4117
- [5] Feynman R, *There's plenty of room at the bottom*, In: *Miniaturization*, ed. H.D. Gilbert, p.282-296. New York: Reinhold (1961)
- [6] www.sciencemag.org, *Science* **254**, [Accessed, 4 July 2012]
- [7] Michael Roukes in *Physics World* **14**(2) February (2001),
<http://nano.caltech.edu/publications/papers/SciAm-Sep01.pdf>, [Accessed, 2 April 2013]
- [8] What is nanotechnology?
<http://mrsec.wisc.edu/Edetc/nanotech/index.html>, [Accessed, 21 May 2012]
- [9] Bukowski TJ and Simmons JH, *Quantum dot research: Current state and future prospects. Critical Reviews in Solid State and Materials Sciences* **27**(3-4) (2002) 119
- [10] Efros AL and Rosen M, *The electronic structure of semiconductor nanocrystals. Annual Review of Materials Science* **30** (2000) 475
- [11] Valeur B and Berberan-Santos MrN, *J Chem Ed* **88**(6) (2011) 731
- [12] Nir Yaacobi-Gross, *Colloidal Semiconductor Nanocrystals Based Solar Cells*, 2012, [PhD Thesis], Israel Institute of Technology, Israel
- [13] Bose HN, *Indian Journal of history of Science* **27**(4) (1992)
- [14] Andries Meijerink, *Lanthanide Ions as Photon Managers for Solar Cells* [online, 04 February 2013]
- [15] Jin Xu, *Luminescence in ZnO*, 2004, [MSc Thesis], Virginia Comm. University, USA
- [16] Galli G, *Nat Phys* **436** (2005) 32
- [17] Erwin SC, Zu L, Haftel MI, Efros AL, Kennedy TA and Norris DJ, *Nat Phys* **436** (2005) 91
- [18] Jean-Claude G Bunzli and Svetlana V Eliseeva, *Basics of Lanthanide Photophysics in Lanthanide Luminescence: Photophysical, Analytical and Biological Aspects*, Springer (2010)

- [19] Partha P Pal and Manam J, *Mater Sci Eng B* **178** (2013) 400
- [20] Bayan S, Das U and Mohanta D, *Phys Status Solidi A* **207** (2010) 1859
- [21] Soumahoro I, Schmerber G, Douayar A, Colis S, Abd-Lefdil M, Hassanain N, Berrada A, Muller D, Slaoui A, Rinnert H and Dinia A, *J Appl Phys* **109** (2011) 033708
- [22] Shestakov MV, Baranov AN, Tikhomirov VK, Zubavichus YV, Kuznetsov AS, Veligzhanin AA, Kharin AY, Rosslhuber R, Timoshenko VYV and Moshchalkov VV, *RSC Adv* **2** (2012) 8783
- [23] Yang H, Holloway PH, *J Chem Phys* **121** (2004) 7421
- [24] Yang P, Song CF, Meng Kai Lu, Xin Yin, Guang Jun Zhou, Dong Xu, Duo Rong Yuan, *Chem Phys Lett*, **345** (2001) 429
- [25] Myung-Han Lee, Seong-Geun Oh and Sung-Chul Yi, *J Colloid and Interface Sci* **226** (2000) 65
- [26] Bhargava RN, *J Lumin* **70** (1996) 85
- [27] Dhlamini MS, *Luminescent properties of Synthesized PbS nanoparticles phosphors*, 2008, [PhD Thesis], University of the Free State, South Africa

Chapter 2. Basic Literature

This chapter presents a combined portrait and elucidations of the luminescence and allied phenomena as well as the various areas of application of light emitting materials (phosphors). The emphasis is on rare earth (RE) ions which are seen as the most accurate luminescent centers due to their high colour purity emission lines. Moreover, emphasis on Zinc oxide (ZnO), a wide direct band-gap (3.37 eV) semiconductor with a large exciton binding energy (60 meV) and high optical gain (320 cm^{-1}) at room temperature, which is used as the host material is provided and discussed. Furthermore, energy transfer and other properties related to nanophosphors based rare earth are discussed. All in all, focus will be on a particular class of nanoparticles called “quantum dots”. References are provided in the chapter wherever necessary.

2.1 Introduction

A phosphor, most commonly, is a material that exhibits the phenomenon of luminescence. Rather confusingly, this includes both phosphorescent materials, which show a slow decay in brightness ($>1\text{ms}$), and fluorescent materials, where the emission decay takes place over tens of nanoseconds [1].

Phosphors are often transition metal compounds or rare earth compounds of various categories. The well-known application of phosphors is in Cathode Ray Tube (CRT) displays and fluorescent lights. CRT phosphors were standardized beginning around World War II and designated by the letter "P" followed by a number [1]. There are different forms of luminescence depending on the method of excitation, which include photoluminescence, cathodoluminescence, chemiluminescence, electroluminescence, bioluminescence etc. The focus in this study is on photoluminescence and this form of luminescence is discussed in the next section.

2.2 Photoluminescence

Photoluminescence (PL), namely, the result of spontaneous emission in a photo-excited system, can be schematized in terms of a three-step process, as shown in **figure 2.1** [2]:

- (a) Absorption of a photon of energy $\hbar\omega$ resulting in a creation of an electron–hole pair.
- (b) Relaxation of the free electron and hole, respectively, near the bottom of the conduction band (CB) and the top of the valence band (VB) (in defect-free samples) by fast scattering with acoustic and optical phonons.

(c) Radiative recombination of the electron and hole, during or at the end of the relaxation process, with a return of the system to its ground state by emission of a photon of energy lower than $\hbar\omega$.

The recombination processes more frequently observed in a PL spectrum are related to the excited states of lowest energy, as shown in **figure 2.2**. This is due to the fact that the timescale of the relaxation processes ($\sim 10^{-12}$ s) is much faster than that of the radiative recombinations ($\sim 10^{-9}$ s), so that photon emission takes place only after carriers have reached the excited states of minimum energy [2].

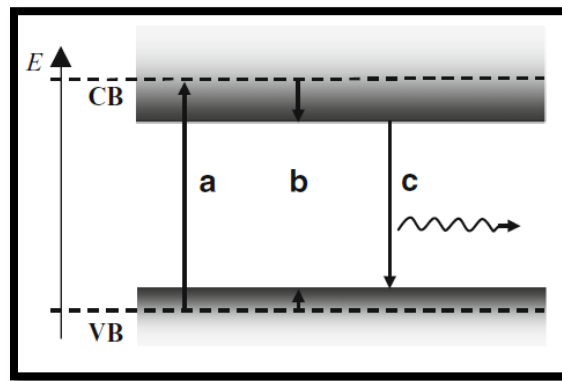


Figure 2.1: Schematic illustration of the three-step photoluminescence process: (a) absorption; (b) relaxation; (c) radiative recombination and photon emission. Shaded areas indicate valence and conduction bands [2].

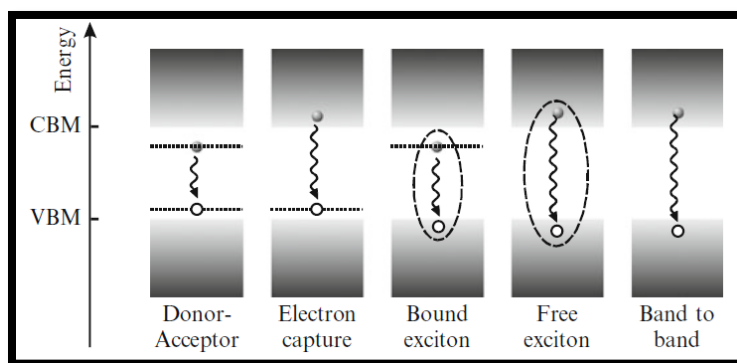


Figure 2.2: Leading recombination processes observed in photoluminescence. The shaded areas indicate VB and CB, while the horizontal dotted lines denote the energy positions of defect states. Electrons (holes) are indicated by dark-shaded (hollow) dots. Undulated arrows indicate radiative recombination. Dashed curves highlight the Coulomb interaction [2].

The PL process is generally classified in terms of the nature of the electronic transitions generating it. Generally PL is categorized into two distinct classes, namely, intrinsic and extrinsic luminescence.

2.2.1 Intrinsic luminescence

There exist three different types of intrinsic luminescence. The first in which the electrons in the conduction band recombine with holes in the valence band leading to emission of light is called band to band luminescence; this process is always observed at high temperatures in crystals of high purity. On the other hand, there is a luminescence process in which an excited electron and a hole interacting with one another moves within the crystal, consequently transferring energy resulting in an emission due to the recombination of electrons and holes, this process is the exciton luminescence and it occurs at relatively low temperature. The last but not the least is the cross-luminescence which consist of the recombination of an electron and a hole in the outer most core band, it occurs when the energy difference between the top valence band and that of the outer most core band is smaller than the band gap energy [3,4].

2.2.2 Extrinsic luminescence

Extrinsic luminescence is the phenomenon in which photons are generated by intentionally incorporated foreign atoms or defects in the host matrix. These foreign atoms are well-known as ‘‘activators’’ in phosphor materials structures. This phenomenon is classified into different type namely localized and unlocalized nature of emission. The localized luminescence refers to excitation and emission processes which are confined to localized centers and its counterpart depends on an eventual contribution of excited electrons and holes in the process of luminescence [3].

2.3 Trivalent Rare Earth (RE³⁺)

The rare earth elements (REEs), which include the 15 lanthanide elements ($Z = 57$ through 71) and yttrium ($Z = 39$), are so called because most of them were formerly isolated in the 18th and 19th centuries as oxides from rare minerals [5].

The discovery of rare earths started in 1787 when Swedish Army Lieutenant Karl Axel Arrhenius collected the black mineral ytterbite (later renamed gadolinite) from a feldspar and quartz mine near the village of Ytterby, Sweden (Weeks and Leicester, 1968, p. 667). Although rare-earth bearing minerals were collected earlier, none were identified as containing a new "rare" and different "earth" (a historical term for an oxide) until B.R. Geijer of the Royal Mint of Sweden, forwarded the Arrhenius sample to Finland for analysis [6].

An exciting feature of luminescent lanthanide compounds is their line-like emission, which results in high color purity of the emitted light (see **figure 2.3**). The emission color depends on the lanthanide ion but is largely independent of the environment of a given lanthanide ion [7].

It has been evidenced that in almost all the cases the emission from the rare earth ions is due to optical transitions within the 4fⁿ configuration (e.g. Tb³⁺ (4f⁸), and Eu³⁺ (4f⁶)) see **table 2.1**. The 4f orbital lies inside the ion and therefore it is well shielded from the surroundings by the filled 5s² and 5p⁶ orbitals so that the 4f electrons are less influenced by the environment of the lanthanide ion [8-10]. The shapes of the seven 4f orbitals are presented on top of **figure 2.4** [11].

It is also well known that the *f-f* emission lines are sharp, this, is because the rearrangement consecutive to the promotion of an electron into a 4f orbital of higher energy does not perturb the binding pattern in the molecules since 4f orbitals do not participate much in this binding (the

covalency of a Ln^{III} ligand bond is at most 5–7%) [11]. Therefore, the internuclear distances remain almost the same in the excited state, which generates narrow bands and very small Stokes' shifts (**figure 2.5**) [11]. The Dieke diagram gives more details about the $4f^n$ energy levels of lanthanides ions (see **figure 2.6**).

Table 2.1: Electronic Structure of the Trivalent rare earth Ions [7].

Element	Symbol	Atomic number (Z)	Configuration Ln^{3+}	Ground state Ln^{3+}
lanthanum	La	57	[Xe]	$^1\text{S}_0$
cerium	Ce	58	[Xe]4f ¹	$^2\text{F}_{5/2}$
praseodymium	Pr	59	[Xe]4f ²	$^3\text{H}_4$
neodymium	Nd	60	[Xe]4f ³	$^4\text{I}_{9/2}$
promethium	Pm	61	[Xe]4f ⁴	$^5\text{I}_4$
samarium	Sm	62	[Xe]4f ⁵	$^6\text{H}_{5/2}$
europium	Eu	63	[Xe]4f ⁶	$^7\text{F}_0$
gadolinium	Gd	64	[Xe]4f ⁷	$^8\text{S}_{7/2}$
Terbium	Tb	65	[Xe]4f⁸	$^7\text{F}_6$
Dysprosium	Dy	66	[Xe]4f ⁹	$^6\text{H}_{15/2}$
Holmium	Ho	67	[Xe]4f ¹⁰	$^5\text{I}_8$
Erbium	Er	68	[Xe]4f ¹¹	$^4\text{I}_{15/2}$
Thulium	Tm	69	[Xe]4f ¹²	$^3\text{H}_6$
Ytterbium	Yb	70	[Xe]4f¹³	$^2\text{F}_{7/2}$
Lutetium	Lu	71	[Xe]4f ¹⁴	$^1\text{S}_0$

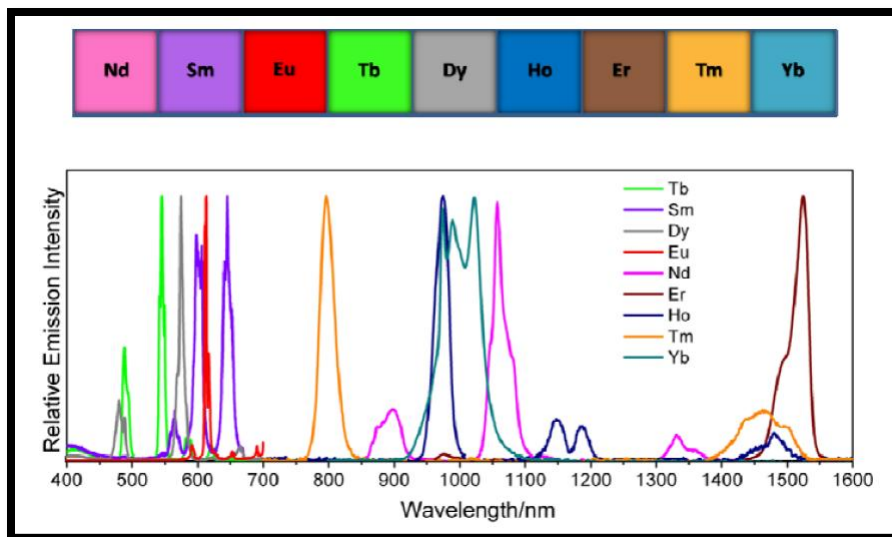


Figure 2.3: Luminescent lanthanide cations and their characteristic emission bands [12,13,14]

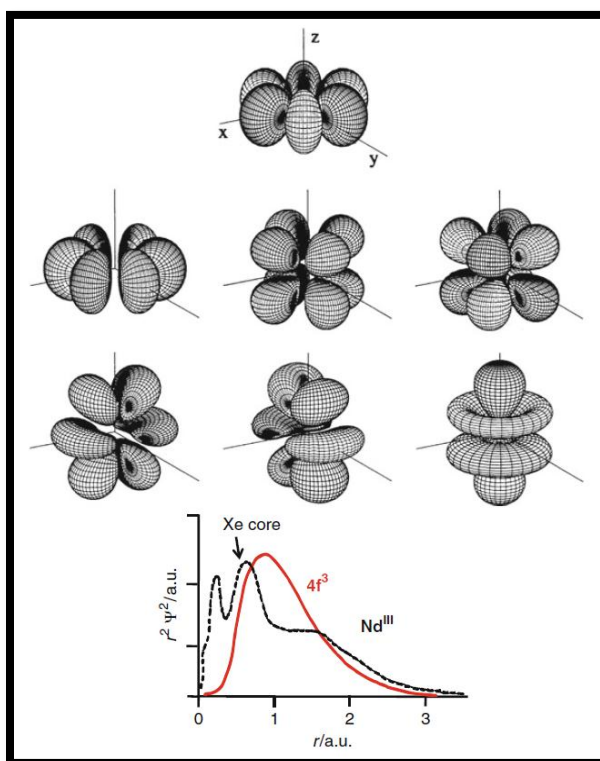


Figure 2.4: Top: Shape of the one-electron (hydrogenoid) 4f orbitals in a Cartesian space. Bottom: Radial wavefunction of the three 4f electrons of Nd^{III} compared with the radial wavefunction of the xenon core (a.u. = atomic units) [15].

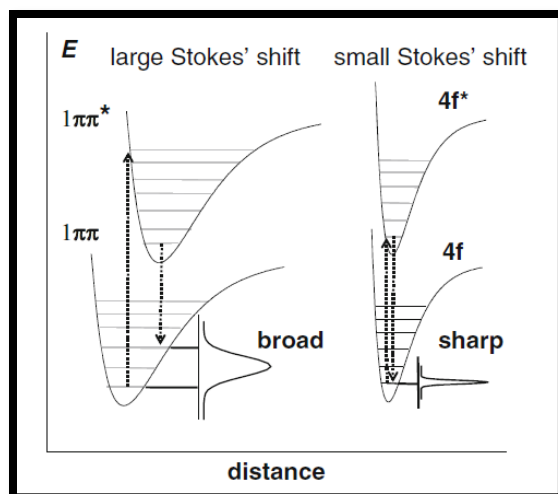


Figure 2.5: Configurational coordinate diagram for emission from (left) an organic chromophore and (right) a lanthanide ion [11].

Trivalent Terbium (Tb^{3+}) is one of the most investigated RE ion during the past decade [16-20]. It exhibits narrow emission lines in the UV and visible spectral region at 384, 416 and 438 due to $^5\text{D}_3 \rightarrow ^7\text{F}_J$ ($J=6,5,4$) transitions and at 493, 543, 584, 620, 700 nm due to $^5\text{D}_4 \rightarrow ^7\text{F}_J$ ($J=6,5,4,3,2$) respectively [21-24], it is also a promising material for white light phosphors. Dhlamini et al. [25], reported enhancement of cathodoluminescent (CL) intensity in Tb^{3+} ions due to sensitizing effect by ZnO nanoparticles, both embedded into SiO_2 matrix. Likewise, Mhlongo et al. [4] reported sol-gel synthesis of Pr^{3+} co-activated $\text{SiO}_2:\text{Eu}^{3+}/\text{Tb}^{3+}$. Furthermore, Yb^{3+} has not been intensively studied in the application of phosphors due to the fact that the current interest in this field is to produce white light phosphors and the lack of Yb ions is to exhibit very simple energy level scheme without absorption excited state. However, it exhibit interesting properties for applications in light emitting material such as in laser diode pumping where its large absorption cross-section is of primary importance. These properties may allow application in a variety of optical materials such as blue and UV light emitting devices [26,27], biological labeling and imaging [28,29], solar cells [30,31], and lasers [32].

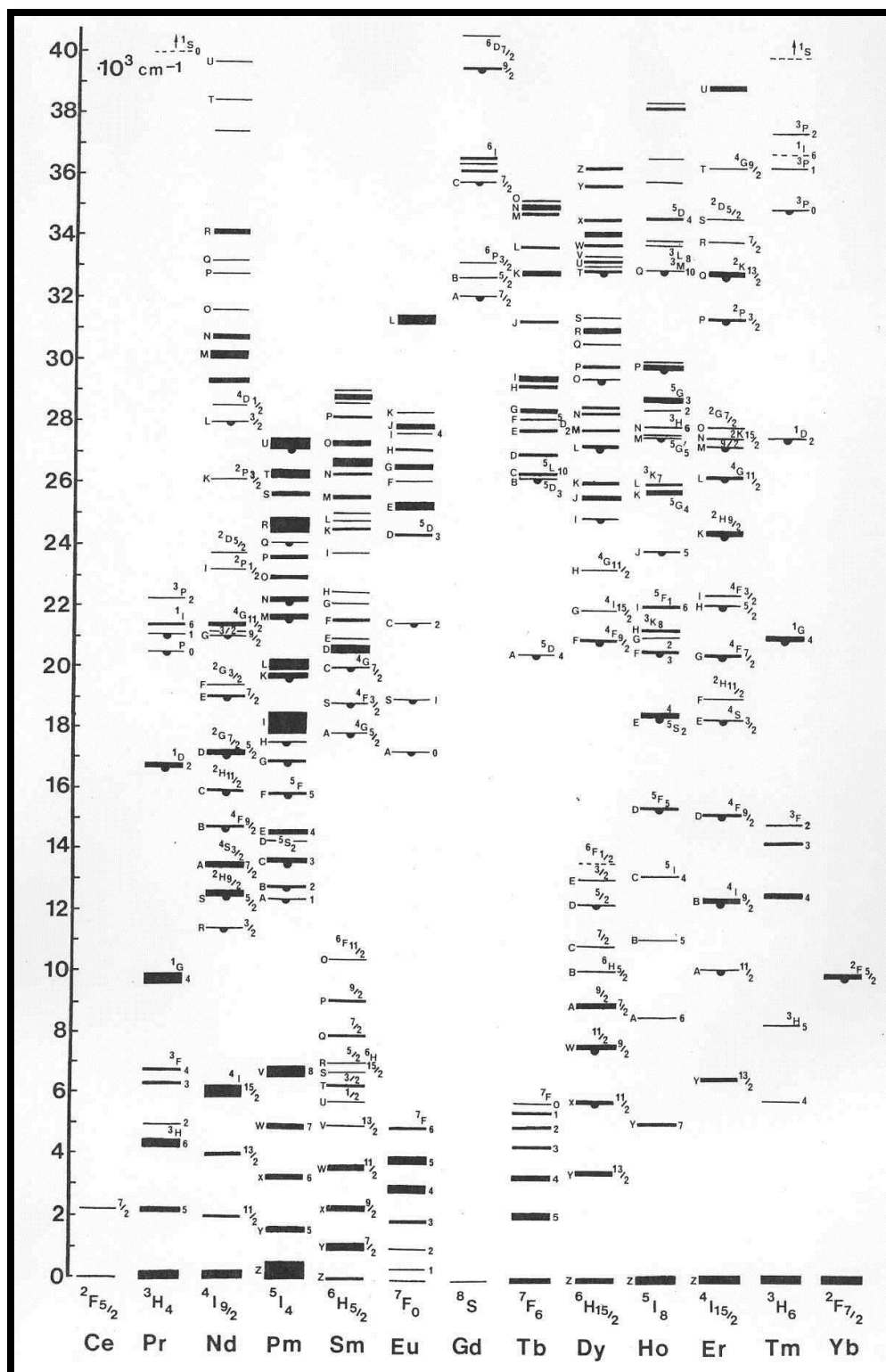


Figure 2.6: Energy-level diagram for trivalent lanthanide rare earth ions in lanthanum chloride (after Dieke, 1968) [33].

2.4 Zinc Oxide (ZnO)

2.4.1 Background

The semiconductor ZnO has gained considerable curiosity in the research community because of its large exciton binding energy (60 meV) that could lead to lasing action based on exciton recombination and possibly polariton / exciton interaction even above room temperature [34]. In this study, our interest on ZnO is motivated mainly by its wide direct band-gap (3.37 eV, RT) as shown in **figure 2.7**. The transitions $i = 1, 2, 3$ and 4 represent excitation, relaxation to the bottom of the conduction band, emission and filling the hole state vacated by electron excitation to the conduction band (process 1), respectively [34]. **Figure 2.8** shows the bulk ZnO band structure. Among a variety of theoretical approaches to calculate the band structure, X-ray or UV reflection/absorption have been used to measure the electronic core level in solids as well as the photoelectric effect which was basically extended to the X-ray region [34].

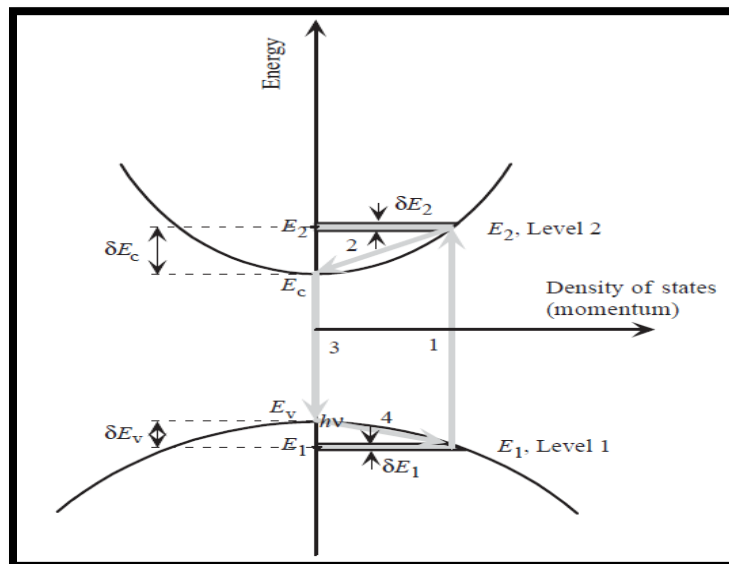


Figure 2.7: Optical transitions in a direct band-gap semiconductor on the energy versus momentum (which also represents energy versus density of states though the functional forms deviate) diagram, which is pumped beyond transparency [34].

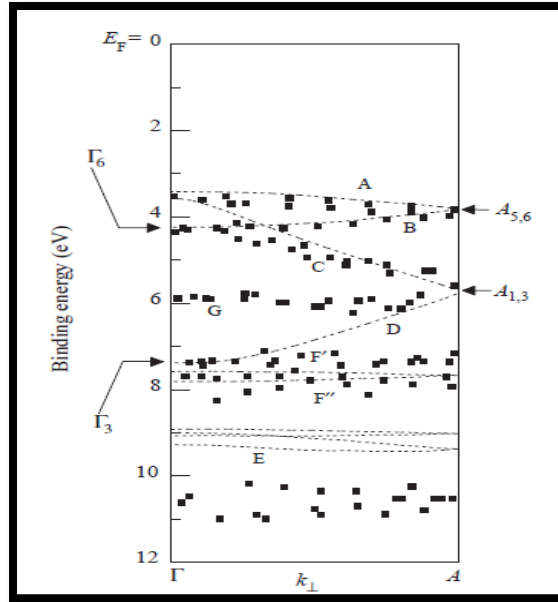


Figure 2.8: Bulk band structure of ZnO [34].

It is worth mentioning that there exist amorphous and crystalline semiconductors. However, the interest in the current study focus on crystalline semiconductors, especially ZnO. Its properties are discussed in the next section.

2.4.2 Crystal structure

As most of the group II–VI binary compound semiconductors, ZnO crystallize in either cubic zinc blende or hexagonal wurtzite (Wz) structure where each anion is surrounded by four cations at the corners of a tetrahedron, and vice versa [34]. This tetrahedral coordination is characteristic of Sp^3 covalent bonding nature, but these materials also have a substantial ionic character that tends to increase the band-gap beyond the one expected from the covalent bonding. ZnO is also well known as an II–VI compound semiconductor whose ionicity resides at the borderline between the covalent and ionic semiconductors [34].

The crystal structures shared by ZnO are wurtzite (B4), zinc blende (B3), and rocksalt (or Rochelle salt) (B1) as schematically shown in **figure 2.9**. B1, B3, and B4 denote the Strukturbericht designations for the three phases. Under ambient conditions, the thermodynamically stable phase is that of wurtzite symmetry. The zinc blende ZnO structure can be stabilized only by growth on cubic substrates, and the rocksalt or Rochelle salt (NaCl) structure may be obtained at relatively high pressures, as in the case of GaN [34]. The schematic representation of the most common crystallization state of ZnO, the wurtzite structure is shown in **figure 2.10** with details on the lattice parameters.

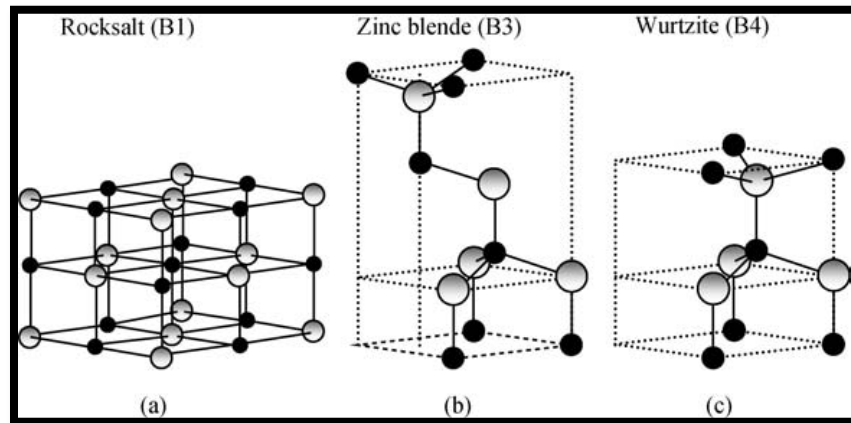


Figure 2.9: Stick-and-ball representation of ZnO crystal structures: (a) cubic rocksalt (B1), (b) cubic zinc blende (B3), and (c) hexagonal wurtzite (B4). Shaded gray and black spheres denote Zn and O atoms, respectively [34].

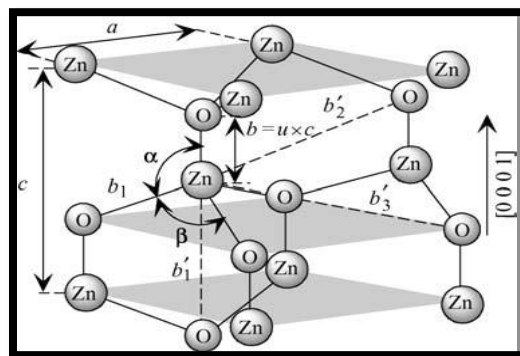


Figure 2.10: Schematic representation of a wurtzitic ZnO structure with lattice constants ' a ' in the basal plane and ' c ' in the basal direction, u parameter, which is expressed as the bond length or the nearest-neighbor distance b divided by c (0.375 in ideal crystal), a and b (109.47° in ideal crystal) bond angles, and three types of second-nearest-neighbor distances b [34].

The lattice parameters of ZnO can be expressed as follow [35],

$$a = \sqrt{1/3} \frac{\lambda}{\sin \theta}, \quad (2.3.1)$$

$$c = \frac{\lambda}{\sin \theta}. \quad (2.3.2)$$

From 'a' and 'c' the volume of the unit cell can be calculated,

$$V = 0.833 \times a^2 \times c \quad (2.3.3)$$

The Zn-O bond length L is given by [36]

$$L = \sqrt{\left[\frac{a^2}{3} + \left(\frac{1}{2} - u\right)^2 c^2\right]}, \quad (2.3.4)$$

Where 'u' in the wurtzite structure is given by

$$u = \left(\frac{1}{3}\right) \left(\frac{a}{c}\right)^2 + \frac{1}{2} \quad (2.3.5)$$

It should be pointed out that a strong correlation exists between the c/a ratio and the 'u' parameter in that when the c/a ratio decreases, the 'u' parameter increases [34].

The bond angles, α and β , are given by [37]

$$\alpha = \frac{\pi}{2} + \arccos\left[\left(\sqrt{1 + 3(c/a)^2(-u + 1/2)^2}\right)^{-1}\right] \quad (2.3.6)$$

$$\beta = 2\arcsin\left[\left(\sqrt{4/3 + 4(c/a)^2(-u + 1/2)^2}\right)^{-1}\right] \quad (2.3.7)$$

The lattice parameter for crystallographic systems in the present study can be calculated from the following equation using the (hkl) parameters and the interplanar d spacing. ZnO wurtzite is known to be a Hexagonal system [38].

$$\frac{1}{d_{hkl}^2} = \frac{4}{3} \left(\frac{h^2 + hk + k^2}{a^2} \right) + \frac{l^2}{c^2} \quad (2.3.8)$$

Where ‘ a ’ and ‘ c ’ are the lattice constants and h, k, l are the Miller indices along $x, y,$ and z -axis respectively.

2.4.3 Defects in ZnO

Typically, defects represent one of the controversial areas of semiconductors, and ZnO is no exception, as the measurement techniques are not able to correlate electrical or optical manifestation of defects to their origin specifically (see **figure 2.11**). It is highly suitable to say that the point defects in ZnO are not yet correctly understood. While several assignments of the defect-related luminescence bands can be found in literature, only a few of them are reliable. Over the years, oxygen vacancies were believed to be the main shallow donors in ZnO. Now it is becoming clear that these vacancies are formed in considerable concentrations after electron irradiation. In fact, Giles and co-workers have studied the electron paramagnetic resonance (EPR) of donors and acceptors in ZnO, they reported that the EPR signal with $g_{||} = 1.9945$ and $g_{\perp} = 1.9960$ could not be assigned to singly ionized oxygen vacancies as reported in several studies for some reasons. The main reason is that this EPR signal could only be observed by irradiating a crystal with high-energy electrons or neutrons [34,39].

As another vital misassignment till now, the green luminescence band in ZnO is commonly attributed to transitions from the oxygen vacancy (V_O) to the valence band. However, it is easy to show that such transition is highly unlikely in n-type ZnO [34].

The neutral impurities such as interstitial zinc (Zn_i) and oxygen vacancy (V_O) compose shallow delocalized donor states that are located 0.05 eV below the conduction band [40]. Divalent zinc

vacancy (V_{Zn}^{2-}) and monovalent interstitial zinc (Zn_i^+) provide donor states, which lie below the conduction band from 0.4 to 0.7 eV [41,42]. The monovalent vacancies of zinc (V_{Zn}^{1-}) and oxygen (V_O^+) act as acceptors with an energy level of 0.3 – 0.7 eV and 1.2–1.5 eV respectively above the valence band (see **figure 2.12**) [40,41].

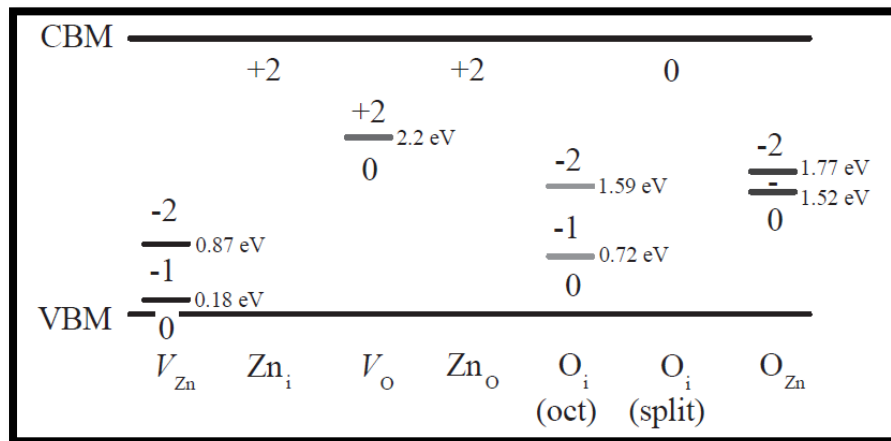


Figure 2.11: Thermodynamic transition levels for native defects in ZnO [42].

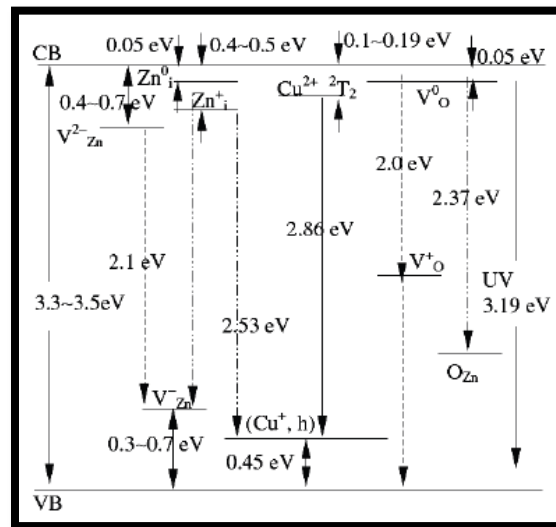


Figure 2.12: Electron energy level diagram of the defects in ZnO:Cu nanoparticles [43].

A variety of nanostructures are currently under intensive investigation among the scientific community, the next section focuses on semiconductor nanocrystals or quantum dot. Some of the main properties governing quantum dots are discussed.

2.4.4 ZnO Quantum dots

A crystalline material which is confined in three dimensions such that the energy levels become discrete enough is called a quantum dot (QDs) also known as semiconductor nanocrystals, see **figure 2.13**. Due to this confinement the electronic and optical properties of quantum dots are related to their size and shape in the nanometer regime [44,45]. Knowing that the confinement occurs when the size of the particle is near the bohr exciton radius, Fonoberov et al. have determined the exciton Bohr radius a_B in bulk ZnO to be about 0.9 nm, thus the size of the considered QDs should be two to three times larger than the size of the bulk exciton [46]. The Bohr radius of the exciton which is the distance between the electron and the hole is given by,

$$a_B = \frac{4\pi\epsilon_0\epsilon_\infty\hbar^2}{m_0e^2} \left(\frac{1}{m_e^*} + \frac{1}{m_h^*} \right) \quad (2.3.8)$$

in which m_e^* and m_h^* are the effective electron and hole masses, respectively, and ϵ_∞ is the high-frequency relative dielectric constant of the medium, m_0 the electron mass at rest, \hbar is the reduced Planck's constant, e is the electronic charge, and ϵ_0 is the optical dielectric constant in vacuum.

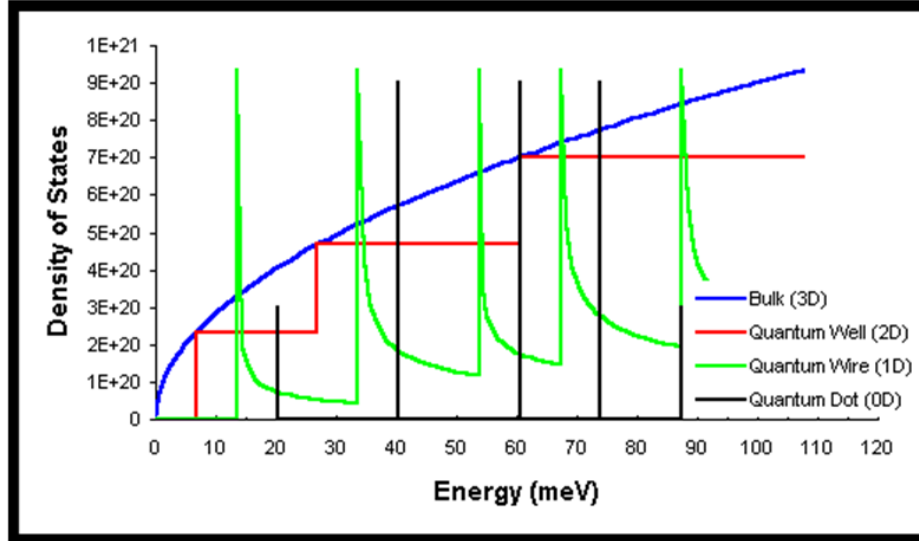


Figure 2.13: Density of states functions plotted against energy for bulk (3D blue), quantum well (2D red), quantum wire (1D green) and quantum dot (0D black) [47].

2.4.4.1 Effective Mass Approximation (EMA) for quantum dots

There exist numerous methodologies to understand and elucidate quantum confinement effects quantitatively. In the current study, the commonly most accepted so-called effective mass approximation (EMA) model is discussed.

Using the effective mass approximation, the hamiltonian of a particle at nanoscale can be expressed as follow [48].

$$H = \left[\frac{-\hbar^2}{2m_e^*} \nabla_e^2 - \frac{\hbar^2}{2m_h^*} \nabla_h^2 - \frac{e^2}{\epsilon_0 |r_e - r_h|} \right] + \text{polarization terms} \quad (2.3.9)$$

In order to obtain a correct calculation of columbic interaction the formed amounts of “two polar substances” within the area separating the nanoparticle surface and the engraved substance must be calculated. For this reason polarization terms have been involved in the equation. Therefore the result would be as follow, by solving eigen value for hamiltonian [49]:

$$E_g(QD) = E_g(bulk) + \frac{\pi^2 \hbar^2}{2\mu R^2} - 1.786 \frac{e^2}{\epsilon R} - 0.248 E_{RY}^* \quad (2.3.10)$$

Where $\frac{1}{\mu} = \frac{1}{m_e^*} + \frac{1}{m_h^*}$

m_e^* and m_h^* are electron's and hole's effective masses, respectively, and 'R' is the radius of QD, μ is the reduced mass, ' ϵ ' is the permittivity of the vacuum and E_{RY}^* is the effective Rydberg energy.

From the above equation it can be concluded that the energy gap of nanoparticle will always increase with decreasing the diameter (see **figure 2.14**).

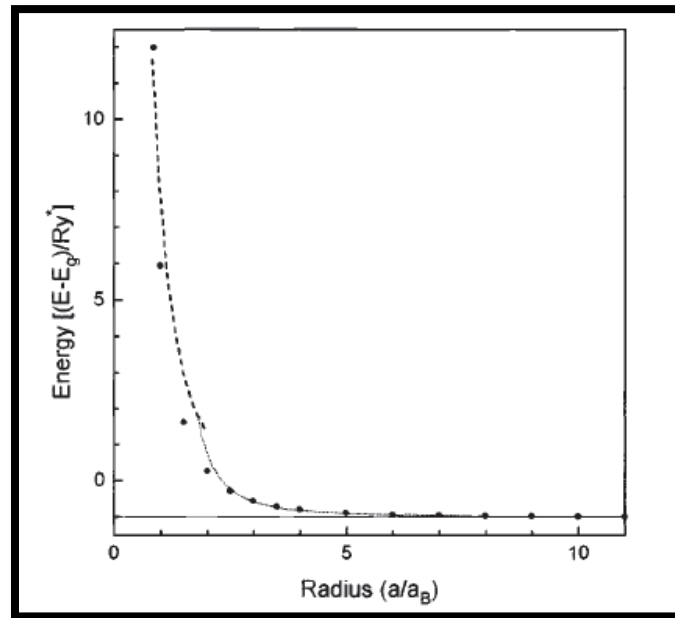


Figure 2.14: Size dependence of the energy gap of the first allowed dipole optical transition in an ideal quantum dot [50].

2.4.4.2 Surface effect

In pure semiconductor, the surface undergoes substantial reconstructions in the atomic positions, and it is almost inexorable that there exist energy levels (surface states) within the energetically forbidden gap of the bulk solid [51,52] due to the surface non-stoichiometry, unsaturated bonds,

etc. In addition, a degradation of the electrical and optical properties of the material is observed, resulting from the trapping of electrons or holes at the surface states. It is however noticed that in a number of cases the surface states can also be involved in radiative transition. Moreover, the relatively large surface to volume ratio in semiconductor nanocrystals results in strong influence of the surface states on their optical properties [53] and with decreasing particle size, the fraction of the surface molecules aggregates increases [54]. This indicates the state of imperfection of the surface which can act as trapping centres for photogenerated electrons and holes. Moreover, surface atoms have reduced amount of bonds in comparison to the atoms in the bulk because of the loss in nearest neighbors. In this regard, they tend to find new equilibrium positions to balance the forces, resulting in surface reconstruction and defects [55].

2.5 Energy transfer in phosphors

2.5.1 Background

In order to effectively understand the photoluminescence efficiency of the semiconductor nanocrystals phosphors, a nonradiative energy transfer process between semiconductor nanoparticles over the matrix was investigated. Energy transfer between dopants and hosts plays an important role in phosphors technology.

The universally conventional mechanism of energy transfer from the organic ligands to the lanthanide ion was studied and suggested by Crosby and Whan, see **figure 2.15** [56-58]. In their study, as a result of irradiation with ultraviolet radiation, the organic ligands of the lanthanide complex was excited to a vibrational level of the first excited singlet state ($S_1 \leftarrow S_0$) (**figure 2.15**) [7]. The molecule then experiences fast internal conversion to lower vibrational levels of the S_1

state, for instance, through interaction with solvent molecules. He noticed that the excited singlet state was deactivated radiatively to the ground state (molecular fluorescence, $S_1 \rightarrow S_0$) or could experience nonradiative intersystem crossing from the singlet state S_1 to the triplet state T_1 (**figure 2.15**) [7]. Moreover, the triplet state T_1 could be deactivated radiatively to the ground state, S_0 , by the spin forbidden transition $T_1 \rightarrow S_0$, which result was assigned to molecular phosphorescence [7].

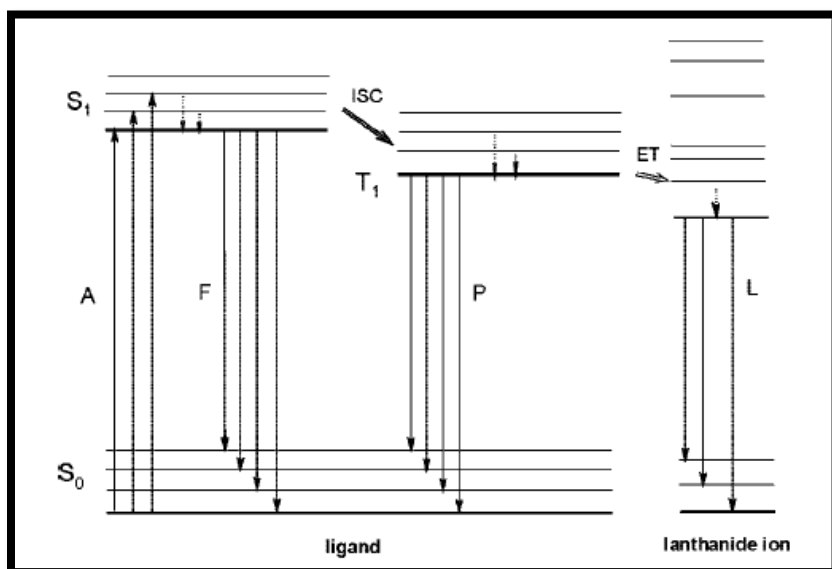


Figure 2.15: Schematic representation of photophysical processes in lanthanide (III) complexes (antenna effect). Abbreviations: A) absorption; F) fluorescence; P) phosphorescence; L) lanthanide-centered luminescence; ISC) intersystem crossing; ET) energy transfer; S) singlet; T) triplet. Full vertical lines indicate radiative transitions; dotted vertical lines indicate nonradiative transitions [7].

Energy transfer between a sensitizer ion (S) and an activator ion (A) can be written as a chemical reaction [59]:



where the asterisk indicates the excited state.

2.5.2 Mechanism of energy transfer

In the energy transfer process, both sensitizer and activator ions have to interact physically. It is however evident that the energy transfer find its origin in electrostatic and exchange interaction. Furthermore, both emission and absorption spectra of the sensitizer and activator ions, respectively, have to show spectral overlap, this, targeting energy conservation. The probability W_{et} for energy transfer is given by the following relation [59]:

$$W_{et} = \left(\frac{2\pi}{\hbar(\rho)} \right) \cdot [\varphi_i | \mathbf{H} | \varphi_f]^2 \quad (2.4.2)$$

where, φ_i is the wave function of the initial state, φ_f is the wave function of the final state, ρ is a measure for the density of initial and final states capable of interaction, and \mathbf{H} is the operator coupling the initial and final state. ρ is given by

$$\rho = \int g_S(E) \cdot g_A(E) dE \quad (2.4.3)$$

representing the spectral overlap between sensitizer and activator ions. $g_S(E)$ and $g_A(E)$ are the normalized optical line shape functions for the sensitizer and the activator ions, respectively.

Hence, the probability per unit time for energy transfer can be written as

$$W_{et} = \left(\frac{2\pi}{\hbar(\rho)} \right) \cdot \left\{ [\varphi(S^*)\varphi(A) | \mathbf{H}_c | \varphi(S)\varphi(A^*)]^2 + [\varphi(S^*)\varphi(A) | \mathbf{H}_e | \varphi(S)\varphi(A^*)]^2 \right\} \quad (2.4.4)$$

The matrix elements for Coulomb interaction represent the repulsive electrostatic interaction between the electronic charge distributions in the initial and final state, respectively, and have the following shape [59]:

$$Q_i^c = \varphi_{S^*}(1)\varphi_A(2) \text{ and } Q_f^c = \varphi_S(1)\varphi_{A^*}(2) \quad (2.4.5)$$

The matrix elements for exchange interaction represent the repulsive electronic interaction of the electronic charge distributions have the shape below [59]:

$$Q_i^e = \varphi_{S^*}(1)\varphi_A(2) \text{ and } Q_f^e = \varphi_S(2)\varphi_{A^*}(1) \quad (2.4.6)$$

Figure 2.16 presented and compared the electronic energy transfer by Coulomb and exchange interaction. In the first case, whereby the Coulomb interaction govern, the electrons initially on the excited donor stay there, and the electrons initially on the acceptor also remain there [59]. It can then be concluded that this interaction does not require physical contact between the interacting partners; it is sufficient that the excited sensitizer ion induces a dipole oscillation on the activator ion. In the case of energy transfer ruled by exchange interaction, the way the energy is transferred can be visualized by a double electron substitution reaction: the excited electron on S* travels to A, while one electron on A goes to S. This second type of interaction necessitates overlap of the electronic charge distribution, i.e. physical contact between the sensitizer ion and the activator ion [59].

The most common processes that govern energy transfer mechanism are:

- a) Electrostatic interaction
- b) Higher-order Coulomb interaction
- c) Exchange interaction
- d) Cross-relaxation

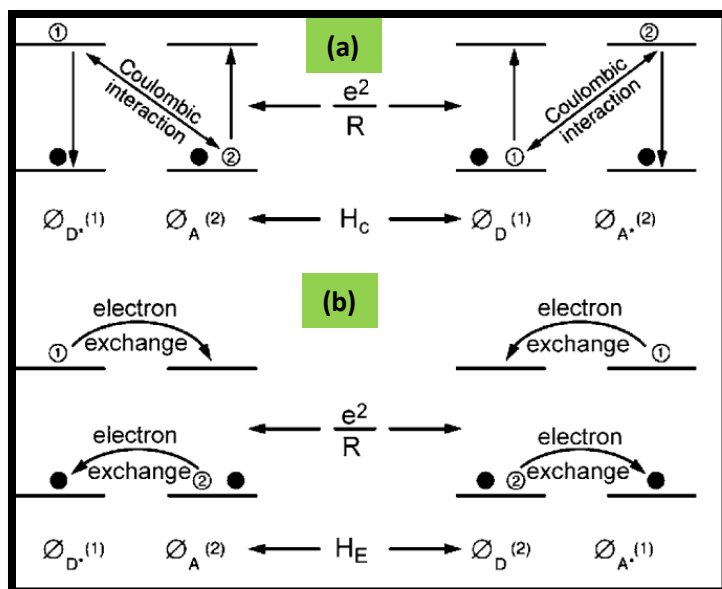


Figure 2.16: Visualization of energy transfer by Coulomb interaction (a) and exchange interaction (b) between two ions [59].

On the other hand, from a theoretical point of view, other factors or parameters may intervene in the wide description of the energy transfer mechanism. Once the ligand is excited, subsequent intramolecular energy migrations obey Fermi's golden rule governing resonant energy transfer, whereby W_{DA} is the probability of energy transfer, Ω_{DA} is the spectral overlap integral between the absorption spectrum of the acceptor A and the emission spectrum of the donor D , while H' is the perturbation operator in the matrix element $\langle D^*A | H' | DA^* \rangle$ [11].

$$W_{DA} = \left(\frac{4\pi^2}{h} \right) \cdot |\langle D^*A | H' | DA^* \rangle|^2 \cdot \Omega_{DA} \quad (2.4.7)$$

Depending on the electromagnetic nature of \mathcal{H}' , a double-electron exchange (Dexter) mechanism or an electrostatic multipolar (Forster) mechanism have been proposed and theoretically modelled. They are sketched on **figure 2.17**, for the simple $1S^* - 3T^* - Ln^*$ path. Their specific dependences on the distance d separating the donor D from the acceptor A , i.e., $e^{-\beta d}$

for double-electron exchange and d^6 for dipole–dipolar processes, respectively, often limit Dexter mechanism to operate at short distance (typically 30–50 pm) at which orbital overlap is significant, while Forster mechanism may extend over much longer distances (up to 1,000 pm) [11].

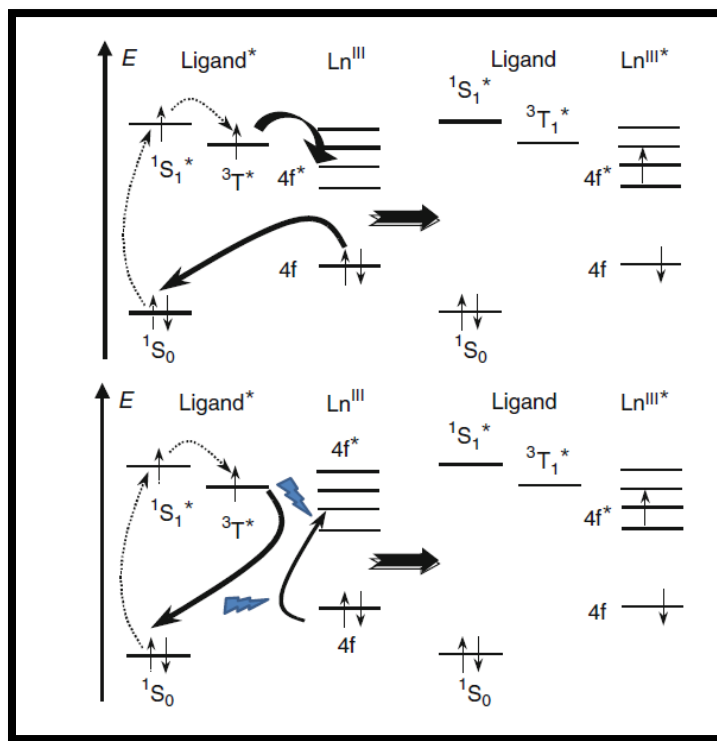


Figure 2.17: Dexter (top) and Forster (bottom) energy transfer mechanisms [11].

2.6 Photoluminescence related Properties

The current section discusses the properties and related process of interest that occurs in activated phosphors.

2.6.1 Concentration quenching

In the case of a high concentration of an activator, which exceeds its optimum concentration, the emission intensity of the phosphor vanishes [60-64]. This phenomenon is known as

“concentration quenching”. The quenching starts to occur at a certain concentration, for which there is a sufficient reduction in the average distance between these centres to favour energy transfer [61]. Concentration quenching is attributed to pairing or aggregation of the activator ions allowing some of them to act as killer centres thus creating a non-radiative pathway. A number of scientists have ascribed concentration quenching effect to energy transfer from one ion to another and finally to energy sink [60,63]. This strongly suggests that concentration quenching related to interaction allows the absorbed excitation energy to reach particular quenching centres such that the critical concentration depends on the probability of the transfer [4].

2.6.2 Killer centers

Killers are defects produced by incidental impurities and characteristic lattice defects that reduce the luminescence intensity of a phosphor [65]. The atoms and molecules adsorbed at the surface of a phosphor may reduce luminescence by producing a non-luminescent layer when they react with ambient vacuum species. The Killer centres exist in two types, namely, the bypassing and the resonance energy transfer type. The bypassing type is known to compete with activator ions in capturing free carriers by so allowing them to recombine non-radiatively. This type can only take place when free electrons and free holes are generated in the conduction band and valance band, respectively. The resonance energy transfer takes away the energy from the activator ion through resonance energy transfer. It occurs at any time and does not require the presence of free carriers to reduce the luminescence [66].

2.6.3 Absorption coefficient

The absorption coefficient $\alpha(\hbar\omega)$ is strictly connected with the electronic density of state (DOS) and band structure of a material. According to the Fermi's Golden Rule, the probability per unit time and volume, $R(\hbar\omega)$, that a given system will absorb an incoming photon of energy $\hbar\omega$ with the transition of an electron from the valence band, VB, to the conduction band, CB, given by

$$R(\hbar\omega) = \frac{2\pi}{\hbar} \sum_{k_{CB}, k_{VB}} |\langle CB | H_{eR} | VB \rangle|^2 \cdot \delta [E(k_{CB}) - E(k_{VB}) - \hbar\omega] . \quad (2.5.1)$$

$E(k_{CB})$ [$E(k_{VB})$] gives the energy dispersion of the conduction (valence) band. However, the Hamiltonian H_{eR} accounts for the electron–radiation interaction, and the term $|\langle CB | H_{eR} | VB \rangle|^2$ is the probability for an electron in a valence band state $|VB\rangle$ to be excited into a conduction band state $|CB\rangle$ by absorbing a photon [2].

The absorption coefficient of the material, $\alpha(\hbar\omega)$, is defined through the Lambert relation $dI / dx = -\alpha(\hbar\omega)I$, which yields $I(x, \hbar\omega) = I(0, \hbar\omega) e^{-\alpha(\hbar\omega)x}$, where $I(x, \hbar\omega)$ is the intensity of the electromagnetic radiation as it has propagated through a distance x in the material. $\alpha(\hbar\omega)$ is connected to $R(\hbar\omega)$ through the relation

$$\alpha(\hbar\omega) = \frac{8\pi}{c \cdot n} \cdot \frac{\hbar\omega}{|\varepsilon(\hbar\omega)|^2} \cdot R(\hbar\omega) \quad (2.5.2)$$

Where n is the refractive index of the material. Then

$$\alpha(\hbar\omega) = \frac{\hbar}{c \cdot n} \left(\frac{2\pi e}{m} \right)^2 \cdot \frac{1}{\hbar\omega} \cdot |P_{VB, CB}|^2 \sum_{k_{CB}, k_{VB}} \delta [E(k_{CB}) - E(k_{VB}) - \hbar\omega] . \quad (2.5.3)$$

If the summation over k is replaced by an integral, we obtain

$$\alpha(\hbar\omega) = \frac{\hbar}{c.n} \left(\frac{2\pi e}{m} \right)^2 \cdot \frac{1}{\hbar\omega} \cdot |P_{VB,CB}|^2 \int_{BZ} \frac{d^2k}{4\pi^3} \cdot \delta[E(k_{CB}) - E(k_{VB}) - \hbar\omega]. \quad (2.5.4)$$

The integral (2.5.4) resembles an electronic DOS and can be defined directly in terms of the gradient of the difference between the energy dispersion of the conduction and valence bands,

$E_{CV}(k) = E(k_{CB}) - E(k_{VB})$. Thus [2]

$$\alpha(\hbar\omega) = \frac{\hbar}{c.n} \left(\frac{2\pi e}{m} \right)^2 \cdot \frac{1}{\hbar\omega} \cdot |P_{VB,CB}|^2 \int_{S_{CV}(\hbar\omega)} \frac{dS}{4\pi^3} \cdot \frac{1}{|\nabla E_{CV}(k)|}. \quad (2.5.5)$$

2.6.4 Quantum yield

The *luminescence quantum yield* φ is an important parameter for the evaluation of the efficiency of the emission process in luminescent materials. The quantum yield is defined as the ratio of the number of emitted photons to the number of absorbed photons per time unit [67]:

$$\varphi = \frac{\text{number of emitted photons}}{\text{number of absorbed photons}} \quad (2.5.6)$$

For luminescent lanthanide complexes, the *overall luminescence quantum yield* Φ_{tot} , upon excitation of the ligands is determined by the efficiency of sensitization or energy transfer (η_{sens}) and by the quantum yield of the lanthanide luminescence step (φ_{Ln}) [68]:

$$\Phi_{tot} = \eta_{sens} \cdot \varphi_{Ln}. \quad (2.5.7)$$

φ_{Ln} is called the *intrinsic luminescence quantum yield*, and it is the quantum yield determined by direct excitation in the 4f levels of the Ln^{3+} ion.

The intrinsic quantum yield can be determined using the equation:

$$\varphi_{Ln} = \frac{\tau_{abs}}{\tau_{Rad}}. \quad (2.5.8)$$

The observed lifetime, τ_{abs} , can be derived from intensity decay curves.

The nonradiative processes influence the *observed luminescence lifetime* τ_{abs} , whereas they do not influence the *radiative lifetime*, τ_{Rad} ($=1/k_T$). The *radiative lifetime* is the lifetime of an excited state in the absence of nonradiative transitions. Although sometimes the term “natural lifetime” is used instead of “radiative lifetime”, the former term should be abandoned [7]. The stretched exponential decay is generally described for luminescence decays as follows [69-71],

$$P = \exp(-(t/a)^b) \quad (2.5.9)$$

where P is the normalized intensity of luminescence varying with time t , a is the characteristic life, especially indicating the time of $P = \exp(-1)$, and b is the stretched exponent.

Generally, Luminescent materials with quantum yield higher than 80%, are considered as efficient phosphors [72].

2.6.5 Franck–Condon principle

Classically, the Franck–Condon principle shown in **figure 2.18** is the approximation that an electronic transition is most likely to occur without changes in the positions of the nuclei in the molecular entity and its environment. The resulting state is called a Franck–Condon state, and the transition involved a vertical transition. The quantum mechanical formulation of this principle is that the intensity of a vibronic transition is proportional to the square of the overlap integral between the vibrational wavefunctions of the two states that are involved in the transition [73].

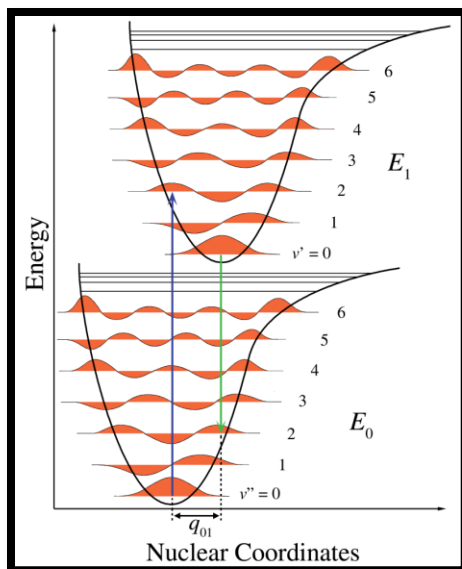


Figure 2.18: A schematic representation of the Franck-Condon principle [73]. The upward arrow indicates the most favoured vibronic (i.e., both vibrational and electronic) transition predicted by the Franck-Condon principle [74].

2.7 Applications

Nanotechnology and in particular nanofabrication, offers a variety of tools to contribute to solving the energy crisis, since creating materials and devices smaller than 100 nanometers (nm) offers new ways to capture, store, and transfer energy [75]. The level of control that nanofabrication provides could help solve many of the problems that the world is facing related to the current generation of energy technologies, including the array of alternative, renewable energy approaches [75,76]. Luminescence through nanotechnology offers a variety of potential applications from electronics, optical communications and biological systems to new advanced materials. A wide range of possible applications have been explored and many devices and systems have been studied such as Solar cells [77-78], Biological imaging and labelling [79], Optoelectronic devices [80], Solid state lighting and white LEDs [81], Electronic devices [82],

gas sensors [83], spintronics [84], nanolasers [85], optical amplifiers [86] as well as Water purification [87-88].

This interdisciplinary technology will provide a broad platform for medicine, industry and the overall economy [89]. This technology is expected to become one of the biggest driving forces in the research of material science in the 21st century [90]. Most of the applications that are derived from nanomaterials are still in an early stage of development and much work must still be done on this new field in science [91].

2.8 References

- [1] <http://en.wikipedia.org/wiki/Phosphor>, [Accessed, 13 April 2013]
- [2] Pettinari G, Polimeni A, and Capizzi M, *Photoluminescence: A Tool for Investigating Optical, Electronic, and Structural Properties of Semiconductors*. A. Patane and N. Balkan (eds.), Semiconductor Research, Springer Series in Materials Science 150, Springer-Verlag Berlin Heidelberg (2012)
- [3] Vij DR, *Luminescence of Solids*, Plenum Press, New York, (1998)
- [4] Mhlongo GH, *Luminescence investigation of trivalent rare earth ions in sol-gel derived SiO₂ and ZnO co-doped SiO₂:Pr³⁺*, 2011, [PhD Thesis], University of the Free State, South Africa
- [5] Stephen B Castor and James B Hedrick, Rare Earth Elements, http://www.fieldexploration.com/images/property/1_RareEarths_FLX_02.pdf, [Accessed, 25 April 2013]
- [6] <http://www.reehandbook.com/intro.html>, [Accessed, 25 April 2013]
- [7] Binnemans K, *Lanthanide-Based Luminescent Hybrid*, *Mater Chem Rev* **109** (9) (2009)
- [8] Reisfeld R, *Mater Sci* **20** (2002)
- [9] Binnemans K, Gorller-Walrand C, *Chem Phys Lett* **235** (1995) 163
- [10] Dieke GH, *Spectra and Energy Levels of Rare Earth Ions in Crystals*, Interscience Publishers: New York (1968)
- [11] Jean-Claude G. Bunzli and Svetlana V. Eliseeva, *Basics of Lanthanide Photophysics in Lanthanide Luminescence: Photophysical, Analytical and Biological Aspects*, Springer SerFluoresc, Springer-Verlag Berlin Heidelberg (2010)
- [12] Petoud S, Cohen SM, Bunzli J-C G, Raymond KN, *J Am Chem Soc* **125** (2003) 13324
- [13] Zhang JP, Badger PD, Geib SJ, Petoud S, *Angew Chem Int Ed Engl* **44** (2005) 2508
- [14] Adrienne Michelle Yingling, 2009, [PhD Thesis], University of Pittsburgh, USA
- [15] Liu G, Jacquier B, Spectroscopic properties of rare earths in optical materials,(2005), Tsinghua University Press & Springer, Beijing & Heidelberg
- [16] Bayan S, Das U and Mohanta D, *Phys Status Solidi A* **207** (2010) 1859
- [17] Li G-R, Lu X-H, Su C-Y and Tong Y-X, *J Phys Chem C* **112** (2008) 2927
- [18] Liu S-M, Liu F-Q, Guo H-Q, Zhang Z-H and Wang Z-G, *Phys Lett A* **271** (2000) 128

- [19] Cetin A, Kibar R, Selvi S, Townsend PD and Can N, *Physica B* **404** (2009) 3379
- [20] Sun L, Jiang S and Marciante JR, *Opt Express* **18** (2010) 12191
- [21] Podhorodecki A, Gaponenko NV, Banski M, Kim T and Misiewicz J, *ECS transactions* **28** (2010) 81
- [22] Pal Partha P and Manam, *J Mater Sci Eng B* **178** (2013) 400
- [23] Sharma A, Dhar S, Singh BP and Kundu T, (2011) IEEE Xplore doi : 978-1-4577-2037-6/11
- [24] Liu S-M, Liu F-Q and Whang Z-G, *Chem Phys Letters* **343** (2001) 489
- [25] Dhlamini MS, Ntwaeaborwa OM, Swart HC, Ngaruiya JM and Hillie KT, *Physica B* **404** (2009) 4406
- [26] Reynolds DC, Look DC, Jogai B, Litton CW, Collins TC, Harsch W, Cantwell G, *Phys Rev B* **57** (1998) 12151
- [27] Debasis Bera et al., *Materials* **3** (2010) 2260
- [28] Cassidy PJ, Radda GK, *J R Soc Interface* **2** (2005) 113
- [29] Coe-Sullivan S, *Nat photonics* **3** (2009) 315
- [30] Rensmo H, Keis K, Lindstrom H, S. So dergren, Solbrand A, Hagfeldt A, Lindquist SE, Muhammed M, *J Phys Chem B* **101** (1997) 2598
- [31] Olson DC, Pitris J, Collins RT, Shaheen SE, Ginley DS, *Thin solid films* **496** (2006) 26
- [32] Ma XY, Chen PL, Li DS, Zhang YY, Yang DR, *Appl Phys Lett* **91** (2007) 251109
- [33] Dieke G, *Spectra and energy levels of rare earth ions in crystals*. 1968, New York, USA: John Wiley & Sons, Inc.
- [34] *Zinc Oxide: Fundamentals, Materials and Device Technology*. Edited by Hadis Morkoç and Ümit Özgür Copyright 2009 WILEY-VCH Verlag GmbH & Co. KGaA, Weinheim, ISBN: 978-3-527-40813-9
- [35] Muhammad Saleem, Liang Fang, Aneela Wakeel, M. Rashad, C. Y. Kong, World *J Cond Matter Physics* **2** (2012) 10
- [36] Barret CS, Massalski TB, *Structure of Metals*, Pergamon Press, Oxford, 1980
- [37] Ambacher O, Majewski J, Miskys C, Link A, Hermann M, Eickhoff M, Stutzmann M, Bernardini F, Fiorentini V, Tilak V, Schaff B And Eastman, LF, *Pyroelectric properties of Al(In)GaN/GaN hetero and quantum well structures*, *J Phys: Conde Matter* **14** (2002) 3399

- [38] *Introduction to solid state physics* by Kittel Chap: 2 p-19.
- [39] Giles NC, Garces NY, Lijun Wang, and Halliburton LE, *Proc. of SPIE* **5359** (2004) doi: 10.1117/12.528094
- [40] Lima SAM, Sigoli FA, Jafelicci M Jr and Davolos MR, *Int J Inorg Mater* **3** (2001) 749
- [41] Lin B and Fu Z, *Appl Phys Lett* **79** (2001) 943
- [42] Tsurkan AE, Fedotova ND, Kicherman LV and Pasko PG, *Semiconductors* **6** (1975) 1183
- [43] Xu CX, Sun XW et al. "Photoluminescent properties of copper-doped zinc oxide nanowires." *Nanotechnology*, **15** (2004) 856
- [44] Gaponenko SV, *Optical Properties of Semiconductor Nanocrystals*, Cambridge University Press, United States of America (1998)
- [45] MRS Bulletin, february (1998)
- [46] Fonoberov and Balandin, *J Nanoelectron Optoelectron* **1** (2006) 19
- [47] Brittney Spears, Guide to Semiconductor Physics." <http://britneyspears.ac/physics/dos/dos.htm> [Accessed, 13 October 2013]
- [48] Haug H and Khoch SW, *Quantum Theory of the Optical and Electrical Properties of Semiconductors* (World Scientific Publishing Co. Pte. Lid (1993)
- [49] Changiz Vatankhah and Ali Ebadi, *Res J Recent Sci* **2** (1) (2013) 21
- [50] Gaponenko SV, *Optical Properties of Semiconductor Nanocrystals*, Cambridge University Press (1998)
- [51] Yang H, 2003, [PhD Thesis], University of Florida, Florida, USA
- [52] Rama J and Pino R, Physical Chemistry: Energy Band Theory and quantum Confinement, Meliorum Technologies Inc., NY USA 14607, http://www.meliorum.com/Meliorum_Technol. [Accessed, 13 October 2013]
- [53] Guo L, Wu Z, Ai X, Li Q, Zhu H, Yang S, *Opt Mater* **14** (2000) 247
- [54] Chakraborty I, Moulik SP, *Journal of Nanoparticle Research* **6** (2004) 233
- [55] Dhlamini MS, *Luminescent properties of Synthesized PbS nanoparticles phosphors*, 2008, [PhD Thesis], University of the Free State, South Africa
- [56] Whan RE, Crosby GA, *J Mol Spectrosc* **8** (1962) 315
- [57] Crosby GA, Whan RE, Alire RM, *J Chem Phys* **34** (1961) 743
- [58] Crosby GA, Whan RE, Freeman JJJ, *Phys Chem* **66** (1962) 2493

- [59] *Luminescence: From Theory to Applications*. Edited by Cees Ronda Copyright(2008)
WILEY-VCH Verlag GmbH & Co. KGaA, Weinheim, ISBN: 978-3-527-31402-7
- [60] Donega C de Mello, Meijerink A and Blasse G, *J Appl Spectrosc* **62** (4) (1995)
- [61] Ferrari JL, Pires AM, Davolos MR, *Mater Chem Phys* **113** (2009) 587
- [62] Satoh Y, Najafov H, Ohshio S and Saitoh H, *Adv Tech Mater Process* **17** (1) (2005) 43
- [63] Zhang X, Qiao X, Seo HJ, *Curr Appl Phys* **11** (2010) 442
- [64] Pang Q, Shi J, and Gong M, *J Am Ceram Soc* **90** (2007) 3943
- [65] Tannas LE, Glenn WE, and Doane JW, *Flat-Panel Display Technologies*, Noyes
Publications: New Jersey (1995)
- [66] Garlick GFJ, *J Appl Phys* **13** (1962)
- [67] Fery-Forgues S and Lavabre D, *J Chem Educ* **76** (1999) 1260
- [68] Werts MHV, Jukes RTF, Verhoeven JW, *Chem Phys* **4** (2002) 1542
- [69] Fatkullin I, Kladko K, Mitkov I, and Bishop AR, *Phys Rev E* **63** (2011) 067102
- [70] Weon BM and Je JH, *J Appl Phys* **97** (2005) 036101
- [71] Weon BM and Je JH, *Appl Surf Sci* (doi:10.1016/j.apsusc.2005.03.164)
- [72] Mothudi BM, *Synthesis and Characterization of Strontium (Sr), Barium (Ba) and Calcium
(Ca) Aluminate Phosphors Doped with Rare Earth Ions*, 2009, [PhD Thesis], University of
the Free State, South Africa
- [73] Franck-Condon principle, <http://goldbook.iupac.org/F02510.html>,
[Accessed, 14 Feb. 2013]
- [74] Ji S, “*Molecular Theory of the Living Cell: Concepts, Molecular mechanisms, and
Biomedical Applications*”, Springer, New York, (2012)
- [75] <http://www.npep.co.za/> , [Accessed, 12 May 2012]
- [76] Biggs MM, 2009, [MSc thesis], University of the Free State, South Africa
- [77] Jiang Tang, Kyle M Kemp, Sjoerd Hoogland, Kwang S Jeong, Huan Liu, Larissa
Levina, Melissa Furukawa, Xihua Wang, Ratan Debnath, Dongkyu Cha, Kang Wei Chou, Armin
Fischer, Aram Amassian, John B Asbury, Edward H Sargent, “*Colloidal Quantum Dot
Photovoltaics Using Atomic Ligand Passivation*,” *Nature Materials*
(2011)
- [78] Sehoon Kim et al. Conjugated polymer nanoparticles for biomedical in vivo imaging,
Chem Commun, The Royal Society of Chemistry, **46** (2010) 1617

- [79] Djurisi AB, Ng AMC, Chen XY, *ZnO nanostructures for optoelectronics: material properties and device applications*, *Prog Quantum Electron* **34** (2010) 191
- [80] Saito N, Haneda H, Sekiguchi T, Ohashi N, Sakaguchi I and Koumoto K, “*Low-Temperature Fabrication of Light-Emitting Zinc Oxide Micropatterns Using Self-Assembled Monolayers*,” *Advanced Materials* **14** (6) (2002) 418
- [81] Lee CJ, Lee TJ, Lyu SC, Zhang Y, Ruh H, and Lee HJ, *Appl Phys Lett* **81** (2002) 3648
- [82] Yi J, Lee JM, Park W, *Vertically aligned ZnO nanorods and graphene hybrid architectures for high-sensitive flexible gas sensors*, *Sens Actuators B* **155** (2011) 264
- [83] Meron T and Markovich G, “*Ferromagnetism in Colloidal Mn²⁺-Doped ZnO Nanocrystals*,” *J Phys Chem B* **109** (43) (2005) 20232
- [84] Pearton SJ et al., *J Electr Mater* **35** (5) (2006)
- [85] Huang MH, Mao S, Feick H, Yan H, Wu Y, Kind H, Weber E, Russo R and Yang P, “*Room-Temperature Ultraviolet Nanowire Nanolasers*,” *Science* **292** (5523) (2001) 1897
- [86] Desurvire E, *Phys Today* **97** (1994) 20
- [87] Dharmendra K Tiwari, Behari J and Prasenjit Sen, *World Appl Sc J* **3** (3) (2008) 417
- [88] Thembela Hillie and Mbhuti Hlophe, *Nanotechnology and the challenge of clean water*, *Nat Nanotech* **2** (2007) 663
- [89] Rogach AL, Eychmuller A, Hickey SG and Kershaw SV, Reviews; Infrared emission, www.small-journal.com, **3** (4) (2007) 536
- [90] Battaglia C, Escarre J, Soderstrom K, Charriere M, Despeisse M, Haug FJ, Ballif C, *Nanomoulding of transparent zinc oxide electrodes for efficient light trapping in solar cells*, *Nat Photonics* **5** (2011) 535
- [91] Roco MC and Bainbridge WS, *Social Implications of Nanoscience and Nanotechnology*, (Springer, Boston) (2001) 1

Chapter 3. Synthesis and Research Techniques

ZnO doped with terbium and ytterbium, respectively, were synthesized via sol-gel method, and their physical properties were investigated using microscopic and spectroscopic techniques to extract structural and luminescence information. A number of non-destructive experimental techniques were used to accomplish this goal, for instance X-ray powder diffractometry, Scanning electron microscopy, Ultraviolet-visible absorption spectroscopy, Photoluminescence Spectroscopy, Raman Spectroscopy, and X-ray photoelectron Spectroscopy. The aim of this chapter is to provide an overview of these research techniques. Detailed information on the synthesis approach used in the study is also presented.

3.1 Introduction

The method of synthesis used in this study is the sol-gel. The sol-gel process is a wet chemical synthesis technique that is used for the preparation of gels, glasses, and ceramic powders. It has been chosen because of its advantages over other synthesis routes among which the potential for achieving very high levels of molecular homogeneity, the possibility to control both the morphology and size of the powders as well as its low processing temperature [1]. The sol-gel approach is discussed in detail in the next subsection.

3.2 Sol-gel process

The sol-gel process is defined as a wet chemical route for the synthesis of colloidal dispersions (sols) of inorganic and organic-inorganic hybrid materials, particularly oxides and oxides-based hybrid at relatively low temperatures. The sols are subsequently converted into viscous gels (sol-gel transition) [2]. At the transition, the solution or sol becomes a rigid, porous mass through destabilization, precipitation, or supersaturation. Sols are dispersions of colloidal particles in a liquid [3] and colloids are solid particles with diameters of 1-100 nm. The sol becomes a gel when it can support stress elastically. A gel is an interconnected, rigid network with pores of submicrometer dimensions and polymeric chains whose average length is greater than a micrometer [4].

The gels are usually dried at room temperature to form powders. In the sol-gel process, grain growth occur at the same time as agglomeration such that it becomes difficult to differentiate between primary particles which consist of small grains or crystallites, and secondary particles which are agglomerates of primary particles [5]. **Figure 3.1** shows the primary particles of about 2 nm in diameter that agglomerate in secondary particles of about 6 nm.

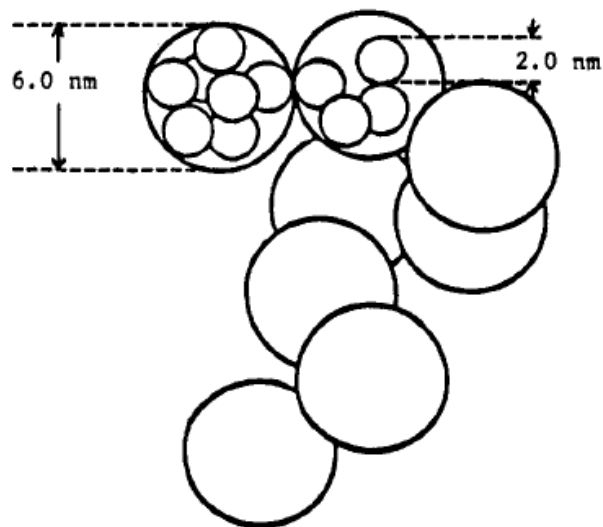
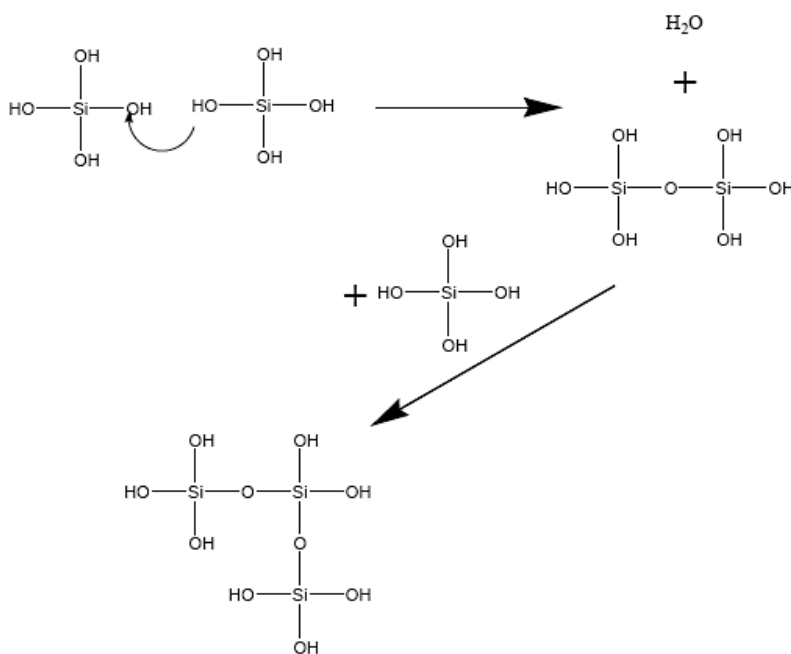


Figure 3.1: Schematic representation of primary and secondary particles in alkoxide gel [3].

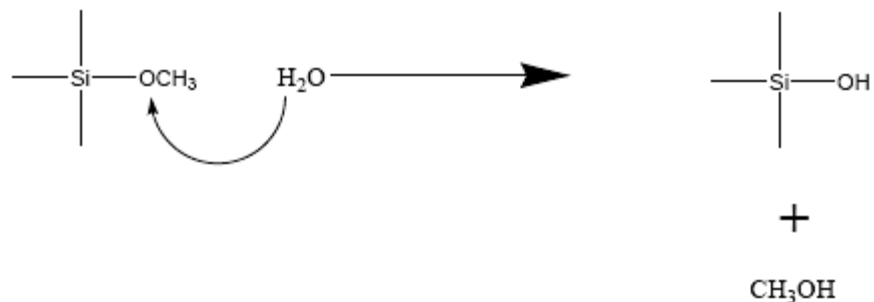
The crystal growth technique in gels has become very important because it is straightforward and can be used at room temperature, in similar conditions to those under which crystal growth naturally [4]. Thus, it enables the incorporation of organic elements into inorganic materials without deterioration of their functionality. The sol-gel processing is particularly useful in making complex metal oxide, temperature sensitive organic-inorganic hybrid materials, and thermodynamically unfavorable or metastable materials [6]. The use of the sol-gel method has attracted great scientific interest in the recent years for making advanced materials and for designing devices with very specific properties [7].

Interest in the sol-gel processing of inorganic ceramic and glass materials began as early as the mid 1800s with Ebelman and Graham studies on silica gels [3]. These early investigators observed that the hydrolysis of tetraethylorthosilicate (TEOS), under acidic conditions yielded SiO_2 in the form of a glass-like material. For a period from the late 1800s through to the 1920s, gels became of considerable interest to chemists stimulated by the phenomenon of Liesegang

Rings formed from gels. In the 1950s and 1960s, the potential for achieving very high levels of chemical homogeneity in colloidal gels was realized to synthesize large number of novel ceramic oxide composition that could not be made using traditional ceramic powder methods. One unique feature of the sol-gel process (reaction 1 and 2, below) is the ability to go all the way from the molecular precursor to the product, thus allowing better control of the whole process (**figure 3.2**) [7].



Reaction 1. Condensation of silanols into a gel. The silanols condense by forming water leading to a network of Si-O-Si bonds. The quaternary functionality of the Si results in a three dimensional network. The silanols groups may be on the surface of nanometer sized silica particles or could be formed by hydrolysis of silicone alkoxides as illustrated in reaction (2).



Reaction 2. Hydrolysis of silicon alkoxides to produce silanols. The silanols subsequently undergo condensation reactions to produce silica gels.

Silicon has four functional groups that can undergo condensation. By altering the reaction conditions (temperature, concentration, pH, solvent and reactant), the degree and nature of the condensation reactions can be controlled. At low pH conditions the rate of condensation slows down with degree of branching resulting in low cross-link density and very porous gels. In contrast high pH will accompany rapid condensation that can produce dense particles that precipitate from the solution. The gels are filled with liquid, generally a water alcohol solution. Controlled drying of the gel is employed to tailor the porosity and composition for specific applications. Highly porous materials can be produced that are exceptional thermal insulators. Alternatively dense gels may be employed as thin film protective coatings for lenses.

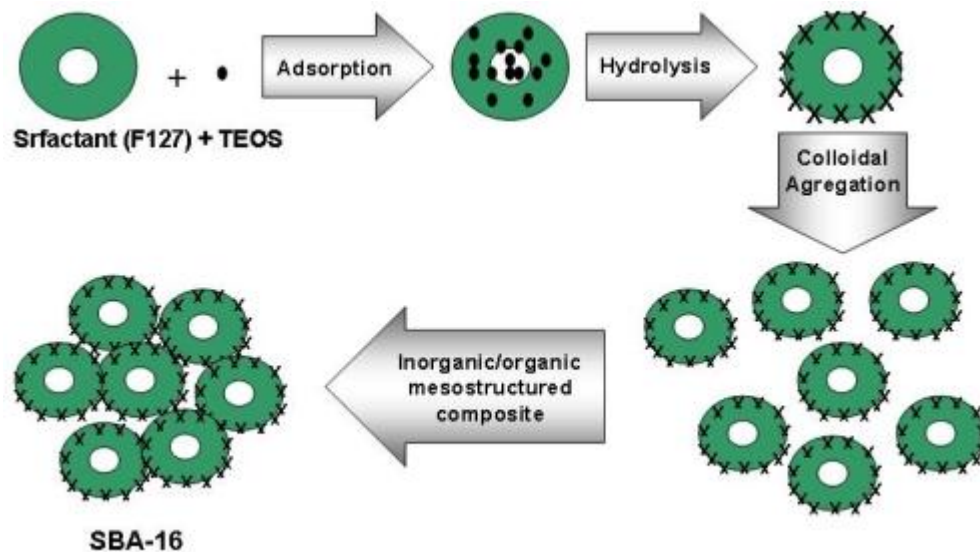


Figure 3.2: Simplified chart of sol-gel process [8].

The particle size can be varied by changing the concentration and aging time. When a gel is maintained in its pore liquid, its structure and properties continue to change long after the gel point and the process is called aging. The process is illustrated in **figure 3.3**. During aging, polycondensation continues along with localized solution and reprecipitation of the network. The strength of the gel is reported to increase with aging.

The liquid is removed from the interconnected pore network during drying. Large capillary stresses can develop during drying when pores are small (<20 nm) and these stresses will cause the gels to crack catastrophically unless the drying process is controlled [3]. Wet-aged increased coalescence and cause little shrinkage on drying. Structural evolution during sol to gel and gel to solid transitions needs to be fully understood to achieve real mastery of the sol-gel process [7]. The properties of a gel and its response to heat treatment are very sensitive to the structure already formed during the sol stage [7].

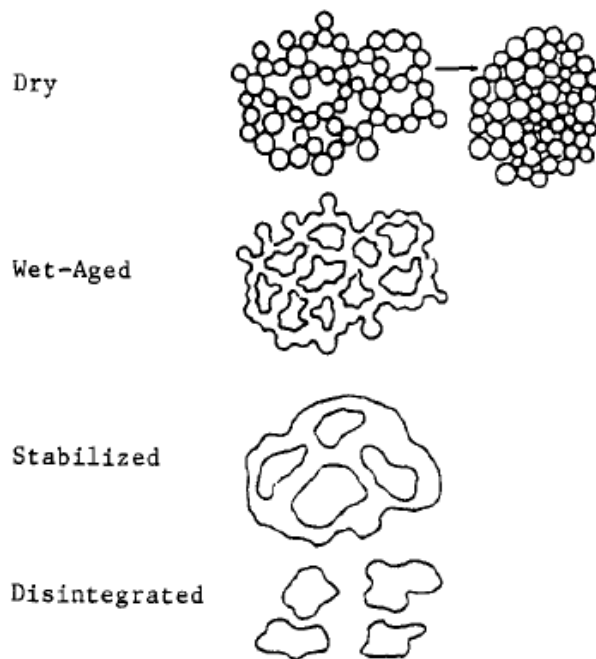


Figure 3.3: Illustration of the stages in aging process of gel [3].

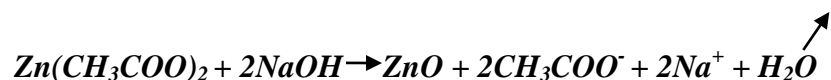
the structure of a gel is established at the time of gelation. Many species are present in the solution, and furthermore, hydrolysis and polycondensation occur simultaneously. The variables of major importance are temperature, nature and concentration of electrolyte (acid, base), nature of the solvent, and type of alkoxide precursor. Yoldas [9] concluded that the hydrolysis reaction and the condensation reaction are not separated in time but take place simultaneously. The sol becomes a gel when it can support a stress elastically [1].

3.3 Preparation of ZnO and ZnO:RE³⁺ (RE = Tb, Yb) nanophosphor

Undoped ZnO

The preparation of colloidal solutions of ZnO nanoparticles in alcohols has been investigated in the past two decades [10].

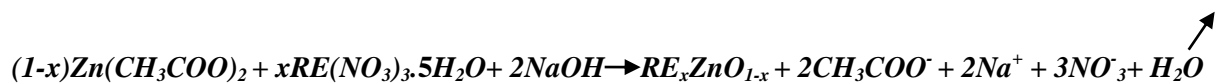
In this study, ZnO nanoparticles were prepared by dissolving 1g of zinc acetate [Zn(CH₃COO)₂·2H₂O] in 65 mL of ethanol (EtOH) by vigorous stirring at 80 °C for 1 hour. The resulting transparent solution was cooled in ice water. A 0.3647 g of NaOH was dissolved in 22 ml of EtOH in an ultrasonic bath and was also cooled in ice water. The NaOH solution was then added drop-wisely to the transparent solution using vigorous stirring in ice water. Oxides are formed during hydrolysis and condensation of the dissolved species according to the following overall reaction:



RE doped ZnO

ZnO:RE³⁺ nanoparticle phosphor was prepared by dissolving firstly 1 g of zinc acetate [Zn(CH₃COO)₂·2H₂O] in 65 ml of absolute ethanol (EtOH) using vigorous stirring at 75-80 °C for 1 hour. Then 0.365 g NaOH was dissolved in 22 ml of EtOH in an ultrasonic bath and was also cooled in ice water while the desired amount of RE (x = 0.1 mol%, 0.5 mol%, 0.75 mol%, 1 mol%) was dissolved in 5 ml of absolute ethanol. Both solutions were drop wisely added to the highly transparent Zn²⁺- solution using vigorous stirring in ice water. The unwanted CH₃COO⁻ and Na⁺ ions were removed by washing the precipitate repeatedly in a mixture of absolute

ethanol and heptane (volume ratio 1:2). The resulting ZnO:RE³⁺ precipitate was either re-dispersed in ethanol or dried in an oven at 200 °C, for 2 hours. The equation below present the reaction taking place during preparation of ZnO:RE³⁺ nanoparticles, where x is the concentration of the RE³⁺.



A flow diagram for the preparation of ZnO:RE³⁺ nanoparticles is shown in **figure 3.4**.

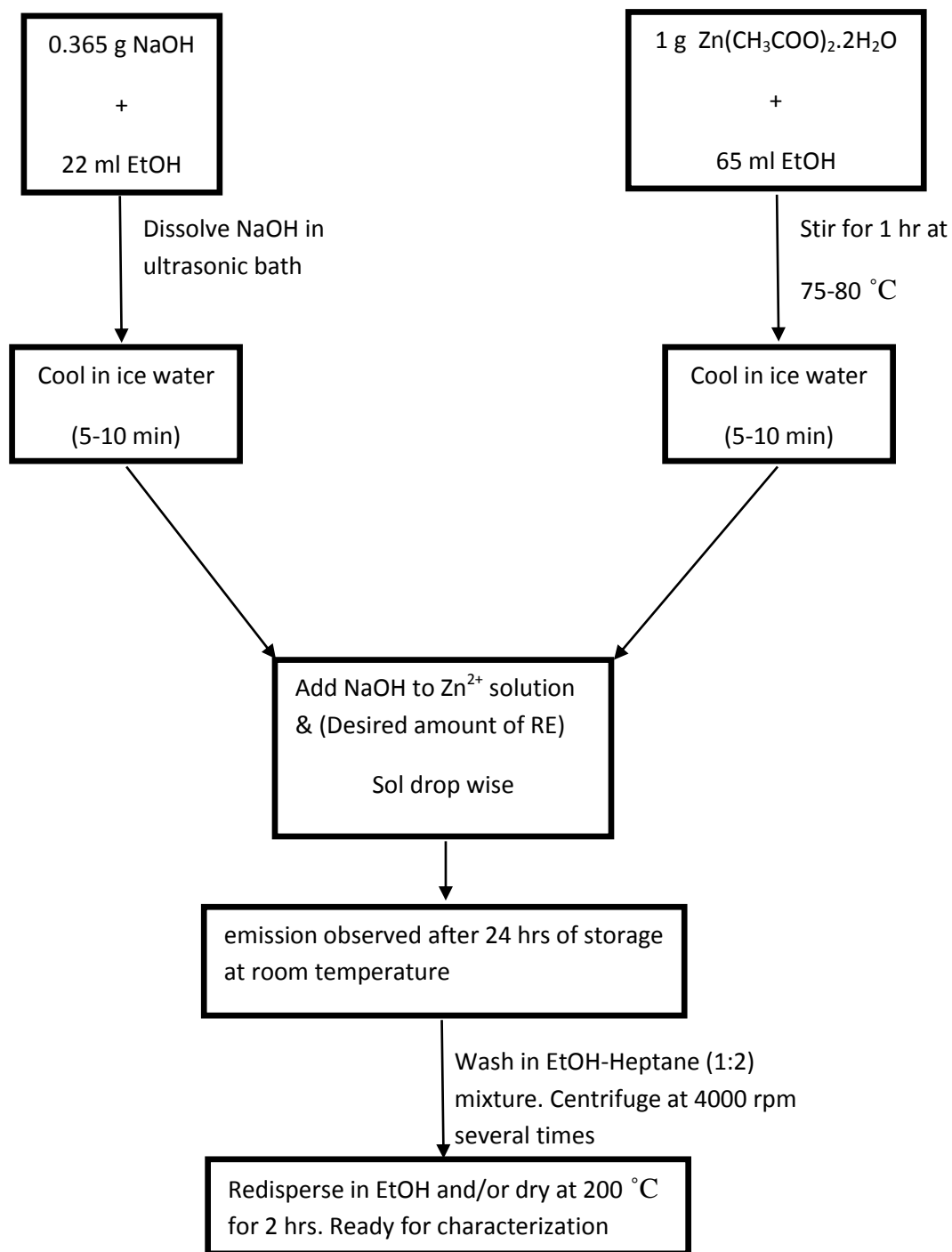


Figure 3.4: A flow diagram of the sol-gel preparation of ZnO:RE³⁺ nanoparticles.

3.4 Characterization techniques

For understanding the relationship between material processing and phosphor performance, our samples were characterized independently. Samples were investigated for their optical, structural, morphology, chemical composition and surface properties. For this purpose we have used different measuring instruments like UV-Vis Spectrophotometer, PL Spectroscopy, CL spectroscopy, Auger Electron Spectroscopy, X-ray diffractometer, X-ray photoelectron spectroscopy, SEM, EDS and TEM.

3.4.1 Optical characterization

Ultraviolet - Visible (UV-Vis) Spectroscopy

The UV-Vis Spectroscopy is an analytical technique in the modern day laboratory. In this study, this technique was used to characterize the intensity of light passing through a sample in the ultraviolet and visible regions in terms of wavelength expressed in nanometers. It is almost entirely used for quantitative analysis; that is, the estimation of the amount of a compound known to be present in the sample [11].

The processes concerned in absorption spectrometry are absorption and transmission based on the Lambert's Law which states that each layer of equal thickness of an absorbing medium absorbs an equal fraction of the radiant energy that traverses it [11].

If the intensity of the incident radiation is I_0 and that of the transmitted light is I , then the fraction transmitted is:

$$I/I_0 = T$$

The percentage transmission is

$$\%T = I/I_0 \times 100$$

The absorbance:

$$A = \log_{10}(I_0/I)$$
$$\Rightarrow \log_{10}(100/T)$$
$$\Rightarrow \epsilon cL$$

where L expressed in m is the length of the radiation path through the sample, c expressed in molar⁻¹ is the concentration of absorbing molecules in that path, and ϵ expressed in mol⁻¹m² is the molar extinction coefficient. In this study the Lambda 750S UV-VIS spectrophotometer, from the CSIR-NCNSM was used to study the absorption properties of the solution samples. **Figure 3.5** shows the schematic diagram of a double-beam UV-VIS spectrophotometry.

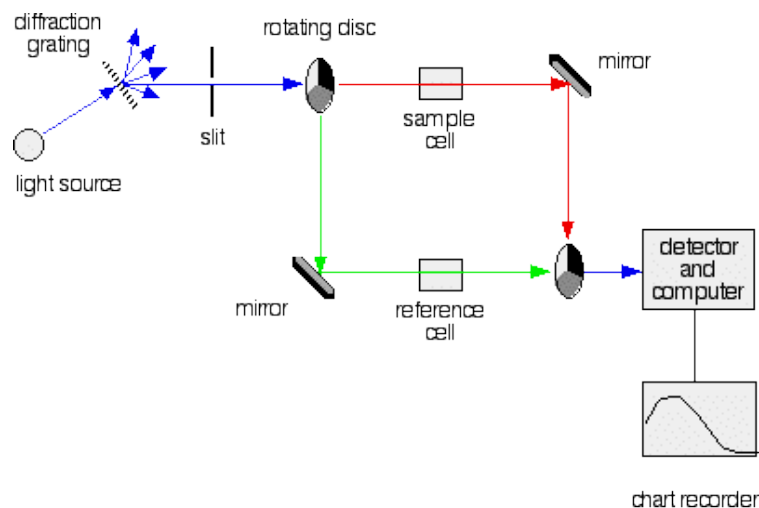


Figure 3.5 : Double-beam UV-Vis absorption spectrophotometer [12].

Photoluminescence (PL) spectroscopy

Photoluminescence spectroscopy is a contactless, nondestructive method of probing the electronic structure of materials. Light is directed onto a sample, where it is absorbed and imparts excess energy into the material in a process called photo-excitation. One way this excess energy can be dissipated by the sample is through the emission of light, or luminescence. In the case of photo-excitation, this luminescence is called photoluminescence [13,14,15].

Photo-excitation causes electrons within a material to move into permissible excited states. When these electrons return to their equilibrium states, the excess energy is released and may include the emission of light (a radiative process) or may not (a nonradiative process). The energy of the emitted light (photoluminescence) relates to the difference in energy levels between the two electron states involved in the transition between the excited state and the equilibrium state. The quantity of the emitted light is related to the relative contribution of the radiative process [15]. In this study, the PL measurements were conducted using a Perkin-Elmer LS-55 Fluorescence Spectrometer, from the CSIR-NCNSM and were confirmed with Fluorolog 3 spectrophotometer available at Unisa laboratory. The **figures 3.6, 3.7 and 3.8** show typical schematic experiment of PL system.

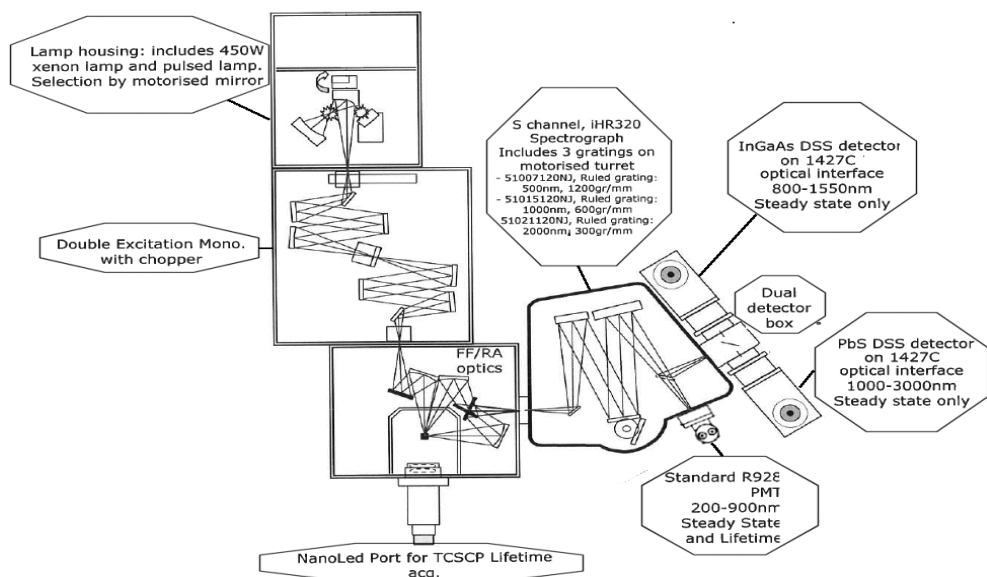


Figure 3.6: System configuration of the PL technique (Fluorolog 3). The sample is irradiated at one wavelength and emission is observed over a range of wavelengths. The excitation monochromator selects the excitation wavelength and emission monochromator selects one wavelength at a time to observe [16].

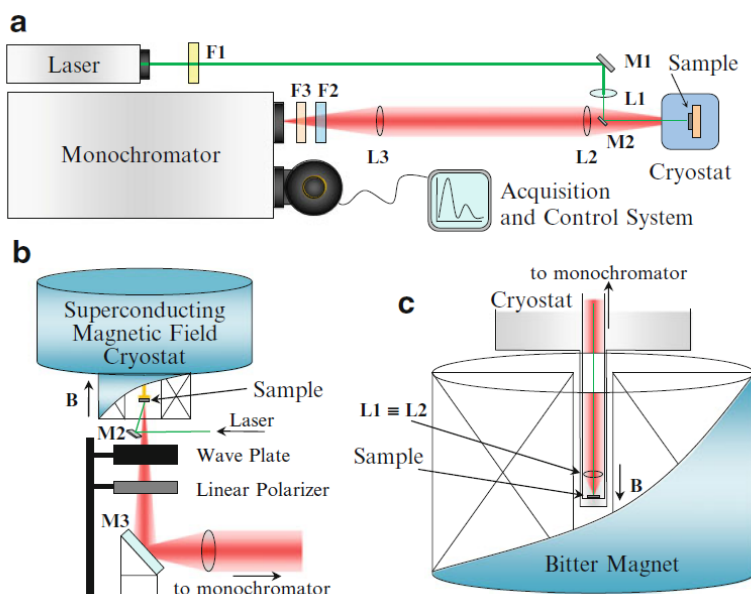


Figure 3.7: (a) Sketch of the experimental setup for PL measurements. Mi label mirrors, Li indicate lenses and Fi filters. (b) Sketch of the cryostat for measurements under low-to-medium (up to -12 T) magnetic fields as obtained by superconducting coils. A linear polarizer and a wave plate are used to resolve the polarization state of the emitted photons. (c) Sketch of the cryostat for measurements under low-to-high (up to -30 T) magnetic fields as obtained in a Bitter magnet by conventional copper disks [17].

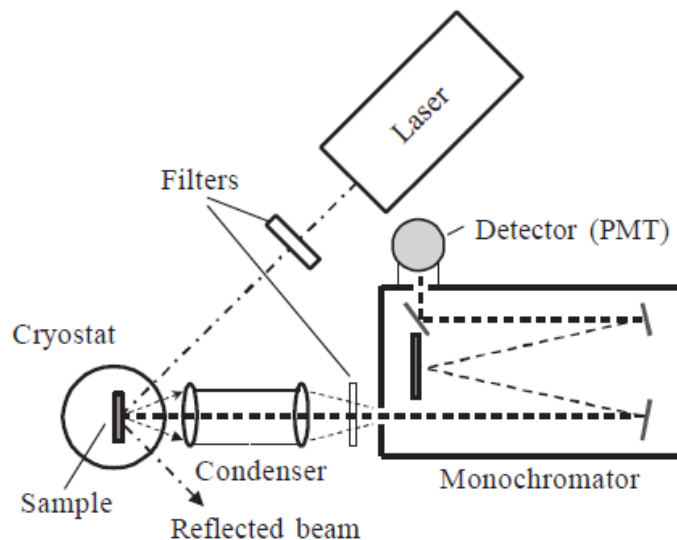


Figure 3.8: Schematic representation of a typical PL setup, including a laser as an excitation source, a grating monochromator as a dispersive element (grating monochromator), PMT as a detector, optical cryostat, filters, and collecting lenses [18].

3.4.2 Structural Characterization

X-ray Diffraction (XRD)

The X-ray diffraction (XRD) technique has been used in this study to characterize the crystalline structure of the powder samples, the XRD also provided information on unit cell dimensions. It is an efficient non-destructive analytical technique used for the identification of crystalline structure of compounds by their diffraction pattern [19].

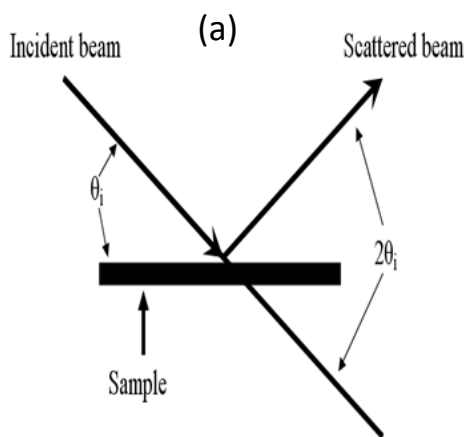
A diffraction pattern is produced when a material is irradiated with a collimated beam of x-rays. The x-ray spectra generated by this technique provide a structural fingerprint of the material (unknown). The relative peak height is generally proportional to the number of grains in a preferred orientation and peak positions are reproducible [19]. The intensity of the diffracted x-rays is measured as a function of diffraction angle 2θ and the specimen's orientation.

Bragg's law was used to explain the interference pattern of X-rays scattered by crystals, diffraction has been developed to study the structure of all states of matter with any beam, e.g., ions, electrons, neutrons, and protons, with a wavelength similar to the distance between the atomic or molecular structures of interest. The process is governed by the equation:

$$n\lambda = 2 d \sin \theta$$

where n is diffraction series, θ is diffraction angle, λ is the wavelength of X-ray, d is interplanar distance. In single crystal, d is the lattice constant.

The x-ray diffractometer used in this study was the X'Pert PRO PANalytical diffractometer with $\text{CuK}\alpha$ at $\lambda = 0.15405 \text{ nm}$ from the CSIR National Centre for Nano-Structured Material (NCNSM). **Figure 3.9** (a) and (b) present the basic principle of the XRD.



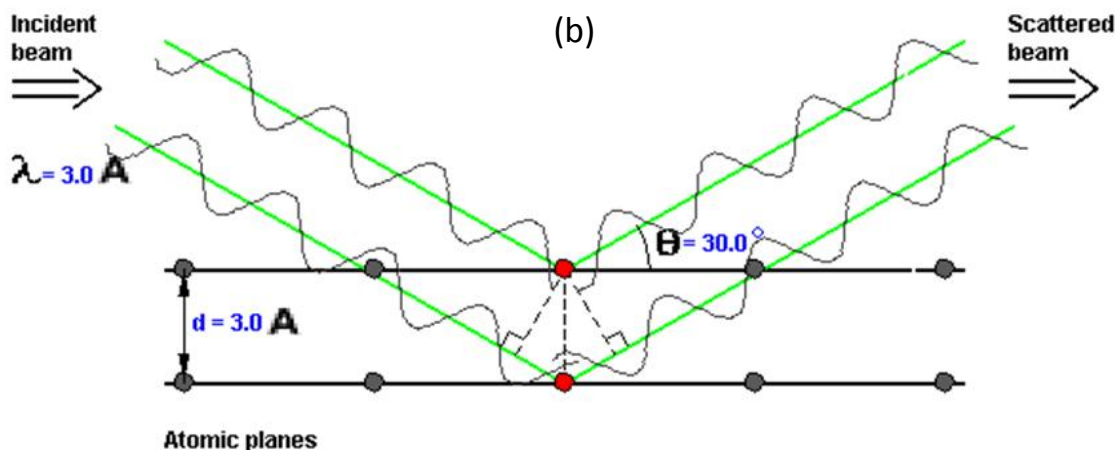


Figure 3.9: (a) and (b) Principle of XRD through the bragg's law [20, 21].

3.4.3 Surface Characterization

X-ray Photoelectron Spectroscopy (XPS)

X-ray photoelectron spectroscopy (XPS), also known as electron spectroscopy for chemical analysis (ESCA), is a widely used surface technique to obtain chemical information at surfaces of different materials. It uses highly focused monochromatised X-rays to probe the material of interest. The XPS process involves the ejection of a photoelectron from the K level of an atom by x-rays in vacuum. The phenomenon is based on the photoelectric effect outlined by Einstein in 1905 where the concept of the photon was used to describe the ejection of electrons from a surface when photons impinge upon it [22]. The energy of the photo-emitted electrons is specific to the chemical state of the elements and compounds present, i.e. bound-state or multivalent states of individual elements can be differentiated [23]. Photoelectrons are collected and analyzed to produce a spectrum of emission intensity versus electron binding energy. The small spot capabilities allow one to obtain XPS information at 30 μm resolutions, making XPS chemical mapping and imaging a viable surface research tool [24]. XPS can easily analyze nonconductive samples with the system charge neutralization. The basic components of the XPS

spectrometer are an x-ray source, electron energy analyzer for the photoelectrons, and an electron detector. In the current study, the PHI 5000 Versaprobe, from the University of the Free State, Department of Physics (Bloemfontein) was used. **Figure 3.10.** shows the photoemission mechanism and **figure 3.11.** depicts the layout of the XPS system.

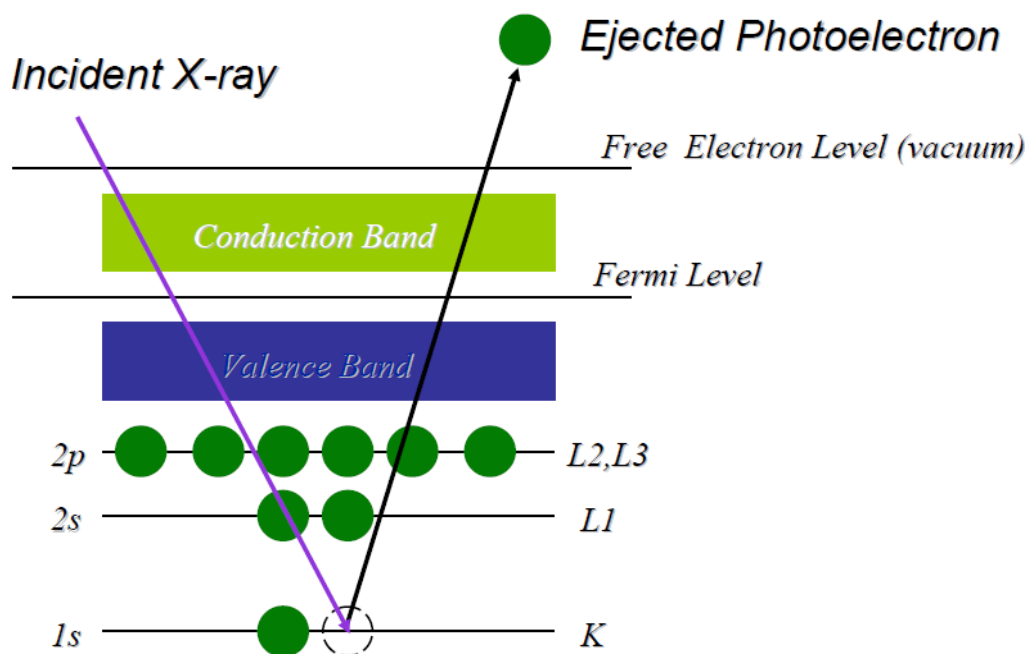


Figure 3.10: Photoemission of electron process [25].

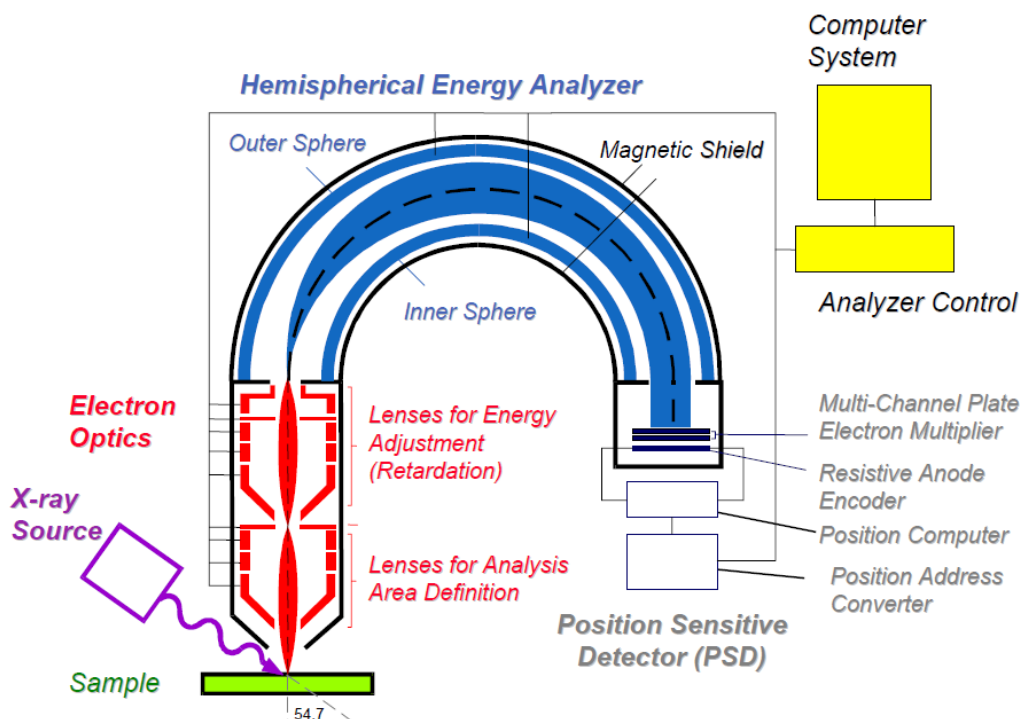


Figure 3.11: Schematic diagram of the XPS system [25].

Raman Spectroscopy

Raman spectroscopy is a non-destructive technique commonly used for optical investigation, in most cases for chemical analysis or in solid state physics. This technique has been fruitfully applied to study interfaces and microstructures in semiconductors [26,27,28]. Raman spectroscopy is based upon the inelastic scattering of monochromatic light within the specimen under investigation, followed by the generation or extinction of elementary excitations [29].

In a typical spectrum, the intensity is plotted against the Raman shift, which is a function of photons population of a certain frequency reaching the detector. Moreover, the Raman shift is given by the frequency difference between the scattered light and the monochromatic excitation source [29].

Most commonly, the Raman shift is designated positive (Stokes Raman scattering) in the case whereby the inelastic light scattering generates an elementary excitation and the scattered light hence exhibiting a lower frequency. The wavenumber value becomes negative (anti-Stokes Raman scattering) in the case of an annihilated elementary excitation [29].

The measurements undertaken in this study were at room temperature, to reduce the thermally excited phonons resulting in an important Stokes process. In the current study, the Horiba Jobin-Yvon HR800 Raman microscope with a 514 nm excitation Ar⁺ laser with a spectral resolution of 0.4 cm⁻¹ from the CSIR-NCNSM. **Figure 3.12.** presents a typical Raman experimental setup.

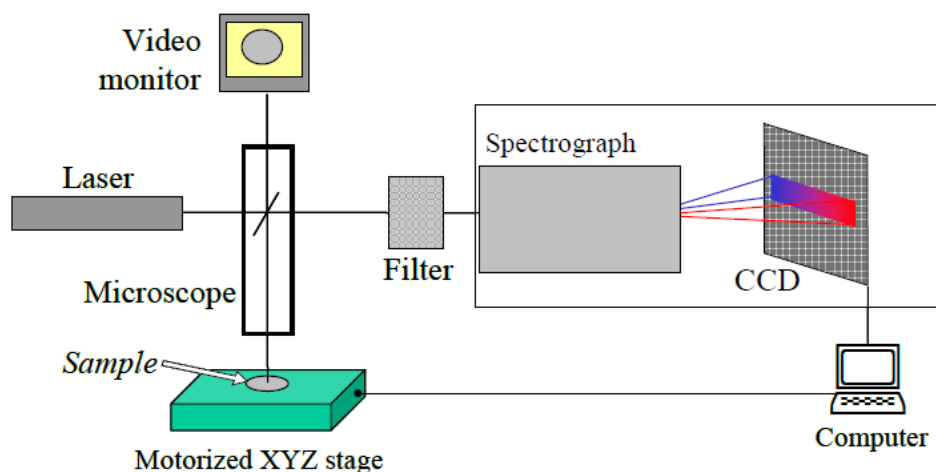


Figure 3.12: Typical Raman experimental setup [30].

Scanning Electron Microscopy (SEM)

Scanning electron microscopy (SEM) is a method for high-resolution imaging of surfaces. The SEM uses electrons for imaging, while a light microscope uses visible light. The advantages of SEM over light microscopy include much higher magnification (>100,000X) and greater depth of field up to 100 times that of light microscopy. Qualitative and quantitative chemical analysis

information is also obtained using an energy dispersive x-ray spectrometer (EDS) with the SEM [14].

The SEM generates a beam of incident electrons in an electron column above the sample chamber. The electrons are produced by a thermal emission source, such as a heated tungsten filament, or by a field emission cathode. The energy of the incident electrons can be as low as 100 eV or as high as 30 keV depending on the evaluation objectives. The electrons are focused into a small beam by a series of electromagnetic lenses in the SEM column [14].

Scanning coils near the end of the column direct and position the focused beam onto the sample surface. The electron beam is scanned in a raster pattern over the surface for imaging. The beam can also be focused at a single point or scanned along a line for x-ray analysis. The beam can be focused to a final probe diameter as small as about 10 Å.

The incident electrons cause electrons to be emitted from the sample due to elastic and inelastic scattering events within the sample's surface and near-surface material. High-energy electrons that are ejected by an elastic collision of an incident electron, typically with a sample atom's nucleus, are referred to as backscattered electrons. The energy of backscattered electrons will be comparable to that of the incident electrons [14].

Emitted lower-energy electrons resulting from inelastic scattering are called secondary electrons. Secondary electrons can be formed by collisions with the nucleus where substantial energy loss occurs or by the ejection of loosely bound electrons from the sample atoms. The energy of secondary electrons is typically 50 eV or less [14].

To create an SEM image, the incident electron beam is scanned in a raster pattern across the sample's surface. The emitted electrons are detected for each position in the scanned area by an electron detector. The intensity of the emitted electron signal is displayed as brightness on a cathode ray tube (CRT). By synchronizing the CRT scan to that of the scan of the incident electron beam, the CRT display represents the morphology of the sample surface area scanned by the beam. Magnification of the CRT image is the ratio of the image display size to the sample area scanned by the electron beam [14].

Two electron detector types are predominantly used for SEM imaging. Scintillator type detectors (Everhart-Thornley) are used for secondary electron imaging. This detector is charged with a positive voltage to attract electrons to the detector for improved signal to noise ratio. Detectors for backscattered electrons can be scintillator types or a solid-state detector [14].

The SEM column and sample chamber are at a moderate vacuum to allow the electrons to travel freely from the electron beam source to the sample and then to the detectors. High-resolution imaging is done with the chamber at higher vacuum, typically from 10^{-5} to 10^{-7} Torr. Imaging of nonconductive, volatile, and vacuum-sensitive samples can be performed at higher pressure [14].

In this study, the SEM images of phosphor powders were obtained from the JEOL JSM-7500F field-emission scanning electron microscope (FE-SEM) equipped with energy dispersive X-ray spectrometer (EDX) from the CSIR-NCNSM. **Figure 3.13** shows the schematic diagram of the SEM [31].

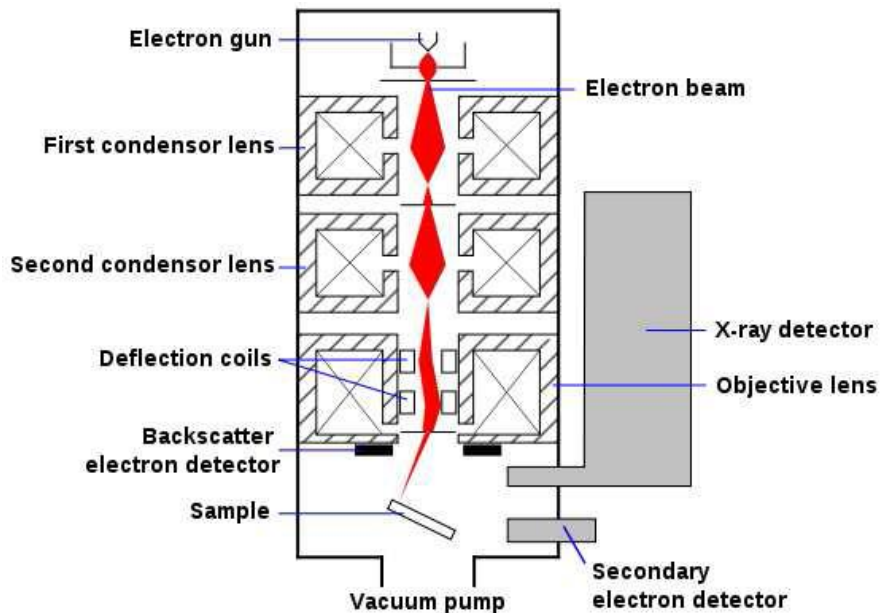


Figure 3.13: Schematic diagram of SEM [32].

Transmission Electron Microscopy (TEM)

TEM is an imaging technique whereby a beam of electrons is transmitted through a specimen, and then an image is formed. The image is then magnified and directed to appear either on a fluorescent screen or layer of photographic film, or to be detected by a sensor such as a CCD camera. The system can study small details in the cell or different materials down to near atomic levels [33, 34]. It can investigate the size, shape and arrangement of the particles which make up the specimen as well as their relationship to each other on the scale of atomic diameters.

Materials to be analyzed with this technique need to have dimensions small enough to be electron transparent and that can be produced by the deposition of a dilute sample containing the specimen onto support grids. The suspension is normally a volatile solvent such as ethanol, ensuring that the solvent rapidly evaporates allowing a sample that can be rapidly analyzed.

The possibility for high magnifications has made the TEM a valuable tool in medical, biological and material sciences research. In all cases, the specimens must be very thin and able to

withstand the high vacuum present inside the instrument. For biological specimens, the maximum specimen thickness is roughly 1 micrometer [34]. To withstand the instrument vacuum, biological specimens are held at liquid nitrogen temperatures. In material science/metallurgy the specimens tend to be naturally resistant to vacuum and must be prepared as a thin foil, or etched so that some portion of the specimen is thin enough for the beam to penetrate.

The system can also be used for the determination of the electron diffraction patterns of the crystalline structures. A crystalline material interacts with the electron beam mostly by diffraction rather than absorption. The intensity of the transmitted beam is affected by the volume and density of the material through which it passes. The intensity of the diffraction depends on the orientation of the planes of atoms in a crystal relative to the electron beam. At certain angles the electron beam is diffracted strongly from the axis of the incoming beam, while at other angles the beam is largely transmitted. In this study the JEOL-Jem 2100 high-resolution transmission electron microscope (HR-TEM) from the CSIR-NCNSM was used to analyze structure and the particle morphology of powder phosphors. **Figure 3.14.** shows the schematic diagram of a TEM.

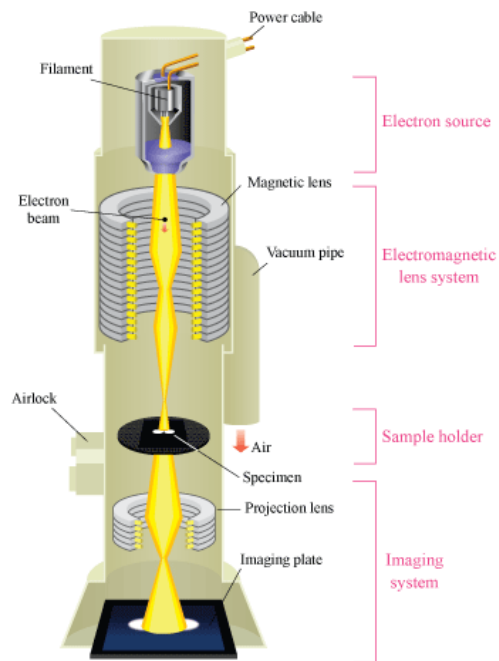


Figure 3.14: Schematic diagram of a TEM [35].

3.5 References

- [1] Hench and West, *The Sol-Gel Process*, *Chem Rev* **90**(1) (1990)
- [2] Klein LC, *Ann Rev Mater Sci* **15** (1985) 227
- [3] Hench LL, West JK, *Chem Rev* **90** (1990) 33
- [4] Aragon-Santamaria P, Santos-Delgado MJ, Maceira-Vidan A, Polo-Diez LM, *J Mater Chem* **1**(3) (1991) 409
- [5] Pierre AC, *Introduction to sol-gel processing*, Kluwer Academic Publishers, Boston, (1998)
- [6] Beecroft LL, Ober CK, *Chem Mater* **9** (6) (1997) 1312
- [7] Criston S, Armelao L, Tondello E, Traldi P, *J Mass Spectrom* **34** (1999) 1380
- [8] http://www.mdpi.com/journal/ijms/special_issues/sol-gel-technique-ijms,
[Accessed, 05 October 2012]
- [9] Yoldas BE, *J Non-Cryst Solids* **63** (1984) 145
- [10] Van Dijken A, Makkinje J, Meijerink A, *J Lumin* **92** (2001) 323
- [11] *Basic UV-Vis Theory, Concepts and Applications*,
<http://www.plant.uoguelph.ca/research/homepages/raizada/Equipment/RaizadaWeb%20Equipment%20PDFs/5B.%20UV%20VIS%20theory%20ThermoSpectric.pdf>.
[Accessed, 28 February 2013]
- [12] *A double beam uv-visible absorption spectrometer*,
<http://www.chemguide.co.uk/analysis/uvvisible/spectrometer.html>,
[Accessed, 20 October 2012]
- [13] Garcia Sole J, Bausa LE and Jaque D, *An Introduction to the Optical Spectroscopy of Inorganic Solids*, John Wiley & Sons Ltd (2005)
- [14] *Handbook of Analytical Methods for Materials*,
http://www.cientificosaficionados.com/microscopio/MICROSCOPIO%20ELECTRONICO_archivos/hamm72d.pdf , [Accessed, 27 October 2012]
- [15] Peter Y. Yu and Manuel Cardona, *Fundamentals of Semiconductors: Physics and Materials Properties*, Springer Heidelberg Dordrecht London New York, (2010)
- [16] Fluorolog-3 Manual, Horiba Jobin Yvon.
- [17] Pettinari G, Polimeni A, and Capizzi M, *Photoluminescence: A Tool for Investigating Optical, Electronic, and Structural Properties of Semiconductors*, Patane A and Balkan N

- (eds.), *Semiconductor Research*, Springer Series in Materials Science 150, DOI10.1007/978-3-642-23351-7 5, Springer-Verlag Berlin Heidelberg (2012)
- [18] *Zinc Oxide: Fundamentals, Materials and Device Technology*. Edited by Hadis Morkoç and Ümit Özgür Copyright (2009) WILEY-VCH Verlag GmbH & Co. KGaA, Weinheim, ISBN: 978-3-527-40813-9
- [19] Cao G, *Nanostructures and Nanomaterials: Synthesis, Properties & Applications*, 6th edition, London, (2004)
- [20] *Bragg's Law and diffraction*, [online]. Available from <http://www.eserc.stonybrook.edu/ProjectJava/Bragg/>, [Accessed, 25 October 2012].
- [21] Introduction to X-ray Diffraction <http://www.eserc.stonybrook.edu/ProjectJava/Bragg/>, [Accessed, 15 October 2013]
- [22] UK Surface Analysis Forum: XPS: <http://www.uksaf.org/tech/xps.html> [Accessed, 5 October 2013]
- [23] *X-ray photoelectron Spectroscopy*: http://www.chem.qmul.ac.uk/surfaces/scc/scat5_3.htm., [Accessed, 5 October 2013]
- [24] Dunn P, Schulze R, Paffett M, *Materials Science and Technology Division Facility Focus*: <http://www.lanl.gov/orgs/mst/files/facilities/LALP-07-018.pdf>., [Accessed, 5 October 2013]
- [25] Introduction to X-ray Photoelectron Spectroscopy (XPS), <http://pire-ecci.ucsb.edu/pire-ecci-old/summerschool/papers/vohs1.pdf>, [Accessed, 15 October 2013]
- [26] Cardona et al., *Light scattering in solids I-X (Topics in Applied Physics)*, edited by Cardona M et al., Springer, Berlin (1983-2007)
- [27] Esser N and Geurts J, in *Optical Characterization of Epitaxial Semiconductor Layers*, edited by Bauer G and Richter W, Springer, Berlin, (1996) 129
- [28] Geurts J, *Prog Crys Grow and Charact* **32** (1996) 185
- [29] Schumm M, *ZnO-based semiconductors studied by Raman spectroscopy: semimagnetic alloying, doping, and nanostructures*, 2008, [PhD Thesis], Julius–Maximilians–Universität Würzburg, Germany
- [30] Gwenaél Gouadec and Philippe Colomban, *Raman Spectroscopy of nanomaterials: How spectra relate to disorder, particle size and mechanical properties*, *Progress in crystal*

growth and characterization of materials **53**(1) (2007) 1

- [31] Mhlongo GH, Luminescence investigation of trivalent rare earth ions in sol-gel derived SiO₂ sand ZnO co-doped SiO₂:Pr³⁺, 2011, [PhD thesis], University of the Free State
- [32] Sri D Suneel, Industrial Production Engineering: special nano materials, characterization and tools
- [33] Wang ZL, Liu Y, Zhang Z, *Handbook of nanophase and nanostructured materials*, 4th edition, New York, (2003)
- [34] Transmission Electron Microscopy:
http://en.wikipedia.org/wiki/Transmission_Electron_Microscopy,
[Accessed, 29 October 2012]
- [35] Basic principle of Transmission Electron Microscope,
http://www.hk-phy.org/atomic_world/tem/tem02_e.html , [Accessed, 29 October 2012]

Chapter 4. Properties of Terbium ions in ZnO Nanocrystals

The current chapter discusses the structural properties, surface morphology and optical properties of as obtained terbium doped ZnO nanocrystals via sol-gel synthesis. Elemental mapping conducted on the as prepared samples using Field-emission Scanning electron microscope (FE-SEM) equipped with an energy dispersive X-ray spectrometer (EDX) revealed homogeneous distribution of Zn, O, and Tb ions. The high resolution transmission electron microscope (HR-TEM) analyses indicated that the un-doped and Tb³⁺ doped samples were composed of homogeneously dispersed particles of high crystallinity with an average size ranging from 4 to 7 nm in diameter, which was in agreement with X-ray diffraction (XRD) analyses. Raman spectroscopy was used to further elucidate the wurtzitic structure of the prepared samples. Finally, UV-Vis and PL results are also discussed.

4.1 Introduction

During the past three decades, ZnO nanostructures have been the subject of intensive investigation due to its luminescent properties, both in the Ultraviolet (UV) and Visible spectral region [1,2]. As a wide direct band-gap (3.37 eV) semiconductor with a large exciton binding energy (60 meV) at room temperature, this material has motivated researchers world wide to undertake research on high efficient and high resolution luminescent display devices such as field emission displays (FEDs), Plasma Display Panels (PDPs), Cathod Ray tubes (CRTs) as well as applications in solar cell, biological and chemical sensors [3-5]. The need of tuning the optical and electrical properties of semiconductor quantum dots (QDs) brought scientists to incorporate intentionally various types of impurities into the ZnO lattice structure through rare earth (RE) doping and RE-RE co-doping [6,7]. Rare earth ions are well known for their high color purity emission lines due to their $f-f$ or $f-d$ internal orbital transitions [8-12].

In order to achieve unique properties in semiconductors, the most important well known and established process applied in solid state device fabrication is the incorporation of impurities through doping. However, the incorporation of the desired amount of impurities proved to be a huge and challenging task while working with quantum dots. [13,14].

The present research work reports mainly on the optimization of the concentration of Tb^{3+} ions in ZnO nanocrystals using a sol-gel method as a synthesis procedure. It has been challenging to obtain a final product of high purity without any other phase as a result of doping, but the flexible sol-gel method offers the possibility to monitor the process of doping during the hydrolysis of zinc acetate. The prepared phosphor powder is a potential material for solar cell application and bio-imaging by exploiting mainly the down-conversion of photons. Finally, it is

important to mention that in the past, Tb^{3+} doped ZnO was synthesized through different methods with diverse fortunes [15-20]. The outstanding optical properties of ZnO nanoparticles as well as the behaviour of Tb^{3+} into the ZnO lattice attracted our attention since doping semiconductor nanocrystals is a challenging task [21-24]. In the present study, the dependence of PL intensities of Tb^{3+} doped ZnO nanocrystals on variation of Tb^{3+} concentrations is reported after a successful doping process via a facile co-precipitation method. Detailed study was also conducted on elemental and microstructural analysis where un-doped and Tb^{3+} doped ZnO with different concentrations were compared.

4.2 Experimental

4.2.1 Un-doped and Tb^{3+} doped ZnO nanocrystals preparation

Un-doped and Tb^{3+} doped ZnO nanocrystals with different concentrations of Tb^{3+} were synthesized using co-precipitation method reported elsewhere [25-27] with few modifications (see subsection 3.1.2). The chemicals were purchased from Sigma-Aldrich and used without further purification. ZnO nanoparticles were prepared using zinc acetate ($Zn-(CH_3COO)_2$) and sodium hydroxide (NaOH) as starting materials. In a typical preparation of un-doped ZnO, $Zn(CH_3COO)_2 \cdot 2H_2O$ (5 mmol) was dissolved in a fixed amount of boiling ethanol, and the solution was cooled in an ice bath. NaOH (10 mmol) dissolved in desired amount of ethanol in a pre-heated ultrasonic bath was also cooled in an ice bath. This solution was slowly added to Zn^{2+} solution under vigorous stirring for 30 min. The resulting solution was then kept at room temperature for 24 hours for further nucleation and growth of ZnO nanoparticles. Green emission by an UV excitation was observed from a transparent suspension of ZnO nanoparticles after 24 h of storage at room temperature, indicating the formation of the ZnO nanoparticles. The Tb^{3+}

doped ZnO nanocrystals were synthesized using almost the same procedure. Except that, the appropriate amount of $\text{Tb}(\text{NO}_3)_3 \cdot 5\text{H}_2\text{O}$ (0.15, 0.5 and 1 mol% Tb) was dissolved in a desired amount of ethanol, then added into hydrolyzed Zn^{2+} precursor solution, and finally stored at room temperature for 24 hours. Both un-doped and Tb^{3+} doped ZnO precursor solutions were then centrifuged and repeatedly washed with heptane to remove unreacted Na^+ and CH_3COO^- ions. The obtained white precipitates were then re-dispersed in ethanol or dried at 200°C for 2 hours and were ready for characterization.

4.2.2 Characterization

Structural analysis of un-doped and Tb^{3+} doped ZnO nanocrystals were carried out by X'Pert PRO PANalytical diffractometer with $\text{CuK}\alpha$ at $\lambda = 0.15405$ nm. Morphology and chemical composition of the samples were analyzed using a JEOL JSM-7500F field-emission scanning electron microscope (FE-SEM) equipped with energy dispersive X-ray spectrometer (EDX), and JEOL 2100 high-resolution transmission electron microscope (HR-TEM), respectively. Samples for TEM measurements were prepared by sonicating ZnO powder samples in ethanol for 15 min. A few drops of the resulting suspension were placed on a TEM grid. Optical properties on the other hand were characterized using room temperature UV-Vis absorption (Perkin-Elmer Lambda 750S UV-Vis spectrometer) and PL (Perkin-Elmer LS-55 Fluorescence Spectrometer) at an excitation wavelength of 310 nm. Microstructural properties were studied by Horiba Jobin-Yvon HR800 Raman microscope with a 514 nm excitation Ar^+ laser with a spectral resolution of 0.4 cm^{-1} .

4.3 Results and discussion

4.3.1 Surface morphology

As observed in SEM images shown in **Figure 4.1**, both un-doped and Tb^{3+} doped ZnO samples revealed well separated but clustered particles that are spherical in shape. These particles showed clear necking with their neighbours. The particle size of the as-prepared un-doped and Tb^{3+} doped ZnO samples was verified using TEM. As indicated in **Figure 4.2**, the TEM images show homogeneous dispersion of ZnO and ZnO:Tb^{3+} particles with the average particle size ranging from 3 to 6 nm in diameter. The HR-TEM images in the insert in **Figure 4.2** (a) and (b) indicate that both un-doped and Tb^{3+} doped nanoparticles are of high crystallinity, respectively. In addition, these HR-TEM images clearly show the lattice fringes. The lattice spacing estimated from the HR-TEM images was found to be around 0.281 nm (**figure 4.2** (c)) which corresponds to the (0100) planar spacing of ZnO in the hexagonal wurtzite phase.

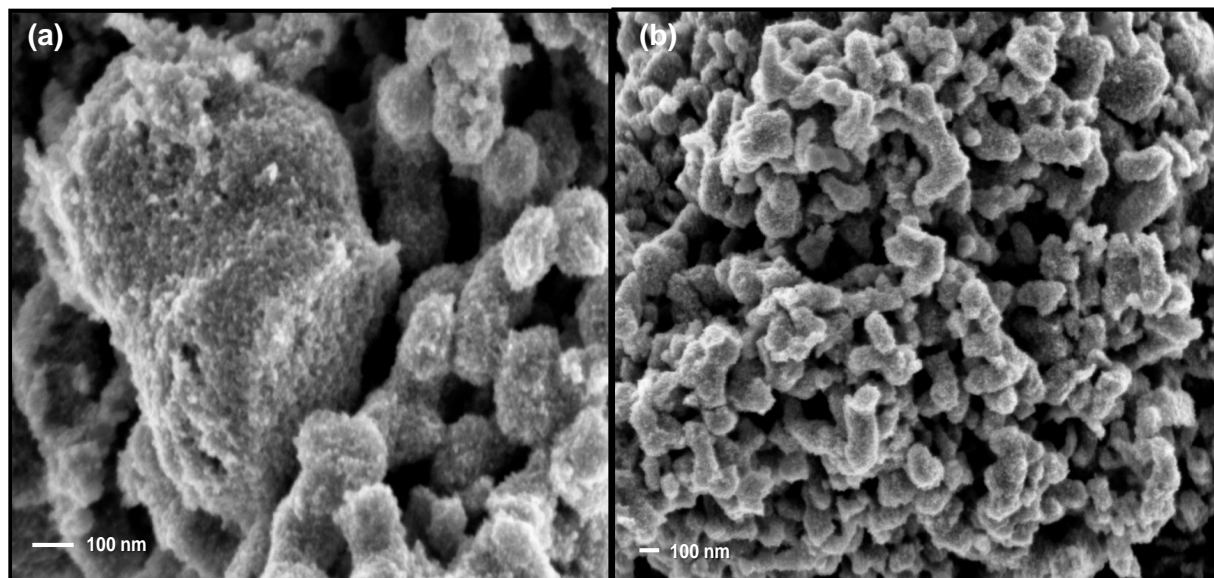


Figure 4.1: FE-SEM image of the as-prepared (a) un-doped ZnO and (b) $\text{ZnO:0.5 mol\% Tb}^{3+}$.

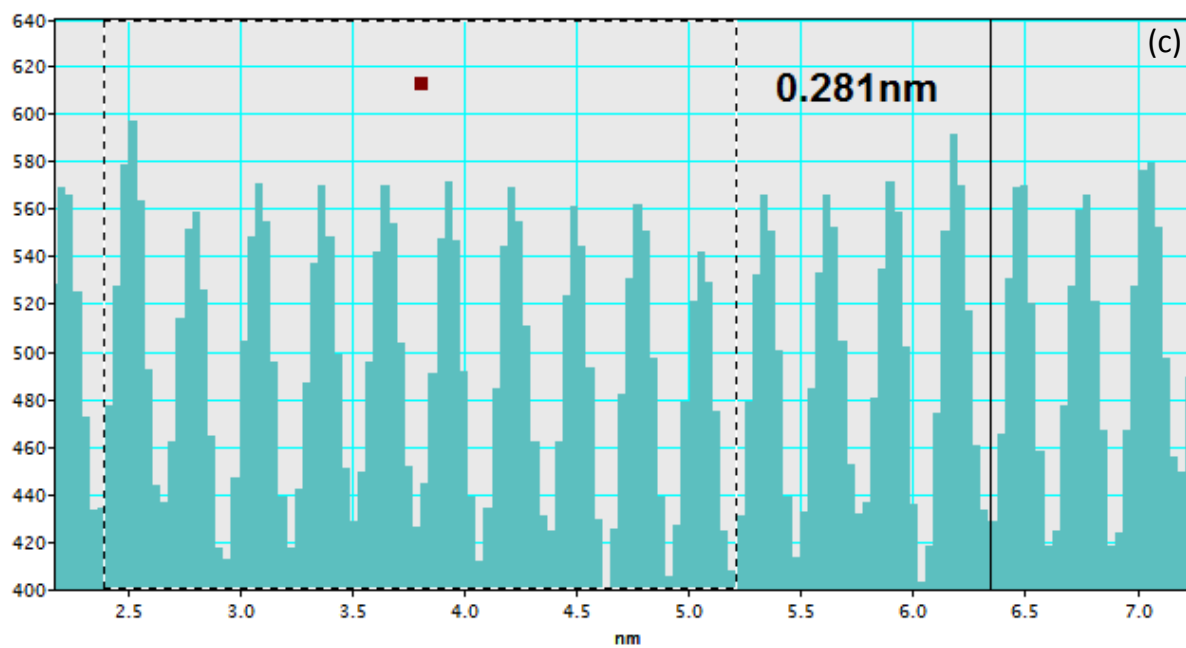
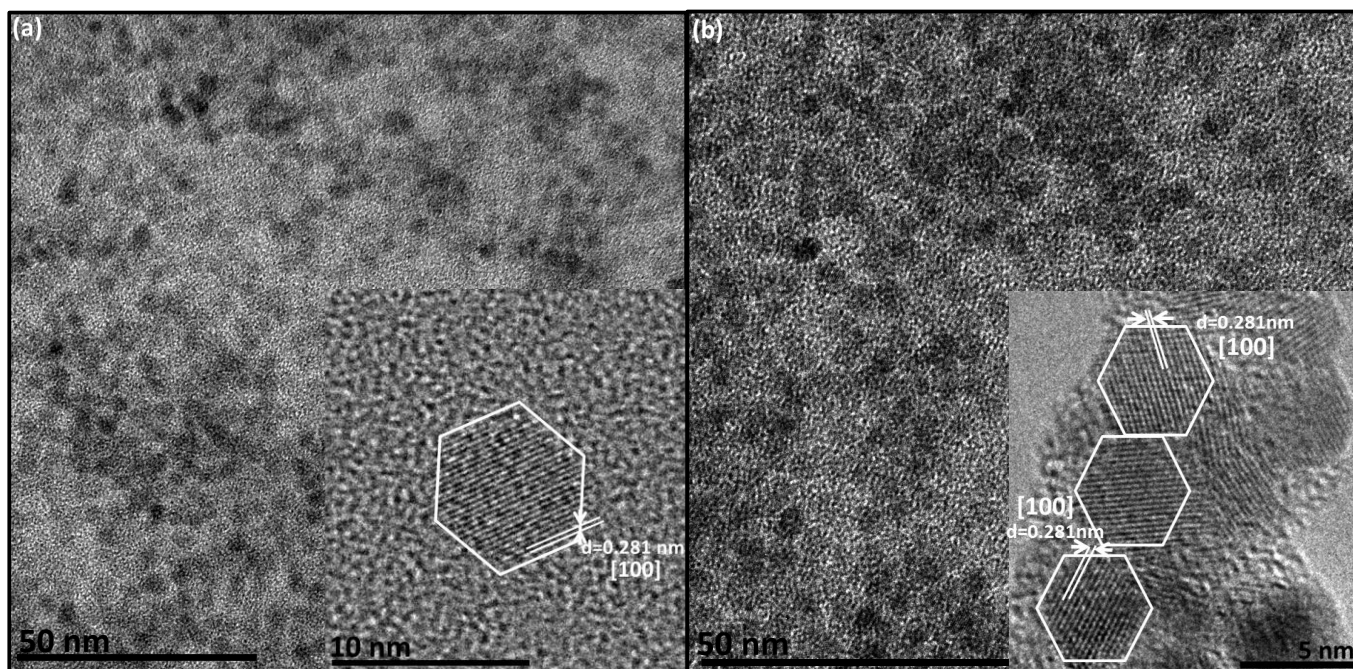


Figure 4.2: HR-TEM images of the as-prepared (a) un-doped and (b) 0.5 mol% Tb^{3+} doped ZnO nanocrystals. (c) HR-TEM profile of the 101 plane for $\text{ZnO}:\text{Tb}^{3+}$.

Elemental analysis of the as-prepared ZnO samples was carried out by the EDX. **Figure 4.3 (a)** and **Figure 4.4 (a)**, both represent un-doped and Tb^{3+} doped ZnO samples respectively. In

both cases, samples did not show any impurities as only expected elements could be detected. Additional peaks of Cu and C are due to the copper grids (which are coated with a carbon film) used during EDX analysis. The inserts in **Figure 4.3** (a) and **Figure 4.4** (a) indicate regions where EDX mapping was conducted for both un-doped ZnO and 0.5 mol% Tb³⁺ doped ZnO respectively. The EDX mappings in **Figure 4.3** (b-d) show homogenous distribution of Zn and O. Similarly in the case of Tb³⁺ doped ZnO sample, the EDX mappings in **Figure 4.4** (b-e) suggest that the distribution of Zn, O, and Tb ions was quite homogeneous. These results agree with the results reported by Li et al. [28].

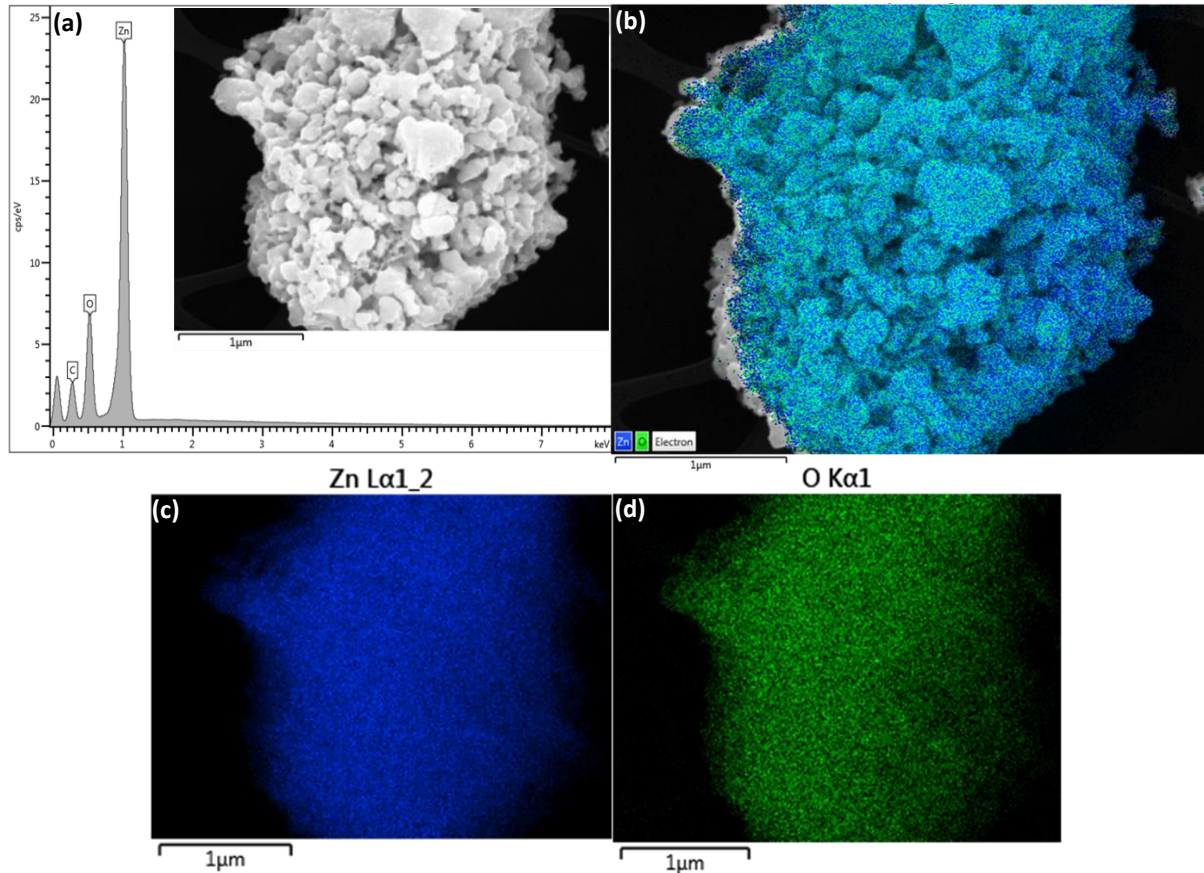


Figure 4.3: (a) EDX spectrum of un-doped ZnO and the insert is the FE-SEM image used for conducting EDX analysis, (b) EDX layered image of un-doped ZnO after elemental mappings of Zn and O, (c-d) Corresponding elemental mappings of Zn and O.

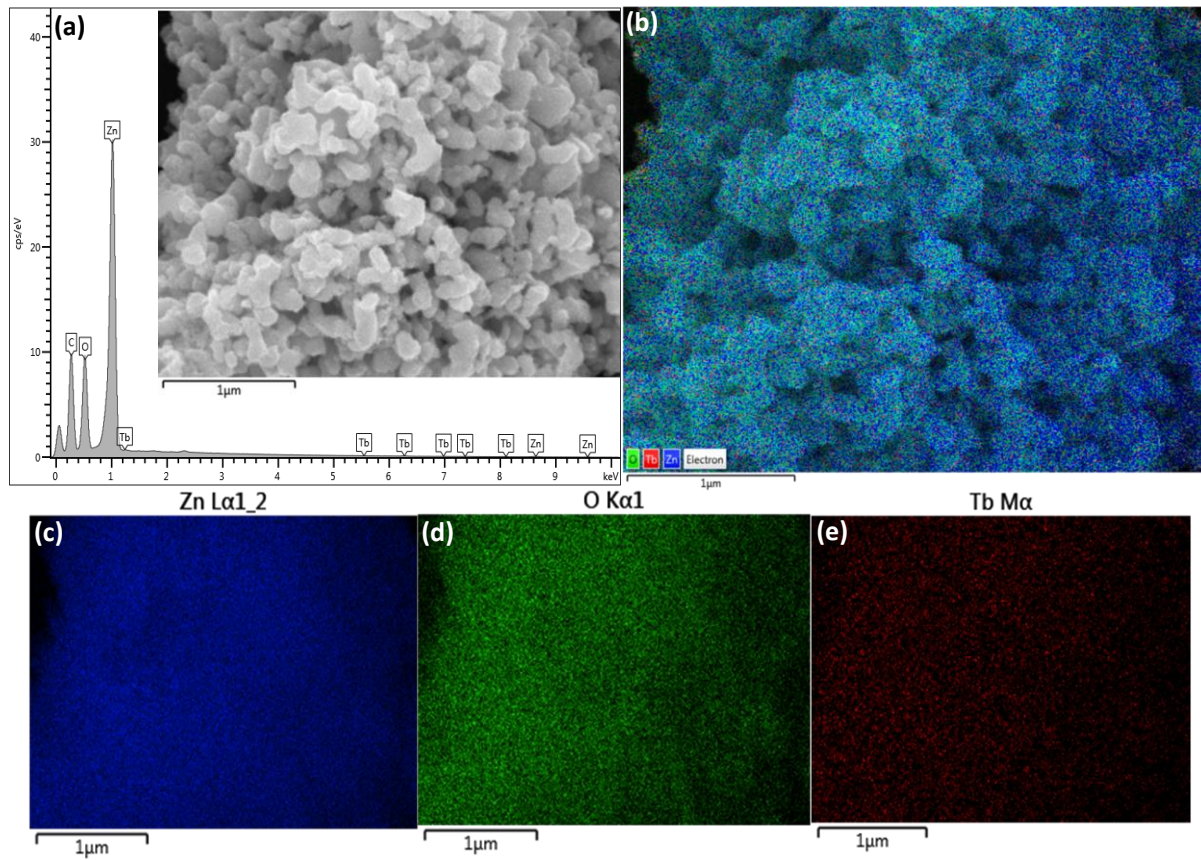


Figure 4.4: (a) EDX spectrum of 0.5 mol% Tb^{3+} doped ZnO and the insert is the FE-SEM image used for conducting EDX analysis, (b) FE-SEM layered image of Tb^{3+} doped ZnO after elemental mappings of Zn, O, and Tb, (c-e) Corresponding elemental mappings of Zn and O.

4.3.2 Structural properties

In order to study structural properties of the as-prepared un-doped and Tb^{3+} doped ZnO nanocrystals, XRD analyses were carried out. **Figure 4.5** shows the XRD patterns of un-doped ZnO and ZnO: Tb^{3+} nanocrystals with different doping concentrations dried at 200 °C. It can be seen that diffraction patterns of both un-doped and Tb^{3+} doped ZnO show only diffraction peaks corresponding to hexagonal wurtzite ZnO (JCPDS card # 36-1451). No diffraction peaks related to Tb_2O_3 could be observed and this indicates that Tb^{3+} ions have entered the ZnO crystal lattice

substituting the Zn^{2+} ions, or entered the oxygen tetrahedral interstitials. Using the strongest diffraction peak (101) at 36.36° , with Scherrer formula [29], the average crystallite sizes (D) was determined to be 5 nm for pure ZnO and 4, 4, and 6 nm for 0.15, 0.5 and 1 mol % of Tb^{3+} into ZnO, respectively. Compared to un-doped ZnO nanocrystals, the main (101) diffraction peak of the Tb^{3+} doped ZnO samples was found to be slightly shifted to lower 2θ angles as a result of dopant incorporation due to larger ionic radius of Tb^{3+} (0.92 Å) than that of Zn^{2+} (0.74 Å) [30]. This is similar to the substitution of Zn^{2+} position by other dopants [31]. The magnified region of (101) peak is shown in the insert in **Figure 4.5**. According to Mohanty et al. [32] this peak shifting and broadening of the (101) diffraction peak with increasing dopant concentration can be ascribed to lattice mismatch, distortion and crystal strain. In addition, these XRD results confirm Tb^{3+} doping in ZnO nanocrystals. In order to confirm the substitution of Zn^{2+} by Tb^{3+} ions in the lattice structure, the angle shift of 2θ ($\delta(2\theta)$) of the most intense peak of ZnO (101) reflection as a function of doping concentration of Tb (x mol%) was calculated and the plot is illustrated in **Figure 4.6** (a). It was noted that 2θ remains unchanged as the x mol% was increased from 0 to 0.15 mol% after which an increase of $\delta(2\theta)$ up to 0.1° was noted as the x mol% rises from 0.15 to 1 mol%. It is also interesting to note that the smaller is FWHM the larger D becomes, this result indicate better crystallization of the particles up to 1 mol% terbium doping (see **Figure 4.6** (b)). The d_{hkl} lattice spacing, the strain induced in powders (ϵ), the dislocation density ($\delta(D)$) which represent the amount of defects in the particle were calculated for the most intense (101) diffraction peak and presented in **Table 4.1** where all computed XRD results are summarized.

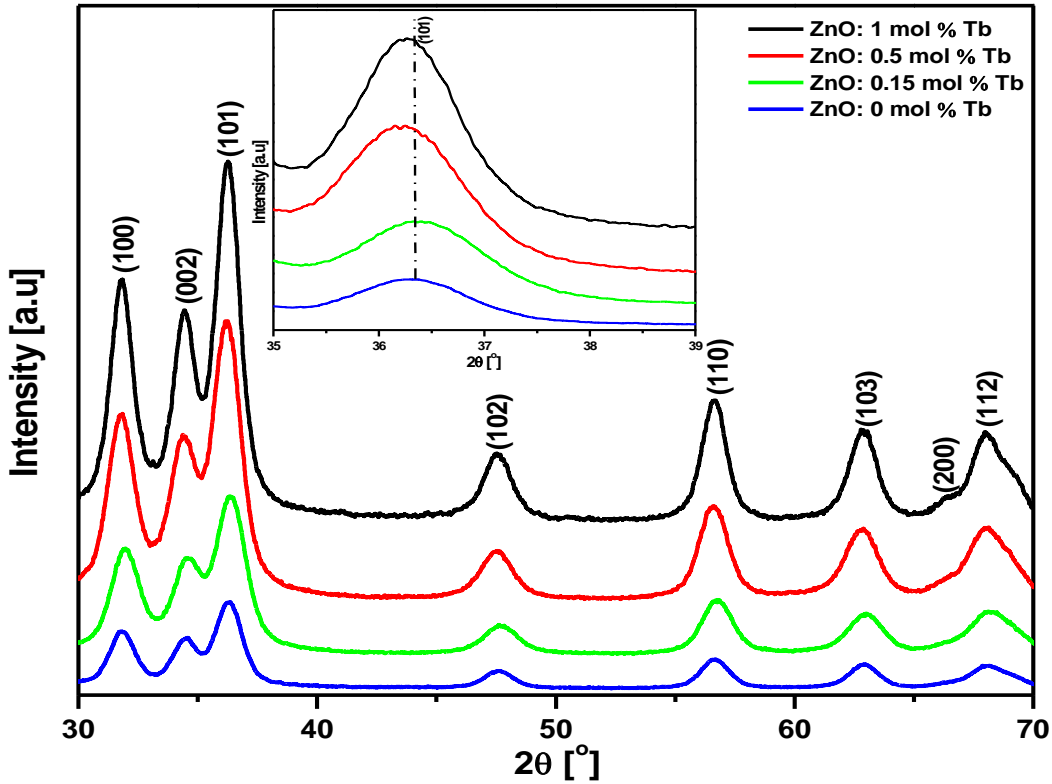


Figure 4.5: XRD patterns of un-doped and ZnO: Tb³⁺ nanocrystals at different doping concentrations dried at 200 °C. The insert is the magnified region of (101) peak.

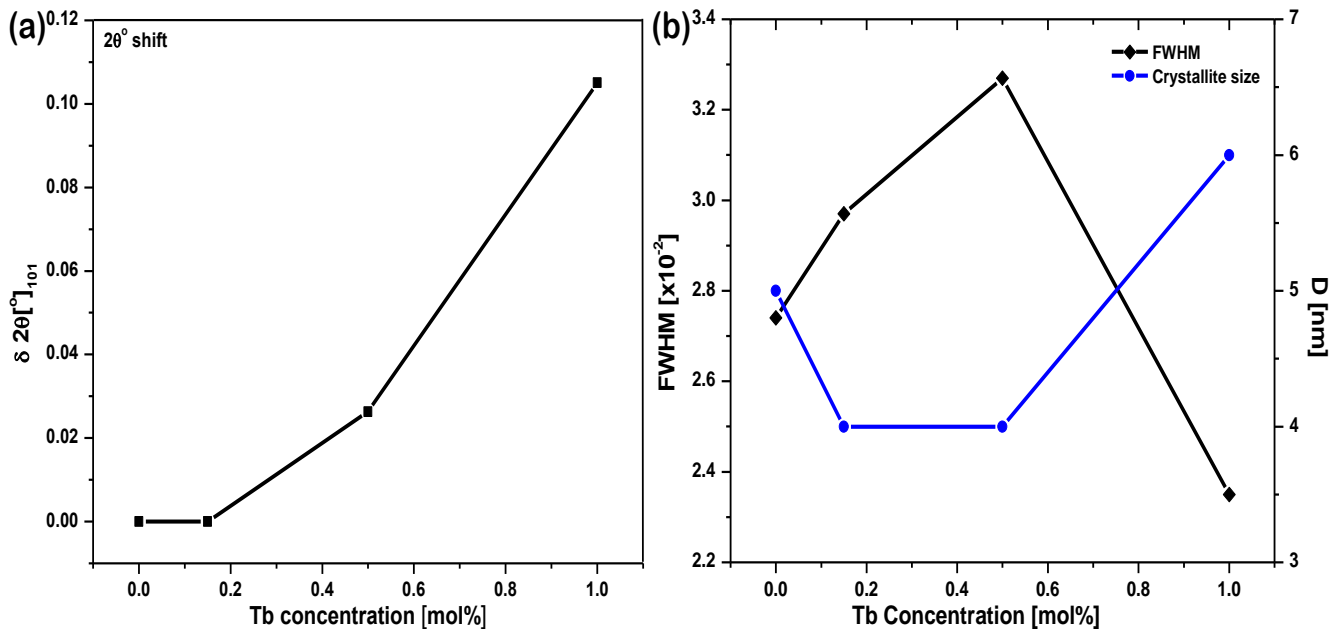


Figure 4.6: (a) Peak shift for (101) plane, and (b) Full Width at Half Maximum (FWHM) and crystallite size as a function of Tb concentration.

Table 4.1 Structural parameters of un-doped and Tb -doped ZnO.

X [mol% Tb]	d_{101} [nm]	β [FWHM]	D [nm]	ε	δ [nm ⁻²]
0	0.2467	0.0274	5	0.0208	0.04
0.15	0.2477	0.0297	4	0.0226	0.06
0.5	0.2471	0.0327	4	0.0249	0.06
1	0.2475	0.0235	6	0.0179	0.03

For further elucidation on the microstructures, Raman measurements were conducted. Raman spectra are sensitive to crystallization, structural disorder and defects in micro and nanostructures. ZnO has a wurtzite structure and belongs to the C_{6v}^4 space group or $P6_3mc$ symmetry group, with two formula units per primitive cell where all of the atoms are occupying the C_{3v} sites [32-34]. The different symmetries involved govern where their vibrations are Raman active and appear in the spectra, while changes in lattice spacing and chemical environment may shift the vibrational frequencies. According to group theory predictions, the single crystalline ZnO has eight sets of optical phonons near the centre of the Brillouin zone, and hence is classified as $\Gamma = A_1 + 2B_1 + E_1 + 2E_2$ [35]. Amongst these, the A_1 and E_1 modes are both Raman and infra-red active. Moreover, these A_1 and E_1 are polar and split into two transverse optical (TO) and longitudinal optical (LO) phonons. E_2 modes are Raman active only while the B_1 modes are silent [36]. **Figure 4.7** presents micro-Raman spectra of un-doped and Tb^{3+} doped ZnO nanocrystals with the 514 nm line of the Ar^+ laser line as the excitation source at room temperature. As shown in the Raman scattering spectra in **Figure 4.7**, four Raman modes were observed at 325, 437, 581, and 672 cm^{-1} . The sharp and intense Raman peak at 437 cm^{-1} can be assigned to the ZnO non-polar optical phonon E_2 (high) mode while a very small phonon peak around 325 cm^{-1} can be attributed to E_2 (high)- E_2 (low) symmetry mode probably marking multi-phonon scattering. The phonon peak at 437 cm^{-1} confirms that the products

formed are wurtzite hexagonal ZnO structure which is consistent with previous reports [37-40]. The phonon peak centred at 581 cm^{-1} is presumably E_1 symmetry with LO mode ($E_1(\text{LO})$), while the one centred at 672 cm^{-1} correspond to TA+LO mode. The 581 cm^{-1} Raman peak, was attributed to defects such as oxygen vacancies (V_{O}), zinc interstitials (Zn_i) and/or free carriers in several reports [40,41]. In this study, the Raman peak at 581 cm^{-1} is also caused by the presence of defects such as V_{O} in un-doped and Tb^{3+} doped ZnO nanocrystals. Furthermore, an obvious increase in Raman intensities with increasing dopant concentration was also observed. This indicates an increase in crystallinity of the samples which is consistent with XRD. On the other hand, it is also noticed that as the dopant concentration is increased, the main peak at 437 cm^{-1} shifted toward low wavenumbers denoting an effective substitution of Zn^{2+} ions with Tb^{3+} ions (see insert in **Figure 4.7**). Similar trend was also observed on XRD results. The results agree well with those reported by Du et al. [36] for Eu^{3+} doped ZnO.

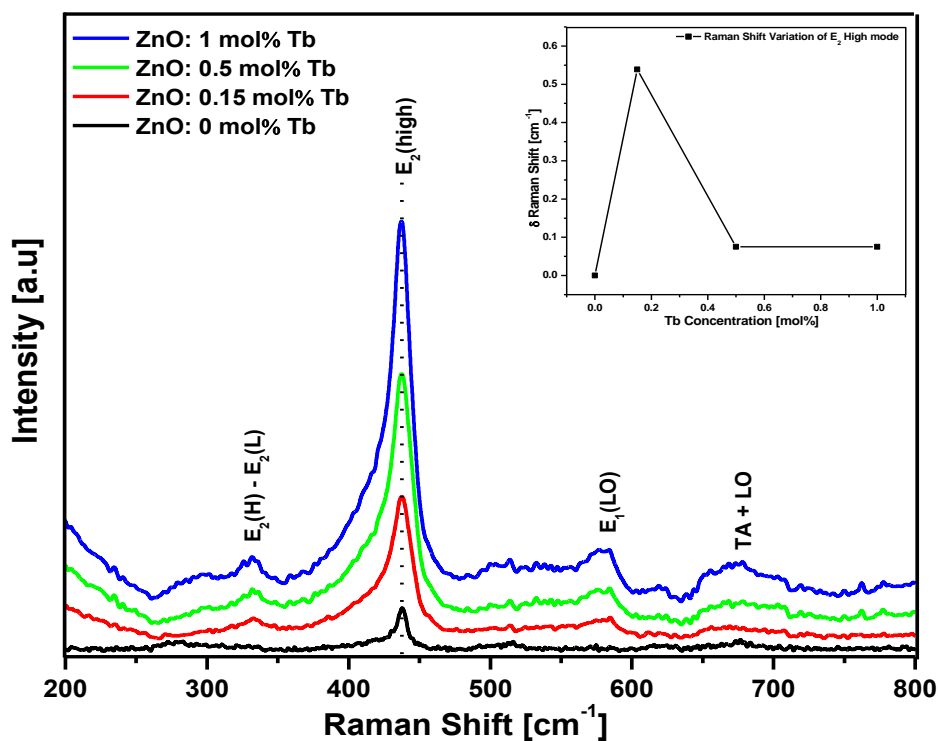


Figure 4.7: Raman spectra of the as-prepared un-doped and Tb^{3+} doped ZnO nanocrystals. The insert shows a comparison of the E_2 phonon shift as a function of Tb^{3+} concentration.

4.3.3 Optical properties

Figure 4.8 compares the UV–Vis absorption spectra of the as-prepared un-doped and Tb^{3+} doped ZnO samples. The absorption spectra showed well-defined exciton bands at 365 for un-doped ZnO and 312, 360, 368 for, 0.15, 0.5, and 1 mol% Tb^{3+} doped ZnO samples, respectively. It worth mentioning that both absorption peaks for un-doped and Tb^{3+} doped have shown blue shift relative to the bulk exciton absorption (386 nm) [42,43]. The blue-shift observed may be attributed to quantum confinement effect [44]. Moreover, a shift of the absorption edges with increasing Tb^{3+} concentration was observed for Tb^{3+} doped samples compared to un-doped ZnO. Similar observation has been reported elsewhere [12,45]. On the other hand, optical absorption spectra of the Tb^{3+} revealed higher absorption with increasing Tb^{3+} concentration. The blue-shifting of the absorption edge with increasing dopant concentration may be either due to the (i) particle size reduction in the Tb^{3+} doped samples with increasing doping concentration, (ii) variation in carrier concentrations and carrier scattering by micro-structural defects, grain boundaries, and ionic impurities, and (iii) lattice distortion due to incorporation of larger Tb^{3+} ions in ZnO lattice. The widening of the band-gap in this case can be associated with the ‘Burstein-Moss effect’ [46] which takes place when electron carrier concentrations exceed the density of states for the conduction band-edge, a process related to degenerate doping in semiconductors.

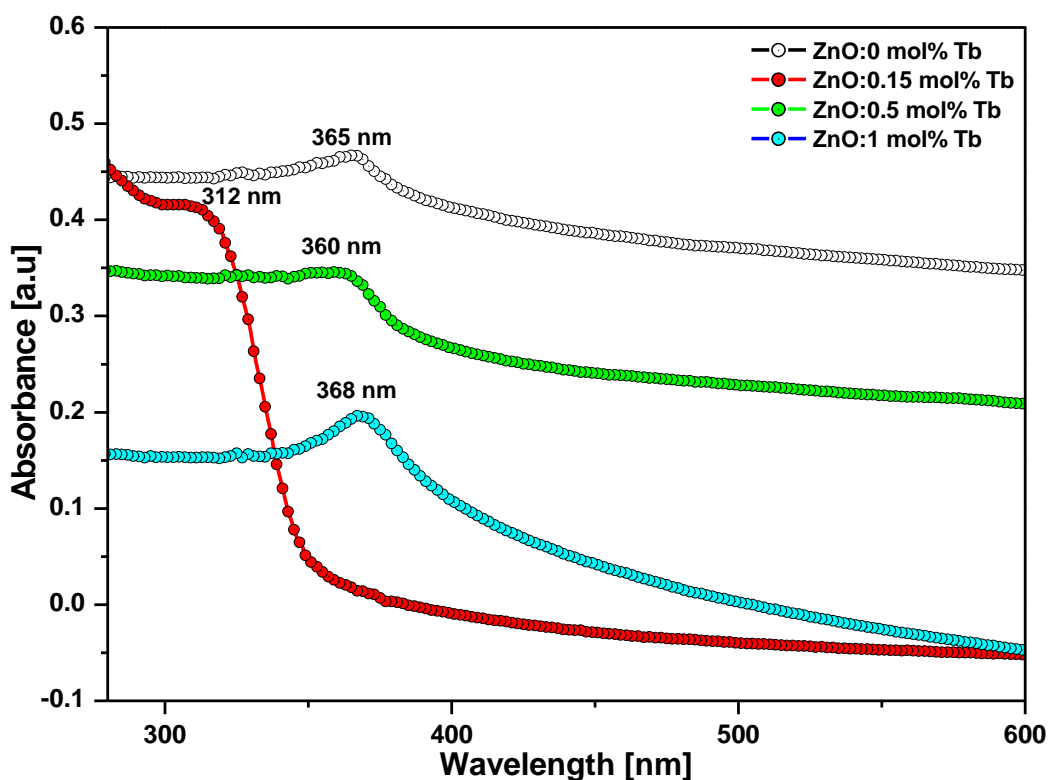


Figure 4.8: UV-Vis Spectra of the as-prepared un-doped and Tb³⁺ doped ZnO nanocrystals dried at 200°C.

From this optical absorption study, the direct band gaps of un-doped and Tb³⁺ doped samples were then calculated. The band gap energies (E_g) were determined from absorption coefficient based on Tauc's method [47-50] using the following relation:

$$\alpha(\lambda)hv = B(hv - E_g)^m$$

where E_g , hv and B are the optical gap, photon energy and constant respectively, $m = 1/2$ in direct band gap semiconductors, $\alpha(\lambda)$ is the absorption coefficient defined by the Beer-Lambert's law as $\alpha(\lambda) = \frac{2.303 \times \text{Abs}(\lambda)}{D}$, where $\text{Abs}(\lambda)$ and D are the absorbance and the diameter of the particle respectively.

The band-gap energies of ZnO nanostructures were extrapolated from the slope of the graphs where $[\alpha h\nu]^2$ plotted versus photon energy, $h\nu$ as shown in **Figure 4.9**. The extrapolated optical band-gap energies were found to be 2.81 eV for un-doped and 3.60, 3.55 and 2.95 eV for 0.15, 0.5, and 1 mol% of Tb^{3+} in ZnO, respectively. It can be seen that the Tb^{3+} doped samples showed a slight increase in the value and this is due to the addition of Tb^{3+} ions into ZnO host lattice. In addition, the minor increase in the band-gap value with increasing dopant concentration agrees well with the blue-shift in the optical absorption results and this indicates the widening of the band-gap with increasing dopant (Tb^{3+}) concentration.

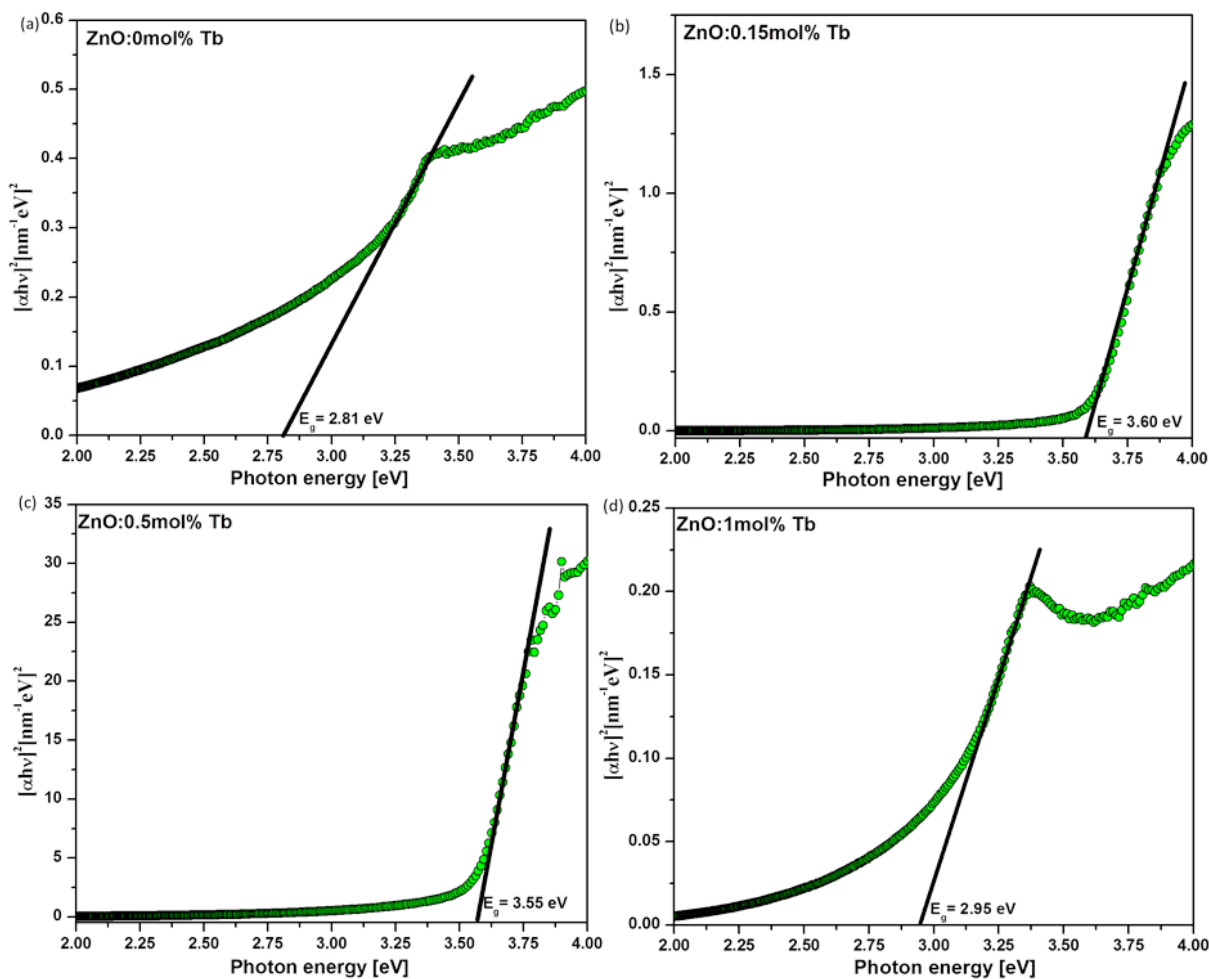


Figure 4.9: The band-gap estimated using TAUC's relation from UV-Vis absorption spectra for un-doped and Tb^{3+} doped ZnO nanocrystals.

Table 4.2: Optical band gap for un-doped and Tb-doped ZnO estimated using different approaches.

X (mol% Tb)	TAUC E_g (eV)	EMA E_g (eV)
0	2.81	3.50
0.15	3.60	3.55
0.5	3.55	3.55
1	2.95	3.45

The optical band-gap (E_g) estimated using the TAUC's method were compared to the values obtained by effective mass approximation (EMA) model, the obtained results are listed in **Table 4.2**. It is observed that at higher Tb^{3+} concentration, the band-gap is found to decrease because the excess of Tb^{3+} ions was segregated into the grain boundaries, and thus do not act as dopant [46].

The room temperature PL emission spectra of the as-prepared un-doped and (0.15, 0.5, and 1 mol%) Tb^{3+} doped ZnO nanocrystals upon excitation at 310 nm using a xenon lamp as an excitation source is shown in **Figure 4.10**. Under 310 nm excitation, un-doped ZnO exhibited two emission peaks, a weak emission peak at 359 nm and a broad green emission at 509 nm. The weak emission at 359 nm can be attributed to the recombination of free electrons with holes in ZnO through exciton-exciton collision process corresponding to near band-edge emission of ZnO [27,51,52]. The broad green emission centred at 509 nm has often been ascribed to single ionized oxygen vacancy [27,39,53,54] resulted from the radiative recombination of a photo-generated hole with an electron occupying the oxygen vacancy (V_o) [51,52]. In contrast with un-doped ZnO, additional weak violet, blue and green emission peaks centred at 392, 437, 477, 499 and 528 nm were observed after incorporation of 0.15 mol% of Tb^{3+} in ZnO. These blue and green emission peaks can be associated with the intra-4f transitions of Tb^{3+} in particular, the $^5D_3 \rightarrow ^7F_{6,4}$ and $^5D_4 \rightarrow ^7F_{6,5}$ transitions, respectively [9,30,55]. In addition, a slight decrease on the broad

green emission compared to un-doped ZnO was noted with 0.15 mol% addition of Tb^{3+} in ZnO. However, when the Tb^{3+} concentration was increased to 0.5 mol%, the PL emission spectrum was dominated by blue and green emission peaks with one additional peak at 406 nm due to $^5\text{D}_3 \rightarrow ^7\text{F}_5$ transition of Tb^{3+} . The broad defect emission from ZnO was quenched. The quenching of broad defect emission of ZnO observed at this concentration is possibly due to the formation of intrinsic trapping centers roused from the substitution of Zn^{2+} by Tb^{3+} in the nanocrystals lattice. Further increase of Tb^{3+} concentration to 1 mol% led to appearance of broad defect-related emission peak from ZnO with weak emission peaks from Tb^{3+} ions overlapped on the broad band of ZnO. These results suggest energy transfer from ZnO to Tb^{3+} . It is important to mention that the exciton peak from ZnO was completely suppressed for all Tb^{3+} doped ZnO samples. In addition, the PL emission spectra exhibited a red-shift in emission specifically from 0.15 and 1 mol% Tb^{3+} doped ZnO compared to un-doped ZnO nanocrystals. A similar red-shift in PL emission spectra was also observed by Al Rifai et al. [56] for emission from Eu^{3+} doped compared to pure ZnO nanowires and it was attributed to Eu^{3+} intra-ionic transitions.

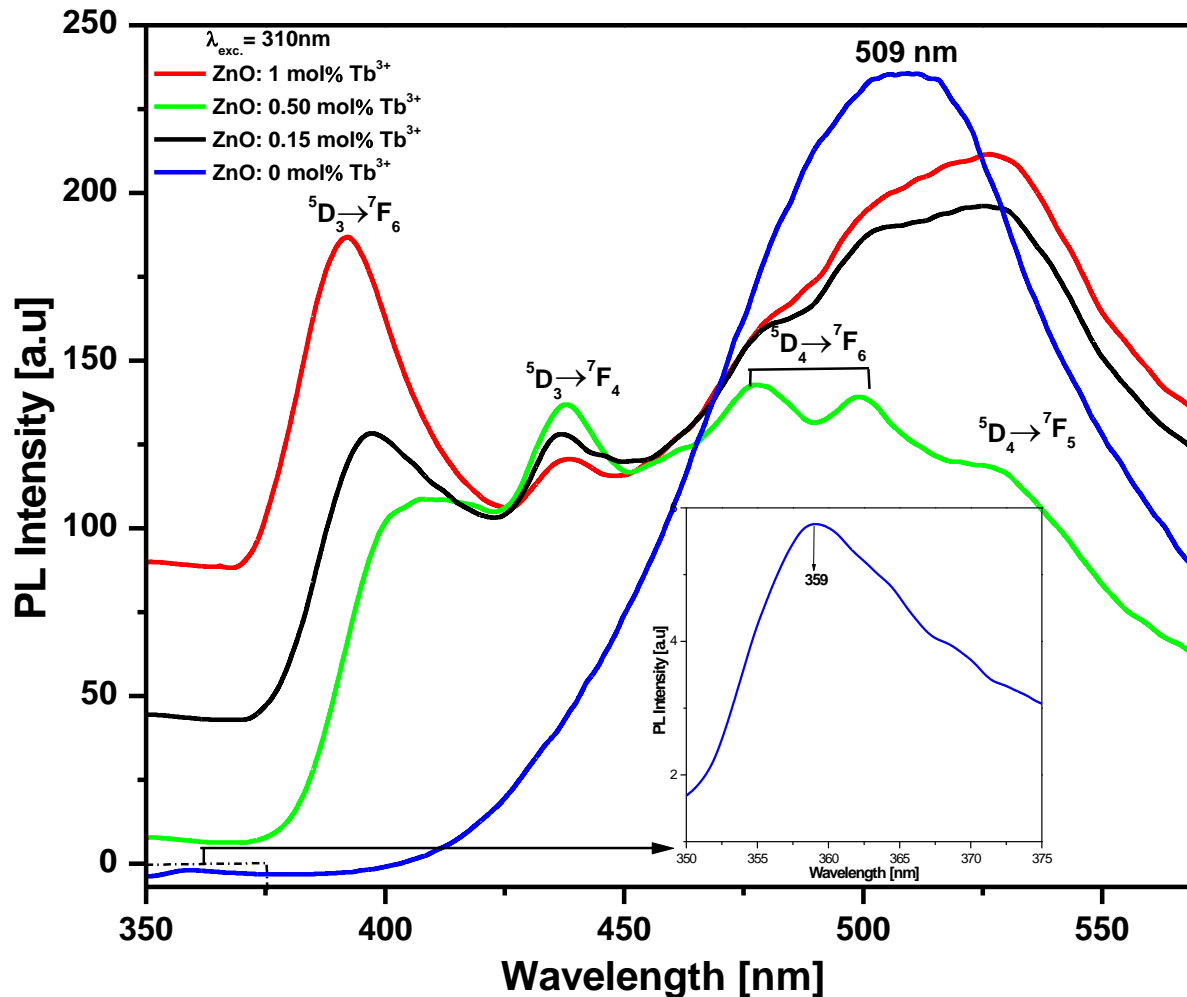


Figure 4.10: PL emission spectra of the as-prepared un-doped and Tb^{3+} doped ZnO after excitation at 310 nm using a Xenon lamp.

Based on previous studies, transfer of energy from the host to rare-earth ions in the case of rare-earth-ion-doped semiconductors often result in strong suppression and/or modification of the host luminescence [31,57]. In fact, such modification can be taken to be an evidence for energy transfer from the host to the rare earth ions. In the current study, the energy transfer process from ZnO host to Tb^{3+} ions may be explained by the energy level diagram presented in **Figure 4.11**. Upon excitation of ZnO: Tb^{3+} nanocrystals by 310 nm, transition of electrons from the valence to conduction band of ZnO nanocrystals occurs. Most of the excited electrons are

captured by traps at energy storage centers of defect complexes resulted from the substitution of Zn^{2+} by Tb^{3+} ions and/or V_O in the nanocrystals and then transfer non-radiatively to the $^5\text{D}_3$, and further to $^5\text{D}_4$, resulting to radiative transitions from $^5\text{D}_3$ and $^5\text{D}_4$ of Tb^{3+} giving rise to violet, blue and green emission due to radiative transitions from $^5\text{D}_3$ and $^5\text{D}_4$ of Tb^{3+} to various $^7\text{F}_J$ ($J=4,5,6$) levels.

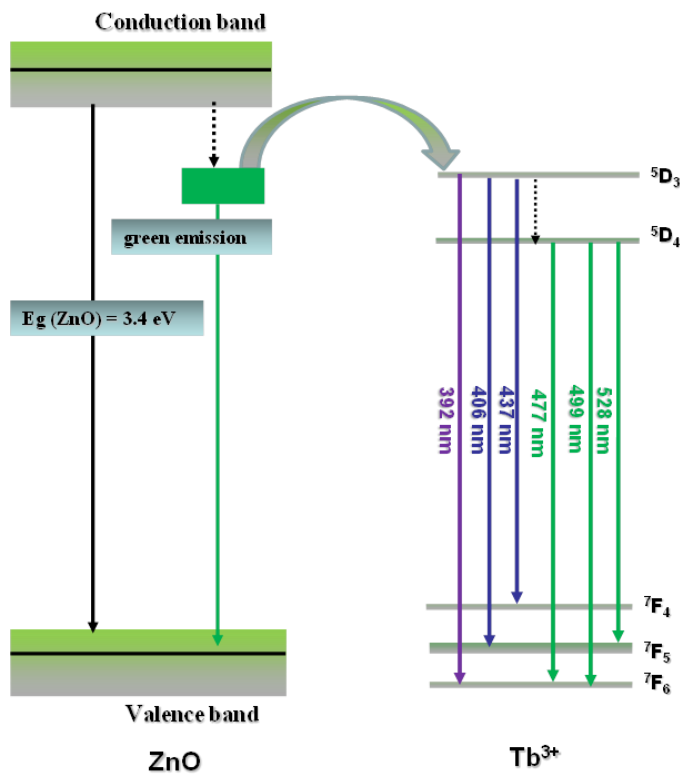


Figure 4.11: Schematic of energy transfer process from ZnO to Tb^{3+} .

4.4 Conclusion

Pure and Tb^{3+} doped ZnO nanocrystals were successfully prepared using sol-gel method and their photoluminescence properties were discussed. The as-prepared un-doped and Tb^{3+} doped ZnO samples were predominantly composed of homogeneously dispersed nanoparticles with particle size ranging from 3 to 6 nm as confirmed from HRTEM analysis. The highly crystalline nanoparticles were obtained without post-annealing treatment. The XRD patterns indicated that Tb^{3+} ions were successfully incorporated into the crystal lattice of ZnO matrix. The XRD and Raman results also confirmed the proper hexagonal phase formation and improved crystallinity with increasing dopant concentration. Optical absorption results indicated a blue-shift of the absorption edges with increasing Tb^{3+} concentration for Tb^{3+} doped samples associated with reduction of particle size as dopant concentration is increased. The PL results for Tb^{3+} doped ZnO samples showed blue and green emission from Tb^{3+} ions associated with $^5\text{D}_3 \rightarrow ^7\text{F}_{5,4}$ and $^5\text{D}_4 \rightarrow ^7\text{F}_{6,5}$ transitions for 0.5 mol% of dopant concentration. At 0.15 and 1.5 mol%, the broad defect emission peak from ZnO was found to dominate the PL emission spectra with the weak blue and green emission from Tb^{3+} ions overlapping the broad band emission from ZnO. Based on the aforementioned results, it was then concluded that, the energy transfer from ZnO host to Tb^{3+} ions is efficient when 0.5 mol% of Tb^{3+} ions are doped into ZnO lattice.

4.5 References

- [1] Morkoç H and Hadis ÜÖ, WILEY-VCH Verlag GmbH & Co. KGaA, Weinheim, (2009)
ISBN: 978-3-527-40813-9
- [2] Coleman VA and Jagadish C, Elsevier Limited, (2006)
- [3] Dhlamini MS, Mhlongo GH, Swart HC and Hillie KT, *J Lumin* **131** (2011) 790
- [4] Shestakov MV, Tikhomirov VK, Kirilenko D, Kuznetsov AS, Chibotaru LF, Baranov AN, Van Tendeloo G and Moshchalkov VV, *Opt Express* **19** (2011) 15955
- [5] Nath SS, Choudhury M, Chakdar D, Gope G and Nath RK, *Sens Act B* **148** (2010) 353
- [6] Ntwaeaborwa OM, Swart HC and Kroon RE, *J Vac Sci Technol A* **25** (2007) 1152
- [7] Ntwaeaborwa OM, Swart HC, Kroon RE, Holloway PH and Botha JR, *Surf Interface Anal* **38** (2006) 458
- [8] Mezdrogina MM, Eremenko MV, Golubenko SM and Razumov SN, *Phys Solid State* **54** (2012) 1235
- [9] Pitale SS, Kumar V, Nagpure IM, Ntwaeaborwa OM, Coetsee E and Swart HC, *J App Phys* **109** (2011) 013105
- [10] Yang J, Gao M, Yang L, Zhang Y, Lang J, Wang D, Wang Y, Liu H and Fan H, *App Surf Sci* **255** (2008) 2646
- [11] Saif M, Hafez H and Nabeel AI, *Chemosphere* **90** (2013) 840
- [12] Pal Partha P and Manam, *J Rare Earths* **31** (2013) 37
- [13] Galli G, *Nat Phys* **436** (2005) 32
- [14] Erwin SC, Zu L, Haftel MI, Efros AL, Kennedy TA and Norris DJ, *Nat Phys* **436** (2005) 91
- [15] Ortiz A, Falcony C, Garcia M and Sanchez A, *J Phys D: Appl Phys* **20** (1987) 670471
- [16] Ji S, Yin L, Liu G, Zhang L and Ye C, *Chem Commun* (2009) 2344
- [17] Lima SAM, Davolos MR, Legnani C, Quirino WG, Cremona M, *J Alloys Comp* **418** (2006) 35
- [18] Liu S-M, Liu F-Q, Zhang Z-H et al. *Acta Phys Sin* **49** (2000) 2307
- [19] Yang L, Tang Y, Hu A, Chen X, Liang K, Zhang L, *Physica B* **403** (2008) 2230
- [20] Chen H-Y, Yang R-Y, Chang S-J, *J Phys Chem Solids* **74** (2013) 344
- [21] Rajeswari YN, Chandra BA, *Prog Nanotechnol Nanomatt* **2** (2013) 1

- [22] Bryan DJ and Gamelin DR, *Prog Inorg Chem* **54** (2005) 47
- [23] Djuricic AB, Leung YH, Tam KH, FHsu Y, Ding L, Ge WK, Zhong YC, Wong KS, Chan WK, Tam HL, Cheah KW, Kwok WM and Phillips DL, *Nanotechnology* **18** (2007) 095702
- [24] Coleman VA, Bradby JE, and Jagadish C, *App Phys Lett* **89** (2006) 082102
- [25] Spanhel L and Anderson MA, *J Am Chem Soc* **113** (1991) 2826
- [26] Meulenkamp EA, *J Phys Chem B* **102** (1998) 5566
- [27] Mhlongo GH, Ntwaeaborwa OM, Swart HC, Kroon RE, Solarz P, Ryba-Romanowski W and Hillie KT, *J Phys Chem C* **115** (2011) 17625
- [28] Li Z, Li P, Wan Q, Zhai F, Liu Z, Zhao K, Wang L, Lü S, Zou L, Qu X, and Volinsky AI, *J Phys Chem C*, (2013) dx.doi.org/10.1021/jp405844z
- [29] Patterson AL, *Phys Rev* **56** (1939) 978
- [30] Sun L, Jiang S and Marciante JR, *Opt Express* **18** (2010) 12191
- [31] Zhang Y, Liu Y, Wu L, Xie E, and Chen J, *J Phys D: Appl Phys* **42** (2009) 085106
- [32] Mohanty P, Kim B, Park J, *Mater Sci Eng B* **138** (2007) 224-227
- [33] Loudon R, *Adv Phys* **13** (1964) 423
- [34] Calleja JM, Cardona M, *Phys Rev B* **16** (1977) 3753
- [35] Damen TC, Porto SPS and Tell B, *Phys Rev* **142** (1966) 570
- [36] Du Y-P, Zhang Y-W, Sun L-D and Yan C-H, *J Phys Chem C* **112** (2008)12234
- [37] Romcevic N, Kostic R, Romcevic M, Hadzic B, Kuryliszyn-Kudelska I, Dobrowolski W, Narkiewicz U and Sibera D, *Act Phys Pol A* **114** (2008) 1323
- [38] Devaraj R, Karthikeyan K, Jeyasubramanian K, *Appl Nanosci* (2012)
DOI 10.1007/s13204-012-0072-1
- [39] Yang RD, Tripathy S, Yuntao L, Sue H-J, *Chem Phys Lett* **411** (2005) 150
- [40] Schumm M, *ZnO-based semiconductors studied by Raman spectroscopy: semimagnetic alloying, doping, and nanostructures*, 2008, [PhD Thesis], Julius–Maximilians–Universität Würzburg, Germany
- [41] Yang L, Tang Y, Hu A, Chen X, Liang K, Zhang L, *Physica B* **403** (2008) 2230
- [42] Li X-H, Xu J-H, Jin M, Shen H, Li XM, *Chinese Phys Lett* **23** (2006) 3356
- [43] Zhou H, Alves H, Hofmann DM, Kriegseis W and Meyer BK, *Appl. Phys. Lett.* **80** (2002) 210

- [44] Bang J, Yang H, Holloway PH, *J Chem Phys* **123** (2005) 084709
- [45] Li G-R, Lu X-H, Su C-Y and Tong Y-X, *J Phys Chem C* **112** (2008) 2927
- [46] Miloslavskii VK, Pogrebniak PS, *Phys Stat Sol (b)* **51** (1972) K99
- [47] Tauc J, Menth A, *Non Cryst Solids* **8** (1972) 569
- [48] Goldenblum A, Belumarian A, Teodorescu V, *J Optoelectron Adv Mater* **8** (2006) 2129
- [49] Ghobadi N, *Intern Nano Letters* **3** (2013) 47
- [50] Potter Jr BG and Simmons JH, *Phy Rev B* **37** (1988) 10838
- [51] Lyu SC, Zhang Y, Ruh H, et al., *Chem. Phys. Lett.* **363** (2002) 134
- [52] Wang D, Xing G, Gao M, Yang L, and Wu T, *Phys. Chem. C* **115** (2011) 22729
- [53] Luo L , Gong L, Liu YF, Chen J, Ding CR, Tang XG, Li XL, Qiu ZR, Wang HZ, Chen XM, Li KF, Fan HH and Cheah KW, *Opt Mat* **32** (2010) 1066
- [54] Jayanthi K, Sunkara Manorama V and Santa Chawla, *J Phys D: Appl Phys* **46** (2013) 325101
- [55] Podhorodecki A, Gaponenko NV, Banski M, Kim T and Misiewicz J, *ECS transactions* **28** (2010) 81
- [56] Rifai SA and Kulnitskiy BA, *J. Phys. Chem. Solids*, (2013) [http: dx.doi.org /10.1016.j.jpics.2013.06.019](http://dx.doi.org/10.1016/j.jpics.2013.06.019).
- [57] Liu Y, Luo W, Li R, and Chen X, *Opt Lett* **32** (2007) 566

Chapter 5. Properties of Ytterbium ions in ZnO Nanocrystals

This chapter discusses the synthesis and characterization of un-doped and Ytterbium doped-ZnO nanocrystals. As prepared ZnO and ZnO:Yb³⁺ was characterized using High Resolution Transmission Electron Microscope (HR-TEM) equipped with an Energy Dispersive X-ray Spectroscopy (EDX), X-ray powder Diffraction (XRD), Field emission Scanning Electron Microscope (FE-SEM) and X-ray Photoelectron Spectroscopy (XPS) to investigate morphological, elemental, phase, structural and chemical state, respectively. Photoluminescence (PL) was studied using a He-Cd laser with an excitation wavelength of 325 nm. The UV-Vis absorption result is also discussed.

5.1 Introduction

Throughout the last decade an unprecedented interest on rare earth ions doped ZnO nanostructures has been observed worldwide [1,2]. The unique optical properties of rare earth ions have motivated researchers to develop luminescent materials based on ZnO nanostructures in order to use effectively its wide direct band-gap (3.37 eV), large exciton binding energy (60 meV) and high optical gain (320 cm^{-1}) at room temperature [3-5]. To the best of our knowledge, among other rare earth ions, Yb^{3+} has not been intensively investigated so far. Only few reports have been found in the literature where optical properties of Yb^{3+} doped ZnO were studied [6-10], and almost none of the previous reports were dedicated to study the enhancement of the exciton emission due to Yb^{3+} addition into ZnO lattice.

In this chapter, we report on the successful incorporation of Yb^{3+} ions into ZnO lattice using sol-gel method to produce Yb^{3+} doped ZnO nano-phosphors. The Yb^{3+} concentration was varied from 0.5 to 0.75 mol% in order to study the PL intensity behavior of ZnO: Yb^{3+} nano-phosphors. The effects of Yb^{3+} on the emission properties of ZnO nanoparticles are also discussed. An in-depth study of the microstructure and photoluminescence properties of un-doped and Yb^{3+} doped nano-phosphors was conducted.

5.2 Experimental detail

ZnO nanocrystals were produced by dissolving zinc acetate in boiling ethanol and the solution was cooled in ice water. The solution of sodium hydroxide dissolved in ethanol was also prepared separately, then cooled in ice water and added drop wise (see subsection 3.1.2) to the ethanol suspension of Zn^{2+} . For preparation of Yb^{3+} doped ZnO samples with different concentrations of Yb^{3+} (0.5 and 0.75 mol%), the ethanol solution of ytterbium nitrate GL KABONGO *et al. Materials Letters* **119** (2014) 71–74 was prepared according to the experimental procedure. The resulting clear solution was kept at room temperature for 24 hours and then washed repeatedly with ethanol and heptane to remove unwanted impurities. The resulting precipitates were then re-dispersed in ethanol or dried at 200 °C for 2 hours. The samples were then characterized by XRD, EDX, XPS, SEM, TEM, UV-Vis and He-Cd laser (325 nm).

5.3 Results and discussion

5.3.1 Structural and surface properties

The Yb^{3+} doped ZnO with different concentrations of Yb^{3+} consist of broadened diffraction peaks resembling those of the un-doped ZnO and they are consistent with the hexagonal wurtzite structure of ZnO (JCPDS Card n° 36-1451) (see **Figure 5.1** (a)). Using Debye-Scherrer's equation, the average crystallite size of the ZnO products was determined to range from ~4 to 7 nm. In addition, no change in the crystal structure was observed due to the introduction of Yb^{3+} ions into the ZnO lattice, however, a very small shift of the (101) peak to the lower diffraction angle was noticed. It is believed that the absence of Yb^{3+} related diffraction peaks may be due to the complete substitution of Yb^{3+} ions into the Zn^{2+} sites or the interstitial sites of ZnO, whereas

the shift of the (1 0 1) peak to the lower diffraction angle is due to the bigger radius of Yb^{3+} (1.01 Å) compared to that of Zn^{2+} (0.74 Å) ions which increases the lattice constants 'a' and 'c' implying a unit cell expansion in Yb^{3+} doped samples [9]. The SEM image obtained from Yb^{3+} doped ZnO (0.5 mol %) depicted in **Figure 1(b)** revealed uniform tiny clamped particles. Similar results were observed in un-doped ZnO sample (results not shown). The insert of **Figure 1(b)** shows the EDS spectrum of the same sample where the presence of Zn, O and Yb were confirmed. Apart from the expected elements, Cu and C from a copper grid which was used to grow Yb^{3+} doped ZnO thin films were also detected. Furthermore, EDX mappings confirmed the presence of the expected species (**figure 5.2**). The TEM image shown in **Figure 1(c)** confirmed the XRD results and revealed that the Yb^{3+} doped ZnO particles are well crystallized and homogeneously dispersed with an average particle size ranging from ~4 to 7 nm in diameter. The selected area electron diffraction (SAED) pattern shows diffraction rings corresponding to (100), (002), (101), (102), (110) and (103) planes revealing the highly polycrystalline nature of these nanoparticles. The calculated interplanar spacings corresponding to each plane are presented in **Table 5.1**. The profile of the 101 plane is shown in **figure 5.3**.

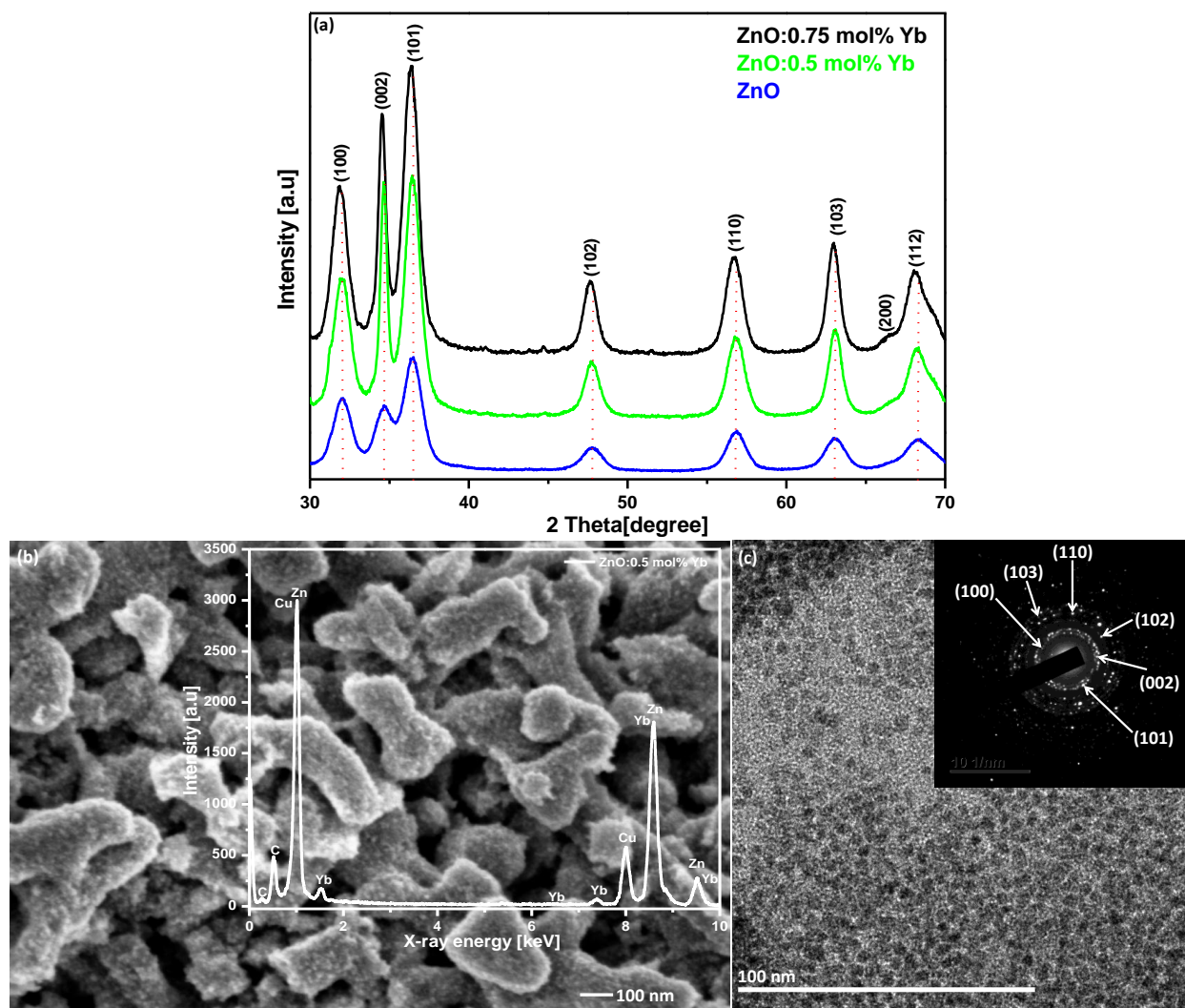


Figure 5.1: (a) XRD patterns of un-doped and Yb doped ZnO nanocrystals, (b) FE-SEM image along with EDX spectrum in the insert and (c) TEM image along with the SAED insert.

Table 5.1 d_{hkl} spacing values calculated for ZnO nanoparticles.

Plane [hkl]	100	002	101	102	110	103
d_{hkl} [nm]	0.281	0.26	0.247	0.191	0.163	0.147

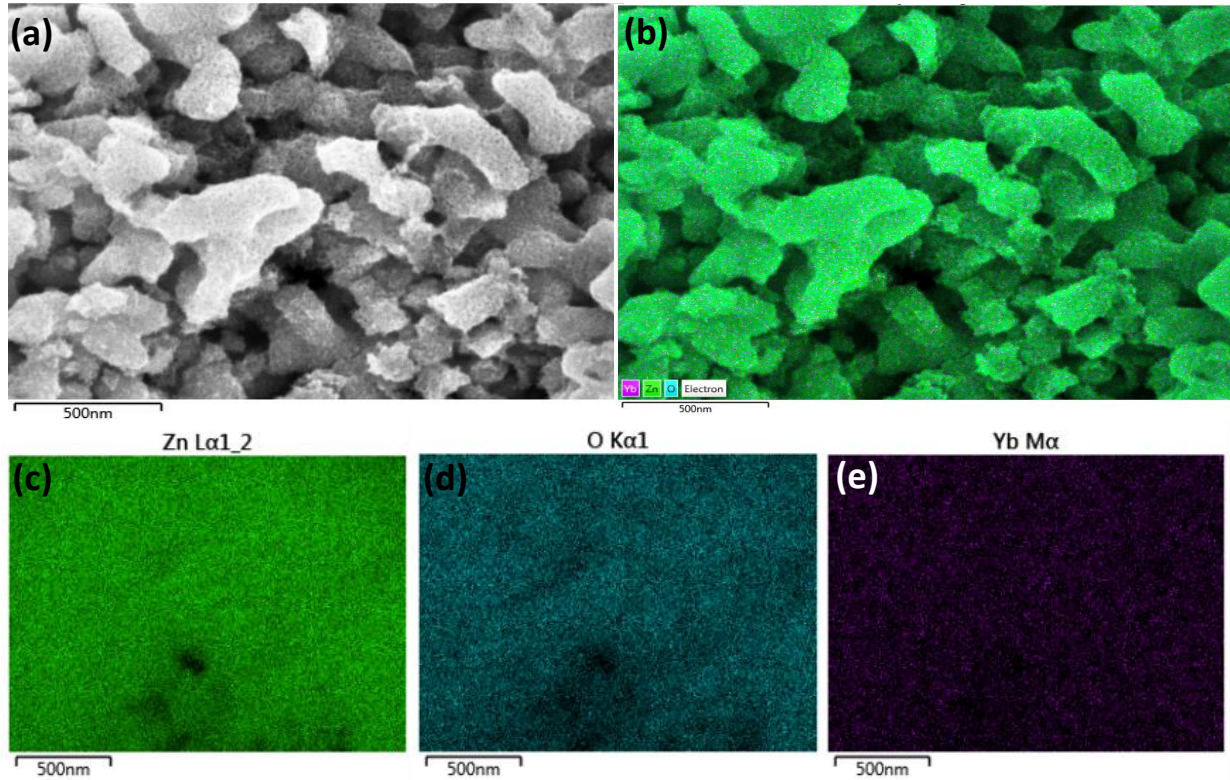


Figure 5.2: (a) FE-SEM image used for conducting EDX analysis, (b) EDX layered image of un-doped ZnO after elemental mappings of Zn, O and Yb, (c-e) Corresponding elemental mappings of Zn, O and Yb.

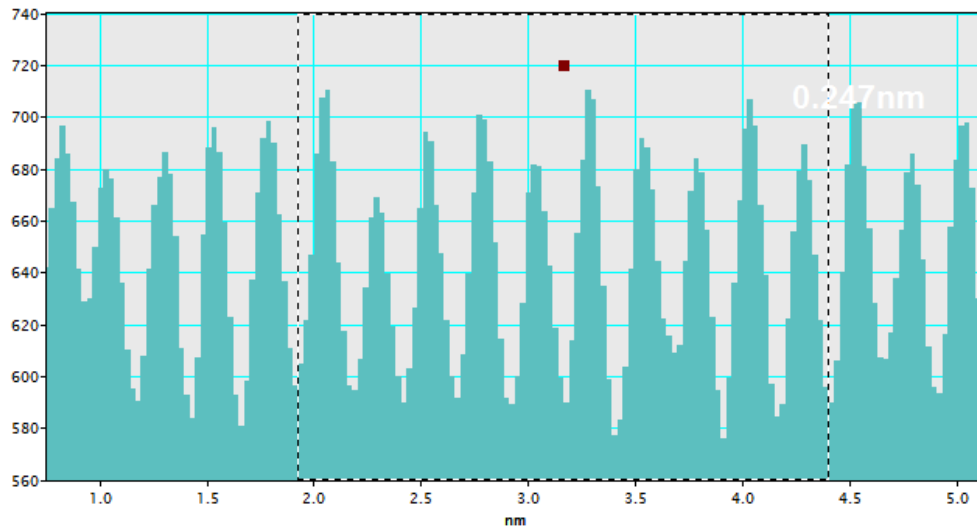


Figure 5.3: HR-TEM profile of the 101 plane for Yb-doped ZnO.

The XPS survey spectra obtained before Ar⁺ sputtering presented in **Figure 5.4** (a) showed the presence of all expected core levels due to Zn 2p, Zn 3p, O 1s, Yb 4d, and C 1s. The binding energy charge correction by adventitious C 1s peak at 284.8 eV was applied. **Figure 5.4** (b) and (c), show the deconvoluted oxygen O 1s peaks of un-doped and Yb³⁺ doped ZnO, respectively. The O 1s peak can be divided into three peaks whose binding energies are 532.3, 531.4 and 530.1 eV (**Table 5.2**) associated with the chemisorbed oxygen species such as CO₃, oxygen vacancies in the oxygen deficient regions of ZnO and intrinsic O²⁻ ions present in a wurtzite structure of hexagonal Zn²⁺ ion arrays, respectively [5]. Addition of Yb ions into ZnO matrix resulted in a fourth oxygen species O²⁻ centred at 529.7 eV resulting in a change in shape of O 1s core level spectrum. Most importantly, the intensity of the oxygen deficient peak at around 531 eV has decreased suggesting the reduction in the concentration of oxygen vacancies after Yb doping [11], which could induce the formation of Yb₂O₃ in the neighboring surface of the nanocrystals. The XPS technique was also used to investigate the oxidation state of Zn and Yb. The Zn 2p peak (**figure 5.5** (a)) contained a doublet whose binding energies were 1045 and 1022 eV, which can be identified as Zn 2p_{1/2} and Zn 2p_{3/2} for un-doped ZnO, respectively, with a spin-orbit splitting of 23 eV. With addition of Yb³⁺ into ZnO lattice, no peak shift was noted in the binding energies, however a second Zn defect was observed after fitting (**figure 5.5** (b)). This compares well with results of Liqiang et al. [12]. Likewise Zn 3p_{3/2} (Zn 3p_{1/2}) at 90.0 eV (91.8 eV) was detected (**figure 5.5** (c)). The Yb 4d peak in **Figure 5.4** (d) revealed two peaks with binding energies of 199.2 and 185.5 eV identified as Yb 4d_{3/2} and Yb 4d_{5/2}, respectively. These findings suggest that the presence of Zn and Yb in pure ZnO is in the form of Zn²⁺ and Yb³⁺ oxidation state.

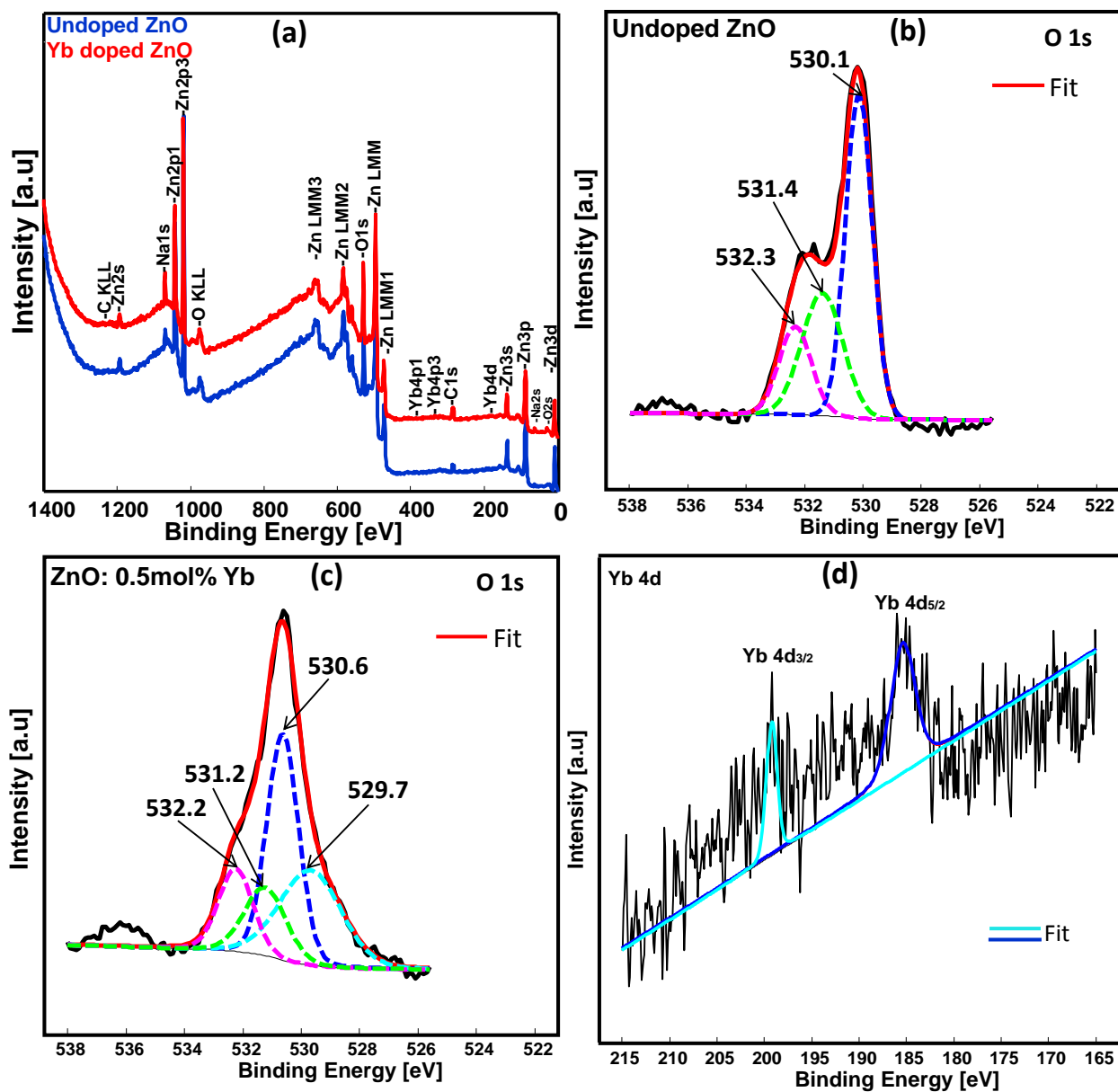


Figure 5.4: (a) XPS spectra of ZnO and ZnO:Yb³⁺, O 1s spectra of (b) un-doped ZnO and (c) ZnO:Yb³⁺, (d) Yb 4d spectrum of ZnO:Yb³⁺.

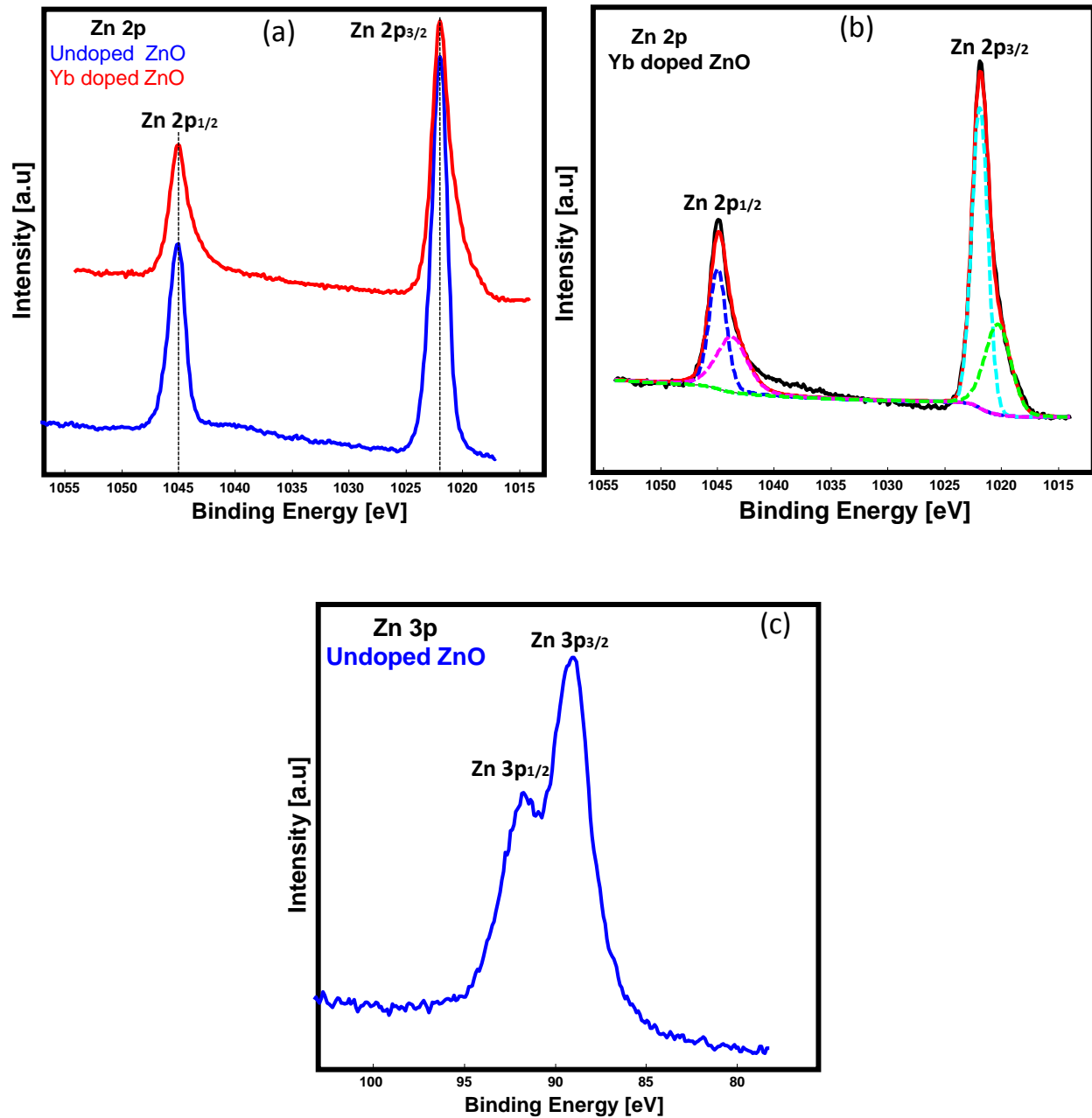


Figure 5.5: Zn 2p core level (a) for undoped ZnO and ZnO:0.5 mol% Yb³⁺, (b) fitted ZnO:0.5 mol% Yb³⁺. (c) Zn 3p core level for undoped ZnO.

Table 5.2: Binding energy positions for core level of O 1s.

Sample	Undoped ZnO			0.5 mol% Yb doped ZnO			
	O ₁	O ₂	O ₃	O	O ₁	O ₂	O ₃
Core level							
Binding energy [eV]	530.14	531.39	532.32	529.7	530.6	531.2	532.2
Area [%]	53.55	29.73	16.71	31.18	38.51	15.20	15.11
FWHM	1.09	1.65	1.30	2.46	1.28	1.67	1.37

5.3.2 Optical properties

The UV–Vis absorption spectra of the as-prepared un-doped and Yb³⁺ doped ZnO samples are presented in **Figure 5.6**. The absorption spectra showed well-defined exciton bands at 365 for un-doped ZnO and 372 for 0.5 mol% Yb³⁺ doped ZnO samples, respectively. It was observed that both absorption peaks for un-doped and Yb³⁺ doped was blue-shifted relative to the bulk exciton absorption (386 nm) [13,14]. The blue-shift observed may be attributed to quantum confinement effect [15]. Moreover, a red-shift of the absorption edge with Yb³⁺ doping was observed, which obviously resulted in a band-gap narrowing contrary to the result obtained in the previous chapter (4.3.3), where the effect of Tb³⁺ doping into ZnO matrix act as a band-gap widening agent.

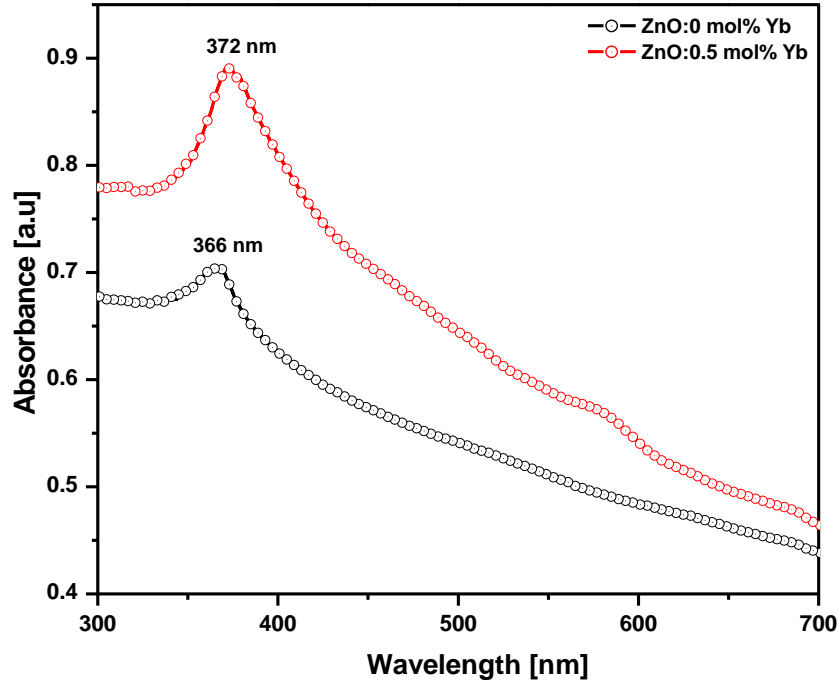


Figure 5.6: UV-Vis Spectra of the as-prepared un-doped and Yb³⁺ doped ZnO nanocrystals dried at 200°C.

The emission spectra of un-doped and doped ZnO nano-phosphors with different Yb³⁺ concentration are shown in **Figure 5.7** (a). The PL emission spectra were obtained under excitation at 325 nm using a He-Cd laser. Two emission peaks, identified as direct band-gap and defect related emission at 377 nm and 509 nm, respectively, were observed from un-doped ZnO sample. The direct band-gap emission peak originate from recombination of free excitonic centers while the broad green peak can be associated with recombination of delocalized electrons at singly occupied oxygen vacancies with deep trapped holes [16]. The broad green emission due to ZnO has shown a decrease and this can be attributed to 0.5 mol% of Yb³⁺ ions into ZnO lattice, while the exciton emission increased significantly. The enhancement of the UV emission may be due to the (i) fact that the ZnO lattice consists of a few singly ionized oxygen vacancies, and/or (ii) creation of more electron-hole pairs with Yb³⁺ doping. Also, effective energy transfer process from Yb³⁺ ions to ZnO may not be excluded as one of the possible reason for enhanced

exciton emission in the presence of Yb^{3+} ions. However, when the doping concentration is further increased to 0.75 mol%, the intensity of the exciton emission dropped, yet still higher than that of un-doped ZnO. The observed slight red-shift on the exciton emission with increasing dopant concentration may be due to the change occurring in the energy band structure as reported elsewhere [17,18]. The insert in **figure 5.7** (a) shows dependence of the $I_{\text{UV}}/I_{\text{GL}}$ ratio on Yb^{3+} concentration and **figure 5.7** (b) presents the evolution of the green luminescence (GL) and UV emission versus Yb^{3+} concentration. The considerably reduced oxygen vacancies with Yb doping were evidenced by the above O 1s core level 531 eV peak in the XPS result. Consequently, decreasing with the surface-to volume ratio [19].

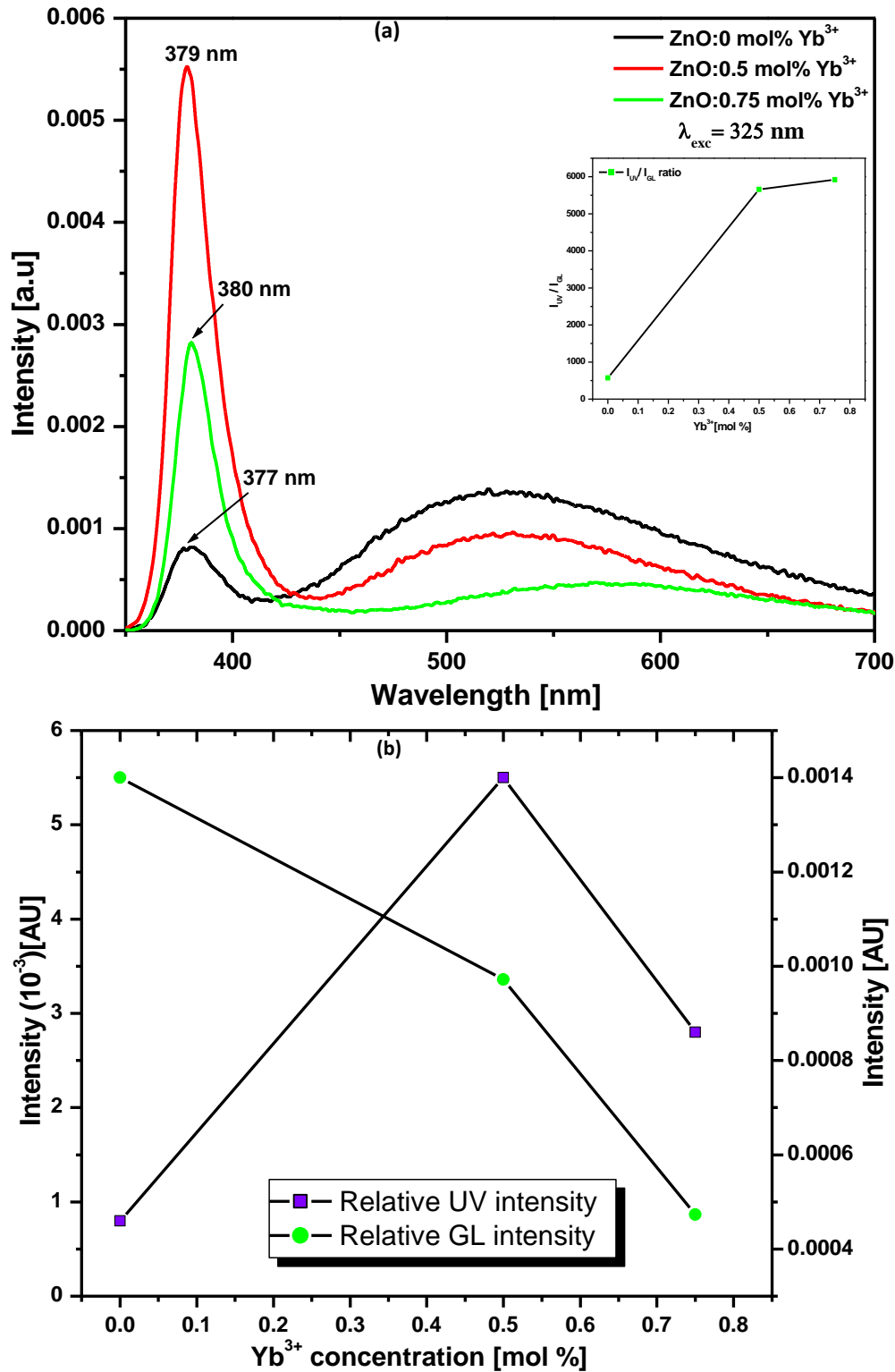


Figure 5.7: (a) PL spectra of un-doped and Yb³⁺ doped ZnO at different concentrations excited at 325 nm. (b) Yb³⁺ concentration dependence of relative UV and GL luminescence intensity.

5.4 Conclusion

Un-doped and Yb³⁺ doped ZnO nanophosphor powders were successfully synthesized using sol-gel method. The PL analysis revealed enhancement of the exciton emission after addition of Yb³⁺ ions into ZnO lattice. Yb³⁺ ions were observed to have substituted Zn²⁺ ions or occupied interstitial sites in ZnO. The Yb³⁺ doped ZnO nanophosphors may have a huge impact on materials development in photonic applications such as lasers.

The observed energy transfer phenomenon and/or the reduction of oxygen related defects could be responsible of the observed enhancement of the exciton emission. Furthermore, the unique optical transition from Yb³⁺ ions ($^2F_{5/2} \rightarrow ^2F_{7/2}$) often observed in the Near Infra-red region of the electromagnetic spectrum was not observed due to the use of a UV detector in the PL system used to collect data.

5.5 References

- [1] Mezdrogina MM, Eremenko MV, Golubenko SM, Razumov SN, *Phys Solid State* **54**(6) (2012) 1235
- [2] Bachir S, Azuma K, Kossanyi J, Valat P, and Ronfard-Haret JC, *J Lumin* **75**(1) (1997) 35
- [3] Ozgur U, Alivou Yi, Liu C, Teke A, Reshchikov MA, Dogan S, Avrutin V, Cho SJ, Markoc H, *J Appl Phys* **98** (2005) 041301(1-103)
- [4] Wang ZL, *J Phys Condens Matt* **16** (2004) 829
- [5] Kumar V, Swart HC, Ntwaeaborwa OM, Kroon RE, Terblans JJ, Shaat SKK, Yousif A, Duvenhage MM, *Mat Lett* **101** (2013) 57
- [6] Song Ye, Nan Jiang, Feng He, Xiao feng Liu, Bin Zhu1, Yu Teng and Jian Rong Qiu, *Opt Express* **18**(2) (2010) 639
- [7] Bai YF, Wang YX, Yang K, Zhang XR, Song YL, and Wang CH, *Opt Commun* **281**(21) (2008) 5448
- [8] Shestakov MV, Tikhomirov VK, Kirilenko D, Kuznetsov AS, Chibotaru LF, Baranov AN, Tendeloo GV, Moshchalkov VV, *Opt Express* **19**(17) (2011) 15955
- [9] Soumahoro I, Schmerber G, Douayar A, Colis S, Abd-Lefdil M, Hassanain N, Berrada A, Muller D, Slaoui A, Rinnert H and Dinia A, *J Appl Phys* **109** (2011) 033708
- [10] Shestakov MV, Baranov AN, Tikhomirov VK, Zubavichus YV, Kuznetsov AS, Veligzhanin AA, Kharin AY, Rosslhuber R, Timoshenko VYV and Moshchalkov VV, *RSC Adv* **2** (2012) 8783
- [11] Wenjuan Cheng, Xueming Ma, *J Phys: Conference Series* **152** (2009) 012039
- [12] Liqiang J, Baiqi W, Baifu X, Shudan L, Keying S, Weimin C, Hongganga F. *J Solid State Chem* **117** (2004) 4221
- [13] Li X-H, Xu J-H, Jin M, Shen H, Li XM, *Chinese Phys Lett* **23** (2006) 3356
- [14] Zhou H, Alves H, Hofmann DM, Kriegseis W and Meyer BK, *Appl Phys Lett* **80** (2002) 210
- [15] Bang J, Yang H, Holloway PH, *J Chem Phys* **123** (2005) 084709
- [16] Mhlongo GH, Dhlamini MS, Swart HC, Ntwaeaborwa OM, Hillie KT, *Opt Mater* **33** (2011) 1495
- [17] Liu Yanmei, Fang Qingqing, Wu Mingzai, Li Yan, Lv Qingrong, Zhou Jun and Wang

- Baoming, *J Phys D: Appl Phys* **40** (2007) 4592
- [18] Baiqi W, Xudong S, Qiang F, Iqbal J, Yan L, Honggang F, Dapeng Y, *Physica E* **41** (2009) 413
- [19] Xiaoyong Xu, Chunxiang Xu, Jun Dai, Jingguo Hu, Fengji Li, Sam Zhang, *J Phys Chem C* **116** (2012) 8813

Chapter 6. Conclusion and future works

6.1 Conclusion

The present thesis report on the sol-gel preparation of ZnO nanocrystals doped with rare earth (RE^{3+}) ions ($RE=Tb^{3+}$, Yb^{3+}), their optical, structural, morphological and elemental chemical composition were studied after a successfully synthesis using different non-destructive techniques such XRD, UV-VIS spectroscopy, Raman spectroscopy, SEM-EDX, TEM, XPS and PL spectroscopy.

High crystalline luminescent hexagonal wurtzite $ZnO:RE^{3+}$ nanocrystals with size ranging from 3-7 nm were obtained. The XRD and Raman study revealed the hexagonal wurtzite structure without second phase, The HR-TEM images confirmed the hexagonal morphology of the nanocrystals with size in the quantum dots range. A slight shift towards lower angles were observed in the XRD patterns of the doped samples due the expansion of the unit cell due to the RE^{3+} ions substitution in the Zn^{2+} ions lattice site. The EDX and XPS elemental analysis were used to investigate the chemical composition of the prepared samples. SEM images, elemental mapping, confirmed the even distribution of RE^{3+} ions in the matrix as well as the Zn and O.

Optical studies using UV-Vis absorption spectroscopy allow us to emphasize on the tunability of the band-gap of the prepared doped ZnO nanocrystals. Furthermore, optical investigation based on Photoluminescence spectroscopy evidenced the presence of energy transfer between the rare earth dopant and the ZnO host matrix which was discussed in detail.

The PL data for ZnO:Yb³⁺ revealed an increase of the exciton emission intensity which was attributed to energy transfer.

6.2 Future works

In this study, ZnO was doped with terbium and ytterbium, the future works will be based on the optical, structural and elemental investigation of other lanthanides such as erbium, holmium, thulium, etc, their lifetime and quantum efficiency could also be studied. Moreover, the influence of the annealing temperature on the properties of the prepared phosphors should be done.

Knowing that the current research interest on luminescent materials is moving to solar cells and biological imaging, the prepared phosphors are promising materials for photovoltaic applications in order to improve devices efficiency.

The study of structural, elemental and optical properties on the annealed samples is a promising research project that still needs to be undertaken. In this regard, the thermogravimetric analysis (TGA) result shown in the appendix (A.0) give an indication on the minimum temperature needed to subject the prepared powder in order to remove all organic constituents.

Appendix

A.0 Thermogravimetric analysis (TGA) result

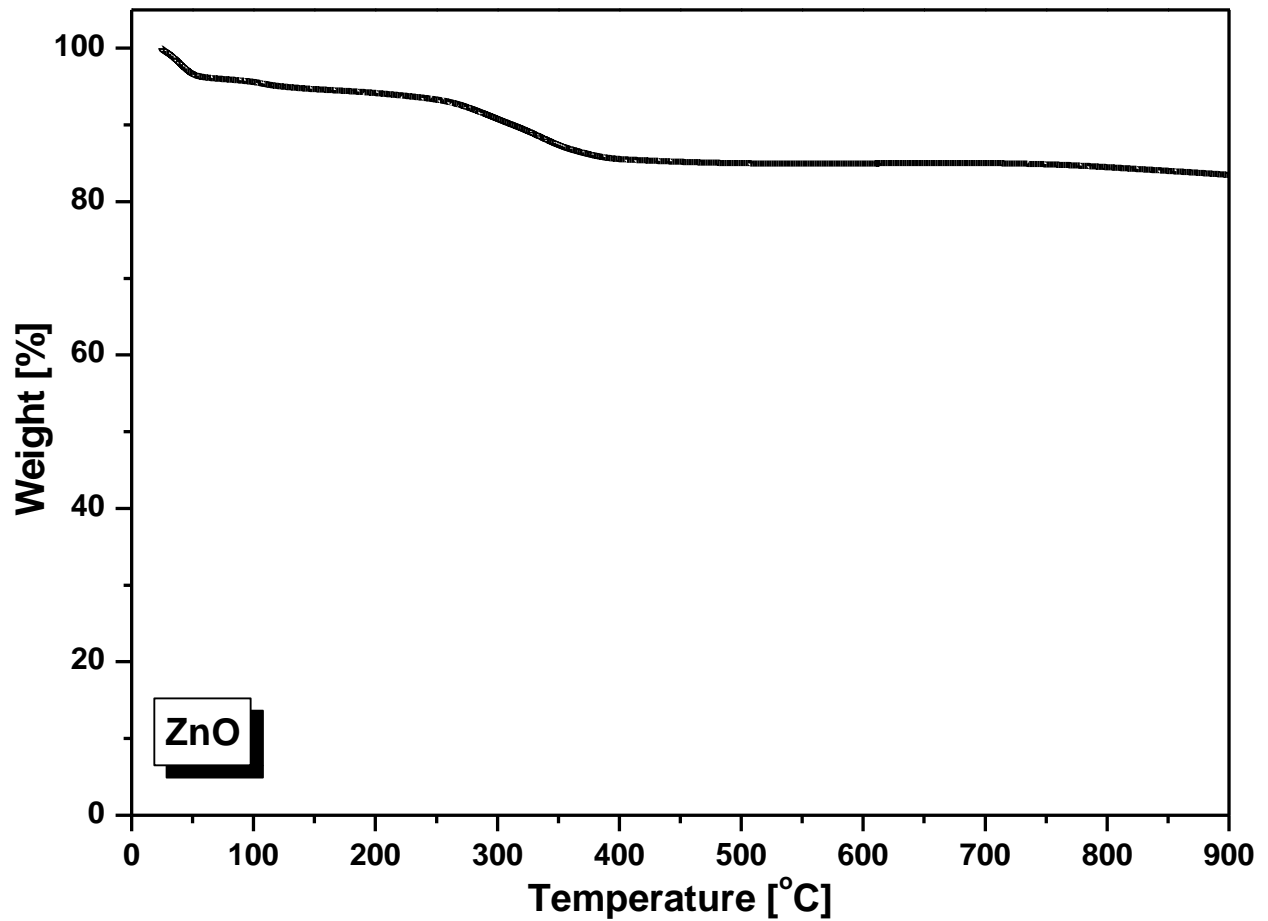


Figure A.1: TGA curve of un-doped ZnO phosphor powder. The sample was heated in ambient atmosphere at a heating rate of 10 °C/min.

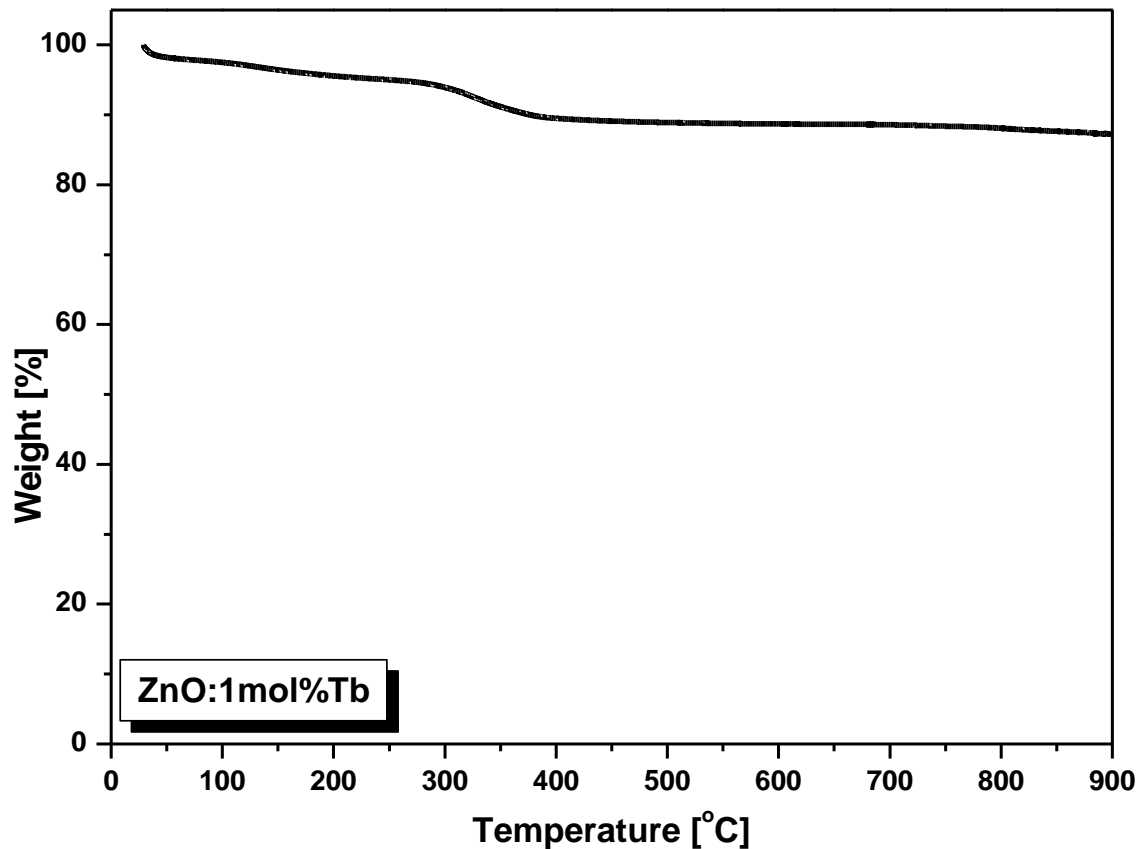


Figure A.2: TGA curve of terbium-doped ZnO phosphor powder. The sample was heated in ambient atmosphere at a heating rate of 10 °C/min.

A.1 Publications

- **G.L. Kabongo**, G.H. Mhlongo, T. Malwela, B.M. Mothudi, K.T. Hillie, M.S. Dhlamini. Microstructural and photoluminescence properties of sol-gel derived Tb³⁺ doped ZnO nanocrystals, *Journal of Alloys and Compounds* **591** (2014) 156-163
- **G.L. Kabongo**, G.H. Mhlongo, B.M. Mothudi, K.T. Hillie, H.C. Swart, M.S. Dhlamini. Enhanced exciton emission from ZnO nano-phosphor induced by Yb³⁺ ions, *Materials Letters* **119** (2014) 71–74

A.2 Conferences

- **G.L. Kabongo**, G.H. Mhlongo, B.M. Mothudi, K.T. Hillie, M.S. Dhlamini. Sol-gel synthesis and characterization of Terbium ions doped zinc oxide nanoparticles, 58th Annual Conference of the South African Institute of Physics (SAIP) conference, 8 to 12 July 2013, University of Zululand (UNIZULU).
- **G.L. Kabongo**, G.H. Mhlongo, B.M. Mothudi, K.T. Hillie, M.S. Dhlamini. Structural and optical properties of Eu –doped and undoped ZnO nanoparticles, BRICS symposium 2013, University of South Africa (UNISA).

A.3 Awards

- 2013 IOP Institute of Physics Entrepreneurship Award for best demonstrating the understanding of entrepreneurial skills and explanation of turning a scientific invention into a commercial success, awarded on 24th May 2013, Ilovo, Kwazulu-Natal, RSA.
- 2014 South African Institute of Physics DPCMM Master Student winner award for the most outstanding work in the field of Condensed Matter Physics and/or Material Science, based on a publication in a scientific journal originating from a Masters dissertation submitted at a South African institution for tertiary education. Vacutec Prize awarded during the De Beers Gold Medal Banquet on 11th July 2014, Helderfontein Estate, Johannesburg, RSA. [publication based on Chapter 5]

Résumé

Les nanocristaux d'Oxide de Zinc (ZnO) pure ainsi que dopés sous différentes concentrations d'ions terbium (Tb^{3+}) et ytterbium (Yb^{3+}) ont été synthétisés avec succès via un procédé sol-gel afin de produire des nanophosphors d'oxide de Zinc activés terres rares. Les poudres finales furent obtenues après séchage des gels précurseurs à 200°C sous air ambiant.

Sur la base des résultats de la diffraction par rayons X (XRD), on a constaté que les nanophosphors de ZnO pure et dopées RE^{3+} étaient hautement polycristallins, indépendamment de la terre rare. En outre, les diagrammes de diffraction sont tous indexés à la structure hexagonale wurtzite de ZnO et appartiennent au groupe de symétrie $P6_3mc$. La spectroscopie Raman a confirmé la structure wurtzite des échantillons préparés.

La cartographie élémentaire effectuée sur les échantillons préparés à l'aide d'un microscope électronique à balayage (MEB) équipé d'un spectromètre à dispersion d'énergie à rayons X (EDX) a révélé une répartition homogène des différents composés à savoir Zn, O, et les ions RE^{3+} . L'analyse au microscope électronique à transmission à haute résolution (HR-TEM) a indiqué que les échantillons non dopés et dopés RE^{3+} étaient composés de particules hexagonales dispersées de façon homogène et de haute cristallinité de dimension moyenne variant de 4 à 7 nm de diamètre, qui était confirmé par l'analyse par diffraction à rayons X (XRD).

L'étude photoluminescente (PL) des nanoparticules dopées sous différentes concentrations de Tb^{3+} a révélé qu' à hauteur de 0.5 mol% Tb^{3+} , des émissions bien définies des transitions intra ioniques $4f-4f$ de Tb^{3+} ont été identifiées pendant que l'émission imposante des défauts de ZnO dominait les spectres d'émission des échantillons dopés à hauteur de 0.15 et 1 mol% Tb^{3+} . Le gap optique de chaque échantillon a été extrapolé par application de la méthode

de TAUC aux spectres d'absorption obtenus par spectroscopie visible/ultraviolet (UV/Vis), d'où fut observé un élargissement du gap optique dans les échantillons dopés par comparaison à l'échantillon référence de ZnO pure. En outre, Il fut observé à travers une étude de photoluminescence de ZnO:Yb³⁺ au laser (325 nm), que l'intensité de l'émission de l'exciton fut considérablement amplifiée après insertion d'ions Yb³⁺ dans la matrice de ZnO. L'étude UV-Vis a révélé l'élargissement du gap optique dans le cas des systèmes ZnO:Tb³⁺ ainsi qu'un rétrécissement dans le cas de ZnO:Yb³⁺.

La spectroscopie photoélectronique par rayon X a démontré la présence des terres rares dans tous les échantillons ayant fait l'objet de dopage, ces résultats concluant furent en accord avec les résultats de PL à travers lesquels le transfert d'énergies fut établi. Ce transfert d'énergie, établi entre le ZnO et les terres rares, a été discuté en détail.